ENERGY ABSORPTION OF COMPOSITE STRUCTURES UNDER AXIAL LOADING: DESIGN, MANUFACTURING AND ANALYSIS

by

Mehmet Can Engül

B.S., Mechanical Engineering, Izmir Institute of Technology, 2012

M.S, Mechanical Engineering, Boğaziçi University, 2016

Submitted to the Institute for Graduate Studies in
Science and Engineering in partial fulfilment of
the requirements for the degree of
Doctor of Philosophy

Graduate Program in Mechanical Engineering
Boğaziçi University

2023

ACKNOWLEDGEMENTS

First and foremost, I would like to present my sincere gratitude to my supervisor Prof. Nuri Ersoy for his endless support, encouragement, and leadership. Under his guidance, I have grown intellectually, professionally, and personally in such a manner that I could have never imagined. I am deeply honoured to be his student in Boğaziçi University.

I would like to acknowledge my committee members for their comments and constructive critics throughout my thesis process. I also thank the Boğaziçi University Research Fund for the financial support under the project code of 17621D.

I would like to thank my friends and colleagues Serdar Demir, Uğur Cucu and Kaveh Shahidi for their assistance and support throughout the study. I also thank the members of the Construction Materials Laboratory at İstanbul Technical University, especially Sidar Bıçakcı for their help with the experimental work in the final phase of my study.

I would also like to express my appreciation to my chosen family in İstanbul: Büşra, Damla, Elif, İlker, Maral, Meltem and Ronay for their all along mental and physical assistance with a never-ending faith in me. This thesis could not be written without their support.

I cannot find enough words to express how grateful I am to my dear family. I would like to thank my mother Hülya Engül, my siblings Pınar Engül, Dilşah Sözeri, Bulut Sözeri, my nephew Rüzgar Sözeri, my aunt Deniz İyigünler, but most of all to my father Ercan Engül. I wish he could have seen this important moment. I dedicate this dissertation to him.

ABSTRACT

ENERGY ABSORPTION OF COMPOSITE STRUCTURES UNDER AXIAL LOADING: DESIGN, MANUFACTURING AND ANALYSIS

Geometry has a significant influence on Specific Energy Absorption (SEA) of composite structures. However, the variation of crush induced failure mechanisms with the change in geometry and the way they affect energy absorption capability has not yet been fully clarified. Moving from simple to complex structures, this dissertation aims to conduct a systematic study investigating the influence of geometry on SEA and to design a novel crash box geometry which has a better performance than those currently in use. For that purpose, an experimental investigation is conducted first for the crushing process of the flat, semi-circle, and sinusoidal structures with different dimensions made of both unidirectional and woven fabric prepregs. The results are compared, and variation of the observed failure mechanisms are discussed. The sinusoidal geometry having the highest SEA is identified to utilize in the design of a novel crash box geometry. Design process based on trial and error through manufacturing and testing, on the other hand, is time consuming and expensive so that researchers are currently interested in Finite Element (FE) Model predictions. However, due to the complexity of the process, FE models applied to estimate the SEA of composites require high computational time. This dissertation proposes a novel numerical approach applied for the crushing process of composite structures in which computational cost is decreased by reducing the number of interfaces between plies and modifying the relevant properties. The novel approach is first applied to composite flat plates and later validated by modelling sinusoidal geometries. The same approach, which can estimate the SEA of the structures in more than 50% less time than conventional methods, is then utilized in the design process of a crash box geometry. As a result of various modelling attempts, a novel geometry, which is called “Sun-like Structure” is manufactured and tested. Results show that the SEA of the final geometry is 2.3 times and 16% higher than the flat plates and the single sinusoidal structures, respectively. In the final part of the thesis work, tapering is applied to edges of the crash box structure so that the initial peak load is decreased to prevent an excessive deceleration causing a fatal damage to the passengers during a crush event.

ÖZET

KOMPOZİT YAPILARIN EKSENEL YÜK ALTINDA ENERJİ EMİLİMİ: DİZAYN, ÜRETİM VE ANALİZ

Geometri, kompozit yapıların özgül enerji emilimini (ÖEE) etkileyen önemli faktörler arasındadır; ancak, ezilme kaynaklı hasar mekanizmalarının geometri farklılaştığında nasıl değiştiği ve enerji emilim kapasitesini nasıl etkilediği literatürde tam olarak açıklığa kavuşturulmamıştır. Bu tez çalışmasında basitten karmaşık yapılara doğru ilerleyerek geometrinin ÖEE üzerindeki etkisini ortaya koyan sistematik bir çalışma kurgulanması ve yeni bir geometri tasarlanması hedeflemektedir. Bu nedenle düz ve örgü kumaş kullanılarak üretilen düz, yarım daire ve sinüs yapıların hasarlanma süreçlerini inceleyen deneysel bir çalışma yürütülmüştür. Sonuçlar karşılaştırılmış ve hasar mekanizmalarının farklı geometrilerdeki değişimi tartışılmıştır. Ayrıca, çarpışma kutusu tasarım sürecinde kullanılmak üzere en yüksek ÖEE'ye sahip sinüs yapı geometrisi saptanmıştır. Üretim ve test süreçleri üzerinden ilerleyen tasarım süreçlerinin oldukça pahalı ve zaman alan süreçler olması, araştırmacıları son zamanlarda Sonlu Eleman (SE) modelleri ile daha yakından ilgilenmeye yöneltmiştir. Öte yandan, yapıların enerji emilim kapasitesini tahmin eden modeller, kompleks hasar modlarından ötürü yüksek hesaplama sürelerine ihtiyaç duymaktadır. Bu tez çalışması kompozit yapıların eksenel yük altında ezilme simülasyonları için hesaplama süresini düşüren yenilikçi bir modelleme yaklaşımı önermektedir. Bu yeni yaklaşım, tabaka ve arayüz sayısının düşürülmesi ve ilgili malzeme değerlerinin modifiye edilmesini içermektedir. Yaklaşım önce düz plakalarda denenmiş, daha sonra sinüs yapılara da uygulanmıştır. Yapıların ÖEE değerini geleneksel modelleme tekniklerine göre yaklaşık %50 daha kısa sürede tahmin edebilen bu yöntem, çarpışma kutusunun tasarım sürecinde de kullanılmıştır. Tasarlanan "Güneş" geometrisi üretilip test edilmiştir. Sonuçlar, bu geometrinin düz tabakadan 2.3 kat, sinüs yapıdan ise %16 daha fazla ÖEE'ye sahip olduğunu göstermiştir. Çalışmanın son aşamasında, yolcularda aşırı ivmelenmeden kaynaklı ölümcül hasar oluşumunu engellemek için çarpma esnasında oluşan ilk yüksek yük değeri, oluşturulan çarpışma kutusunun kenarlarına açı verme işlemi yapılarak giderilmiştir.

TABLE OF CONTENTS

ACKNOWLEDGEMENTS iii
ABSTRACT iv
ÖZET v
LIST OF FIGURES viii
LIST OF TABLES xvii
LIST OF SYMBOLS xix
LIST OF ACRONYMS/ABBREVIATIONS xxi
1. INTRODUCTION 1
2. LITERATURE REVIEW 6
2.1. Experimental Studies 6
2.2. Numerical Studies 16
2.3. Summary, Problem Statement and Objectives 24
2.4. Organization of the Thesis 26
3. EXPERIMENTAL AND NUMERICAL INVESTIGATION OF COMPOSITE FLAT COUPONS 29
3.1. Experimental 30
3.2. Numerical 34
3.2.1. Conventional Model 34
3.2.2. Novel Numerical Approach to Decrease Computational Cost 40
3.3. Results and Discussion 44
3.3.1. Test Results 44
3.3.2. Results of Numerical Analyses 49
4. FROM FLAT PLATES TO COMPLEX STRUCTURES: THE INFLUENCE OF GEOMETRY ON SEA 56
4.1. Experimental 57
4.1.1. Manufacturing and Testing of AS4/8552 Semi-Circle and Sinusoidal Structures 57
4.1.2. Manufacturing and Testing of Flat and Sinusoidal Structures Made of Woven Prepregs 60
4.2. Numerical 63

4.2.1. Conventional FE Model with Artificial Plug Initiator 63
4.2.2. Novel Modelling Approach Applied to Sinusoidal Structure 66
4.3. Results and Discussion..... 67
4.3.1. Test Results of Semi-circle and Sinusoidal Structures Made of UD Prepregs..... 67
4.3.2. Test Results of Sinusoidal Structures Made of WF Prepregs 70
4.3.3. Conventional Numerical Results..... 74
4.3.4. The Results of Novel Numerical Approach 80
5. DESIGN, ANALYSIS AND MANUFACTURING OF A CRASH BOX..... 82
5.1. The Influence of Nesting..... 83
5.2. The Influence of Adding T-Joints 85
5.3. Design of a Complex Composite Crash Box Structure..... 88
5.3.1. Numerical Analysis..... 91
5.3.2. Numerical Results 94
5.4. Manufacturing and Testing of Sun-like Geometry 100
5.5. A Solution to Decrease the Peak Load: TAPERING..... 103
6. CONCLUSION 106
REFERENCES 111
APPENDIX A: COPYRIGHT PERMISSIONS FOR FIGURES 129

LIST OF FIGURES

Figure 1.1. Specific energy absorption capacities for various materials. 2

Figure 1.2. Failure of crash box structures made of different materials: steel (left), composite (right). 3

Figure 1.3. Failure modes. a) Compressive matrix failure. b) Tensile matrix failure. c) Compressive fiber failure. d) Tensile fiber failure e) Shear failure. 4

Figure 1.4. Delamination propagation in a CFRP specimen. 4

Figure 2.1. A schematic illustration of crushing of a tube with chamfered edge. 7

Figure 2.2. Typical force-displacement curve for a specimen subject to crushing. ... 7

Figure 2.3. Main failure modes according to the Farley and Jones: (a) transverse shearing and (b) lamina bending failure modes of progressive crushing failure. 9

Figure 2.4. Schematics of the two failure modes identified by Hull: splaying mode (left) and fragmentation mode (right). 9

Figure 2.5. Four progressive crush failure modes as identified by Bisagni. 10

Figure 2.6. Failure modes identified by Chen et al. 11

Figure 2.7. Flat coupon plate fixture proposed by Feraboli et al. 13

Figure 2.8. Experimental setup with full lateral fixture (left), crushed specimen (right) from the study of Lausch et al. 14

Figure 2.9. Simple support fixture presented by Bru et al. 15

Figure 2.10. General schematic of damage propagation. 17

Figure 2.11. Mixed-mode delamination. 21

Figure 3.1. Schematics of stacking sequences of composite plates: $[0/90]_{2s}$ and [0/45/0/-45]s. 30

Figure 3.2. Autoclave in Composites Laboratory at Boğaziçi University 31

Figure 3.3. Manufacturer recommended cure cycle for AS4/8852 [90]. 32

Figure 3.4. The illustration of the specimen and the supporting fixture (left), test setup (right). 33

Figure 3.5. Abaqus/CAE model of the composite flat plates with rigid side walls 34

Figure 3.6. Various Forms of Traction-Separation Curves. 36

Figure 3.7. Mesh and boundary conditions for 2D DCB model. 38

Figure 3.8. Deformed state of the 2D DCB model. 39

Figure 3.9. The load-displacement responses of DCB tests. 39

Figure 3.10. Modelling idea for novel numerical approach. 41

Figure 3.11. Repartition of energy (%) in the crushing process of flat plates..... 41

Figure 3.12. 3-point bending test model and simulated load-displacement results..... 43

Figure 3.13. Load-displacement curve of the $[0/90]_{2s}$ flat specimen with 8 plies..... 44

Figure 3.14. The crushing process of $[0/90]_{2s}$ flat plate specimen with 8 plies 45

Figure 3.15. Load-displacement curve of $[0/90]_{3s}$ flat specimen with 12 plies..... 46

Figure 3.16. The crushing morphology of $[0/90]_{3s}$ flat specimen with 12 plies..... 46

Figure 3.17. Load-displacement curve of $[0/90]_{4s}$ flat specimen with 16 plies..... 47

Figure 3.18. The crushing morphology of $[0/90]_{4s}$ flat specimen with 16 plies..... 47

Figure 3.19. Experimental results of $[0/45/0/-45]_s$ flat specimens: load-displacement curve (left), crushed morphology (right)..... 48

Figure 3.20. Comparison between the load–displacement curves of the experimental test and FE analysis for $[0/90]_{2s}$ flat plate specimen..... 49

Figure 3.21. Comparison between absorbed energy values of $[0/90]_{2s}$ flat plate during the experimental test and FE analysis..... 50

Figure 3.22. Comparison of experimental and numerical analysis of progressive damage of $[0/90]_{2s}$ plates: Test photos (top), Front view of propagation of crush (middle), isometric view of numerical model and delamination growth (bottom)..... 51

Figure 3.23. In-plane failures in $[0/90]_{2s}$ flat plate after 2 mm crash: Fiber failure (left), matrix failure (right). 52

Figure 3.24. Load-displacement curves of the novel approach and comparison with the test data for $[0/90]_{2s}$ specimen. 52

Figure 3.25. Energy results of the novel approach and comparison with the test data for $[0/90]_{2s}$ specimen. 52

Figure 3.26. Comparison of 12-ply $[0/90]_{3s}$ plate model results with experimental tests in terms of load-displacement (left) and absorbed energy curves (right). 53

Figure 3.27. Comparison of 16-ply $[0/90]_{4s}$ plate model results with experimental tests in terms of load-displacement (left) and absorbed energy curves (right). 53

Figure 3.28. Comparison of $[0/45/0/-45]_s$ plate model results with experimental tests in terms of load-displacement (top) and absorbed energy curves (bottom). 55

Figure 4.1. The schematic of the cross section of semi-circle specimen. 58

Figure 4.2. The schematic of the cross sections of sinusoidal structures with 3 curvatures (left), and 5 curvatures (right). 58

Figure 4.3. A snapshot taken during the manufacturing process. 59

Figure 4.4. Manufactured structures: semi-circle (a) and sinusoidal specimens with 3 (b), 5 curvatures (c). 59

Figure 4.5. Test setup. 60

Figure 4.6. MRCC for KOM10T/PL200 woven prepregs. 61

Figure 4.7. The flat specimen and a close-up photo of the woven material. 62

Figure 4.8. Manufactured sinusoidal specimens with 3 (left) and 5 curvatures (right). 62

Figure 4.9. Abaqus/CAE half model of the sinusoidal structure with 3 curvatures: isometric view (left), front view (right). 63

Figure 4.10. The finalized version of artificial plug-initiator design with the position in assembly. 64

Figure 4.11. Abaqus/CAE half model (right) and the schematic of the mid-plane of sinusoidal structures with 7 curvatures (left) (all dimensions are given in millimeters.). 65

Figure 4.12. Abaqus/CAE novel FE model of $[0/90]_{2s}$ sinusoidal structures with 3 curvatures. 66

Figure 4.13. The load-displacement curves of the semi-circle specimens made of UD prepregs. 67

Figure 4.14. The crushed shape of the semi-circle specimen made of UD prepregs at the end of the test. 68

Figure 4.15. The deformed shapes of sinusoidal specimens made of UD prepregs with 3 curvatures (left), and 5 curvatures (right). 69

Figure 4.16. The Load-displacement curves of sinusoidal specimens made of UD prepregs with 3 (left), and 5 curvatures (right). 69

Figure 4.17. Experimental results of flat specimens made of WF prepregs: load-displacement curve (left), crushed morphology (right). 70

Figure 4.18. The load-displacement curves of specimens made of WF prepregs having 3 curvatures. 71

Figure 4.19. The load-displacement curves of specimens made of WF prepregs having 5 curvatures. 72

Figure 4.20. The deformed shapes of sinusoidal specimens made of WF prepregs..... 73

Figure 4.21. Comparison of FE model of sinusoidal specimen having 3 curvatures with experimental tests: load-displacement curves and energy curves. 74

Figure 4.22. Simulated crushed shapes of sinusoidal specimen having 3 curvatures: isometric view with demonstrated matrix failure (left), and cross-sectional view from the mid-plane (right). 75

Figure 4.23. Evaluation of the artificial plug-initiator geometry and corresponding simulation results compared with the observed failure modes. 76

Figure 4.24. Simulated deformed shape with artificial plug-initiator. 77

Figure 4.25. Matrix crack and delamination growth in FE Model with artificial plug-initiator. 77

Figure 4.26. Comparison of FE model (with plug-initiator) with experimental tests: load-displacement curves (left), and energy curves (right) of sinusoidal having 3 curvatures. 78

Figure 4.27. Comparison of FE model with experimental tests: load-displacement curves (left), and energy curves (right) of sinusoidal structure having 5 curvatures. 78

Figure 4.28. Simulated deformed shape of sinusoidal specimen with 7 curvatures. 79

Figure 4.29. Simulation results of sinusoidal structure with 7 curvatures: load displacement and energy curve. 79

Figure 4.30. The overall comparison of SEA of structures 80

Figure 4.31. Comparison of the novel FE model of sinusoidal structure having 3 curvatures with experimental tests in terms of load-displacement (top) and absorbed energy curves (bottom). 81

Figure 5.1. Two sinusoidal composite specimens with vertical line cuts. 83

Figure 5.2. The nested composite structure. 84

Figure 5.3. Experimental results of the nested structure: load-displacement curve (left), crushed morphology (right). 84

Figure 5.4. Cross-sectional view of corrugated structure. 86

Figure 5.5. The lay-up method utilized in the manufacturing process of AS4/8552 corrugated structure. 86

Figure 5.6. Test specimen. 87

Figure 5.7. Experimental results of the corrugated structure: load-displacement curve (left), crushed morphology (right). 87

Figure 5.8. The design idea of the novel crash box geometry. 89

Figure 5.9. Abaqus/CAE model of PSP geometry: (a) front view with symmetry axes, (b) isometric view, (c) one edge with plug initiator. 92

Figure 5.10. The schematic representing four layers and V-shaped trigger. 92

Figure 5.11. Abaqus/CAE models of SL4 (top) and SL8 (bottom) geometries. 93

Figure 5.12. Simulation results of PSP geometry. 94

Figure 5.13. Load-displacement curve of PSP geometry. 95

Figure 5.14. Load-displacement curve of SL4 geometry. 96

Figure 5.15. Simulation results of SL4 geometry. 95

Figure 5.16. Simulation results of SL8 geometry. 97

Figure 5.17. Load-displacement curve of SL8 geometry. 98

Figure 5.18. SEA vs Crush Distance plots for five different geometries. 99

Figure 5.19. General SEA comparison. 99

Figure 5.20. Snapshots taken during the manufacturing process. 100

Figure 5.21. Manufactured sun-like geometry (left) and the test setup (right)..... 101

Figure 5.22. The deformed shape of sun-like geometry at the end of the test. 102

Figure 5.23. The load-displacement curves of SL4 geometry..... 102

Figure 5.24. Comparison of the novel FE model of SL4 structure with experimental tests in terms of load-displacement (left) and energy curves (right)..... 103

Figure 5.25. The tapered geometry..... 104

Figure 5.26. Experimental results of the tapered SL4 structure: load-displacement curve (top) and crushing morphology (bottom). 105

Figure A.1. Permission for Figure 1.2..... 129

Figure A.2. Permission for Figure 1.3..... 130

Figure A.3. Permission for Figures 1.4, 2.5 and 2.6..... 131

Figure A.4. Permission for Figures 2.1 and 2.4. 132

Figure A.5. Permission for Figure 2.3..... 133

Figure A.6. Permission for Figure 2.7..... 134

Figure A.7. Permission for Figure 2.9..... 134

Figure A.8. Permission for Figure 2.8..... 135

Figure A.9. Permission for Figure 2.11..... 136

LIST OF TABLES

Table 3.1. Dimensions of the test samples. 32

Table 3.2. The Material properties of AS4/8552 composite. 37

Table 3.3. Energy absorption of 0°, 90° plies and [0/90] sub-laminate..... 43

Table 3.4. Energy absorption of 0°, 45° plies and [0/45] sub-laminate..... 43

Table 3.5. The comparison of SEA values for different thicknesses. 48

Table 3.6. Computational times of FE models for different thicknesses. 54

Table 4.1. The SEA values of semi-circle specimens made of UD prepregs. 68

Table 4.2. The SEA values of sinusoidal specimens made of UD prepregs. 69

Table 4.3. The SEA values of flat specimens made of WF prepregs..... 71

Table 4.4. The SEA values of sinusoidal specimens made of WF prepregs. 73

Table 4.5. The SEA comparison between structures unidirectional and woven fabric prepregs..... 74

Table 5.1. SEA of nested structure and the difference from the single sinusoidal. .. 85

Table 5.2. SEA of corrugated structure and the difference from the flat plate. 88

Table 5.3. Three crash box designs. 90

Table 5.4. Comparison of the SEA performances of the three geometries. 98

Table 5.5. The SEA values of SL4 structures. 102

Table 5.6. Comparison between the SEA of tapered and non-tapered structures. ... 105

LIST OF SYMBOLS

C_d	Damaged elasticity matrix
d_1	Damage variable of fibre material
d_2	Damage variable of matrix material
d_{12}	Damage variable of shear factor
E_1	Elastic modulus in fibre direction
E_2	Elastic modulus in transverse direction
G_i^c	Fracture toughness for Mode-i
G_{ij}	In-plane shear modulus
K	Interface stiffness
l_{CZ}	Cohesive zone length
l_e	Element size
S	Shear Strength
S_c	In-situ ply shear strength
W	Total absorbed energy
X_C	Compressive strength in fiber direction
X_T	Tensile strength in fiber direction
Y_T	Tensile strength in transverse direction
Y_C	Compressive strength in transverse direction
ε_{11}	Fibre direction strain
ε_{22}	Transverse direction strain
μ	Friction coefficient
v_{ij}	Poisson's ratios
ρ	Density

σ_{11}	Normal stress in longitudinal direction
σ_{22}	Normal stress in transverse direction
τ_{12}	Shear Stress

LIST OF ACRONYMS/ABBREVIATIONS

CFRP	Carbon-Fiber-Reinforced Polymer
CZM	Cohesive Zone Model
CPU	Central Processing Unit
EV	Electrical Vehicle
FE	Finite Element
ICE	Internal Combustion Engine
MRCC	Manufacturer Recommended Cure Cycle
SEA	Specific Energy Absorption
UD	Unidirectional
WF	Woven Fabric

1. INTRODUCTION

The automotive industry is always under constant pressure to meet the growing demands raised by legislative requirements for better protective structures and safety performances. As one of the major health issues worldwide, more than 1.2 million people die due to vehicle crash every year [1]. Crashworthy structures, on the other side, can be designed to absorb impact energy in a controlled manner so that high decelerations, causing fatal injuries, are minimized in a crash event. These crashworthy components are also expected to be light in weight to satisfy fuel economy requirements to decrease greenhouse gas emissions.

Lightweighting is one of the major trends in automotive industry. For internal combustion engine (ICE) vehicles, every 100 kg of a weight reduction decreases the fuel consumption by 0.3 to 0.5 L per every 100 km which corresponds to 800 to 1100 g reduction of CO_2 emission [2]. In order to meet the future targets for clean designs, the developments of electric vehicles (EV) also accelerated. The sales volume of EVs is expected to increase by at least 35% by 2030 with the release of over a hundred new models [3]. Since additional electrical components such as batteries increases the weight of electric vehicles compared to the conventional ICE vehicles, weight reduction is still a requirement to increase the driving range with a single battery charge. According to the investigations, 10% increase in driving range can be achieved by 7.3% weight reduction [4]. Therefore, the growing demand for lightweight automotive components leads to an expansion of research for new materials having high strength-to-weight and high energy absorption-to-weight ratios.

Carbon fiber reinforced Plastic (CFRP) composites are stiff, strong, durable and have low densities which makes them 30 to 50% lighter than metal components. Their high fatigue and corrosion resistance make them also preferable in the industry. Moreover, due to their superior energy absorption potentials, composite materials are good candidates for crashworthy components [5]. When properly designed, the failure mechanisms of composite structures can be in a stable progressive form that makes crushing mechanism easy to control so that they can have many benefits over traditional metallic structures.

Figure 1.1 demonstrates the specific energy absorption capacities (the amount of absorbed energy per unit mass) of various materials [6]. Several types of composite materials have greater capacity of energy absorption on a per unit mass basis, as compared to more commonly used metals, such as steel and aluminium. Hence, it can be concluded that composites offer the potential to be used as very efficient energy-absorbing crash structures.

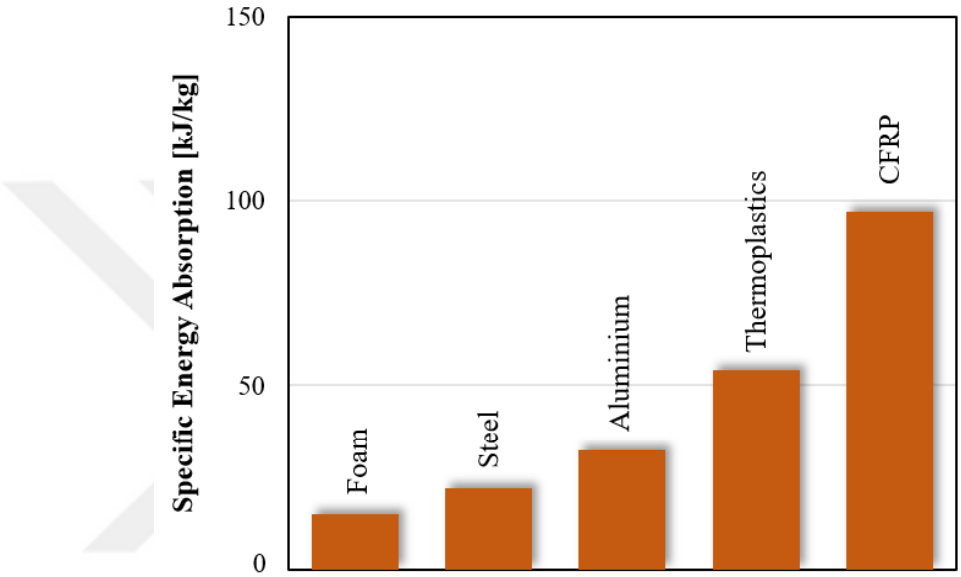

Figure 1.1. Specific energy absorption capacities for various materials (Plotted according to the information given in [6]).

When the energy absorbing components in a vehicle are considered, it is quite important to understand the difference of the crushing morphologies between conventional metallic and composite materials which indicates the difference in energy absorption levels. Figure 1.2 demonstrates the deformed state of steel and composite crash boxes used as an energy absorber at the front side frame of the vehicle. As can be apparently seen from the left side of the figure, in steel crash box, plastic folding process occurred which is the primary energy absorption mechanism of metallic structures [7].



Figure 1.2. Failure of crash box structures made of different materials: steel (left), composite (right) [7].

Right side of Figure 1.2 gives the failure of composite materials. Composite structures generally fail by progressive crushing under axial compression. When compared to steel crash box, smaller load oscillations are observed for composite structures, and this provides better energy absorption capability.

Instead of ductile failure modes observed in metals, fiber reinforced composites exhibit diverse failure mechanisms such as shear failure, tensile and compressive failure modes of fiber and matrix [8]. Besides, delamination is one of the predominant forms of failure for the laminated composite structures. Figure 1.3 shows the matrix and fiber failure modes subjected to loadings in different directions [9]. When a composite is subjected to compression perpendicular to the fiber direction, matrix failure occurs due to the crushing and interacting of fibers and matrix (see Figure 1.3a). Matrix crack propagates throughout the thickness in a plane where shear stress reaches its maximum value. When composite material subjected to tensile load in transverse direction, matrix failure again occurs due to the tensile failure of the matrix material or the failure of interface between the fibers and matrix. As illustrated in Figure 1.3b, the crack propagates perpendicular to the tensile loading. Figure 1.3c demonstrates the fiber failure as a result of the compression in longitudinal direction. Kink bands occur due to the exhibition of shear by matrix which results in “compressive fiber failure”. When fibers are subjected to tension in longitudinal direction, fiber breakage occur at their weakest cross sections (see Figure 1.3d). The applied shear loading, as depicted in Figure 1.3e, causes tensile stress on the 45° plane which leads a combination of tensile fiber and matrix failures as well as fiber-matrix debonding [10].

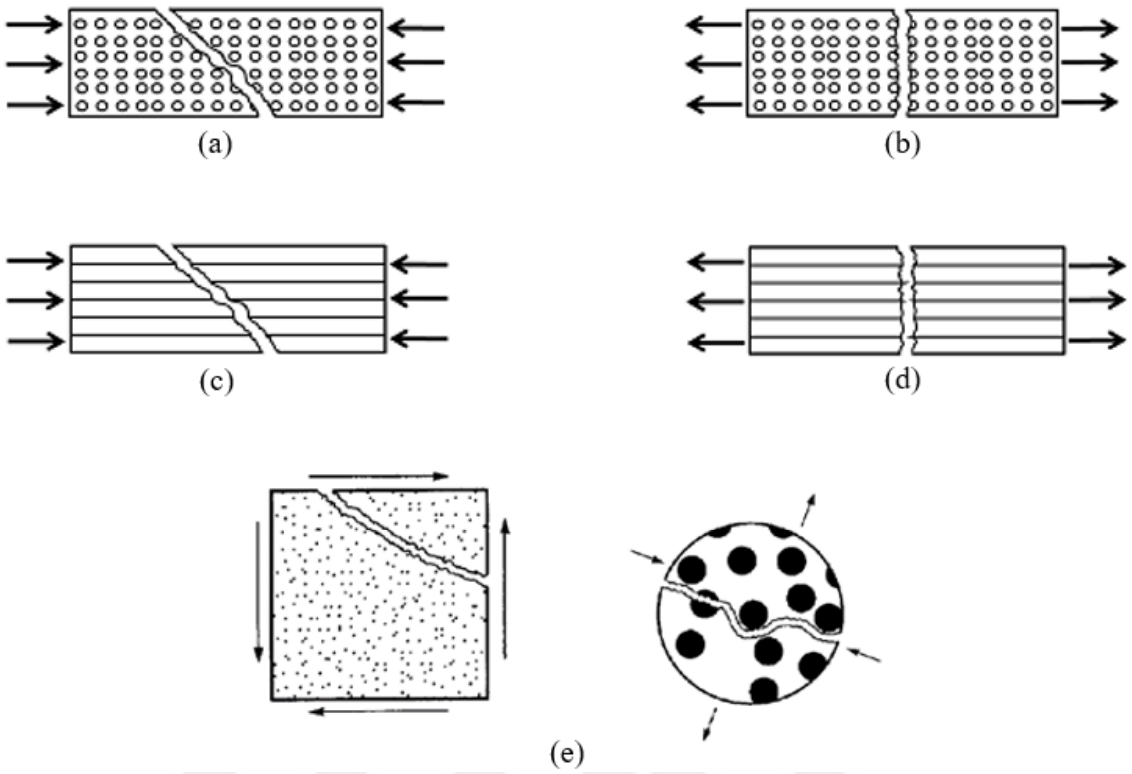

Figure 1.3. Failure modes: (a) Compressive matrix failure, (b) Tensile matrix failure, (c) Compressive fiber failure, (d) Tensile fiber failure, (e) Shear failure [9].

When it comes to failure of composite laminates, delamination is one of the most critical modes. Delamination, the separation of two adjacent plies, often preceded by a crack which propagates through a ply until it has reached the fibers of an adjacent ply. Figure 1.4 shows the delamination in a composite specimen [11].

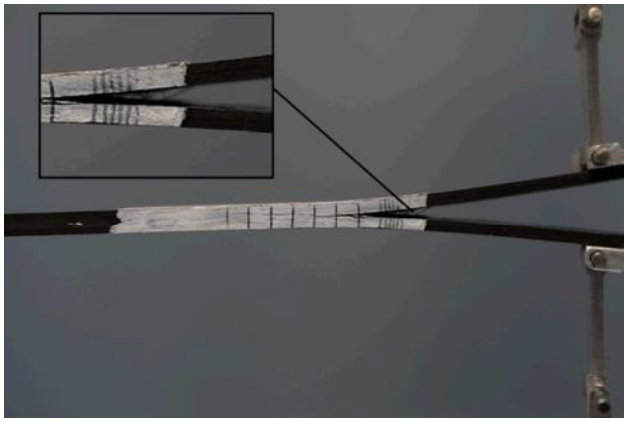

Figure 1.4. Delamination propagation in a CFRP specimen [11].

During the crushing process, composite structures absorb energy through a combination of abovementioned failure modes which take place in an order that may also vary according to several factors. This complexity of the crush failure mechanisms causes the energy absorption provided by a composite structure to be quite difficult to predict. There are several parameters that have direct influence on SEA and the crush induced failure mechanisms. Understanding how those parameters affect the failure mechanisms and so the energy absorption capabilities of composite structures under axial loading is quite significant for efficient designs. During last few decades, considerable number of experimental and numerical studies has been carried out to reach a better understanding. However, there are still several questions required to be answered.

2. LITERATURE REVIEW

2.1. Experimental Studies

Research, aiming to understand the behavior of composites undergoing crash failure, began in early 1980's. From that day to the present, there has been extensive literature about the energy absorption of composite structures. Most of the studies have focused on experimental analysis since the crush-induced failure mechanisms, including not only intralaminar but also inter-laminar damage modes, are quite complex and have not been fully clarified.

Prior to the literature review on the experimental investigation applied on progressive failure of composite structures, it is essential to understand the crushing of a composite specimen and discuss the parameters defining the energy absorption capability. As can be seen from the Figure 2.1, a progressive behavior of the crushing, triggered by a chamfered edge, is described at different stages for a cross-section of a tube with a basic lay-up of $[90/0]_{2S}$ [15]. In the first stage, the inner 90-degree layer is compressed, failed, and forced to move outwards. Then the middle axial (0-degree) layers are starting to contact with the rigid plate. Delamination also occurred at the center as mode I (opening mode) delamination and between the 90 and 0-degree plies, occurred most likely as mode II (shear mode) delamination. Finally, the outer 90-degree layer experiences bending and transverse shear cracks in the matrix.

A typical force-displacement curve of axial crushing is illustrated in Figure 2.2. There is an initial peak force, followed by stable crushing where the force remains at an almost constant level. The initial peak is higher because there have been no failure modes observed yet. There is a transition zone between the peak force and the stable crash zone which is highly dependent on how the crash is triggered.

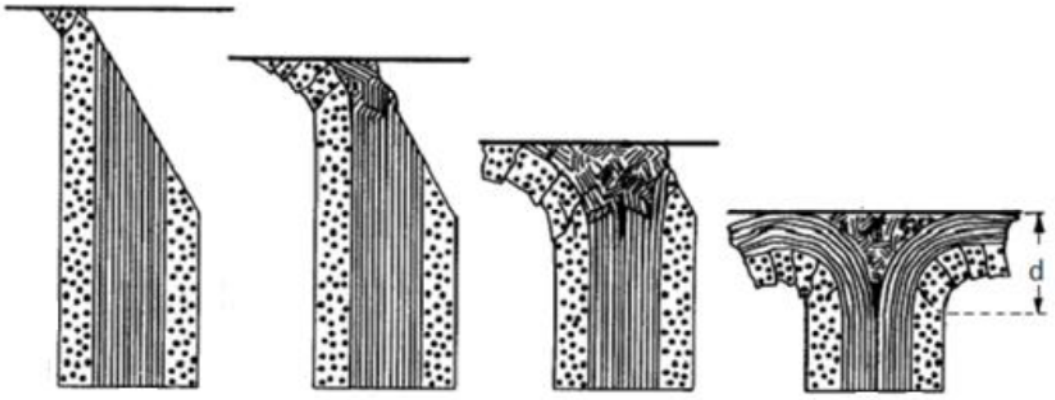

Figure 2.1. A schematic illustration of crushing of a tube with chamfered edge, modified from [15].

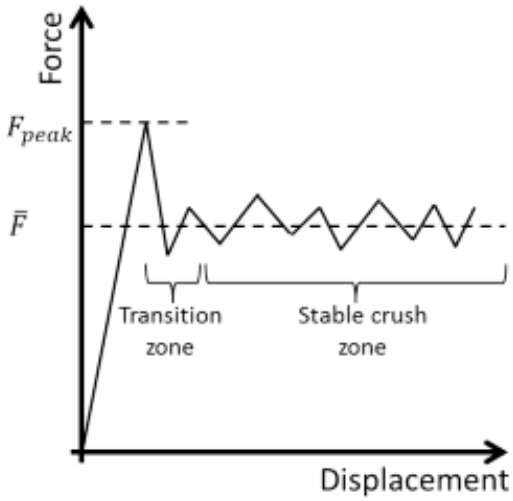

Figure 2.2. Typical force-displacement curve for a specimen subject to crushing.

The total energy, **W**, absorbed during process can be evaluated as the total area under the load-displacement curve which is expressed as

$$W = \int_0^{\Delta} F ds \,, \tag{2.1}$$

where Δ is the crush distance and F is the measured force.

The specific energy absorption, SEA is the total energy absorbed per unit mass that can be written as

$$SEA = W/\rho A l\,, \tag{2.2}$$

where ρ is the density, A is the cross-sectional area, l is the crushed length. For crushing process, the specific energy absorption is significant since the crashworthiness of a composite material is expressed in terms of its *SEA* and can be used to compare the performance of composite structures having different characteristics from various studies [12].

Most of the experimental research in literature conducted to understand the energy absorbing mechanisms of composite materials has focused on the crushing of thin-walled tubular structures because the manufacturing and testing of such self-supporting structures are much easier when compared to other complex designs. Besides, the crushing morphology and the crush-induced failure modes observed in tubes can be utilized to generalize and classify the deformation behavior of composite materials. Among all the studies focused on composite tubes, the view commonly shared that there are several different failure modes occurring simultaneously during crushing of composite materials, each of which absorbs different level for energy.

Farley and Jones [13] were among the first scientists who aim to provide a better understanding of energy absorption mechanisms occurring during the progressive crushing. In 1989, they presented three main failure modes which are “transverse shearing”, “lamina bending” and, “brittle fracturing”. In a later study of Farley and Jones [14], they concluded that “brittle fracturing mode” is actually a combination of “transverse shearing” and “lamina bending”. Moreover, all other failure modes observed during the crushing of composite structures are also the combinations of those two identified modes. The transverse shearing, depicted in Figure 2.3a, is characterized by longitudinal and short interlaminar cracks while lamina bending, depicted in Figure 2.3b, is characterized by long interlaminar, intralaminar, and parallel-to-fiber cracks. The main energy absorbing mechanism during the transverse shearing is the fiber breakage occurring at the edges of the lamina bundles. On the other hand, during the lamina bending, most of the energy is absorbed by the matrix cracks.

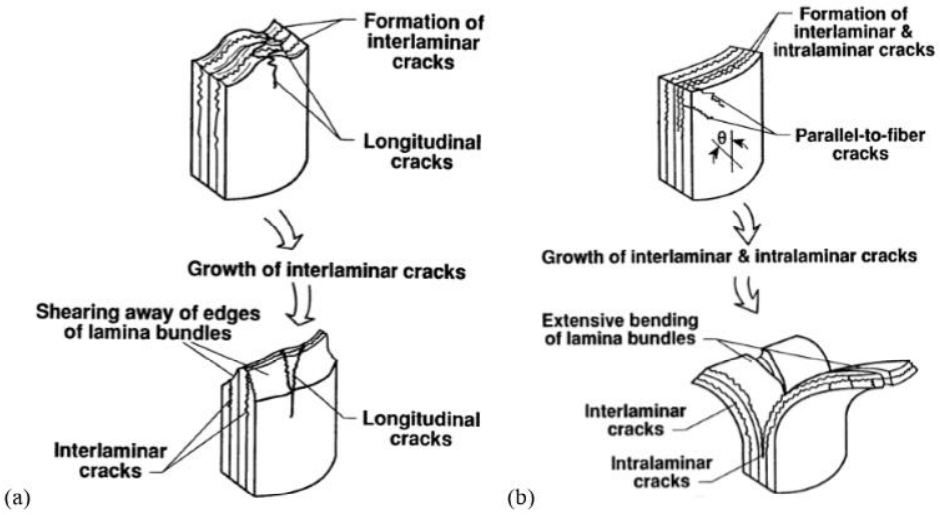

Figure 2.3. Main failure modes according to the Farley and Jones: (a) transverse shearing and (b) lamina bending failure modes of progressive crushing failure [14].

Hull [15] followed the work of Farley and Jones and identified two main failure modes during crushing event: “fragmentation” and “splaying” (see Figure 2.4). These two failure modes are actually the same with the modes presented by Farley et al. (Transverse shearing and lamina bending) [14]. The splaying mode is characterized by the delamination and matrix cracks that leads bending of plies without having major fiber breakage. The fragmentation mode is mostly characterized by fiber fracture and matrix cracking. Hull, on the other hand, does not give any information about the levels of dissipated energy from these failure modes.

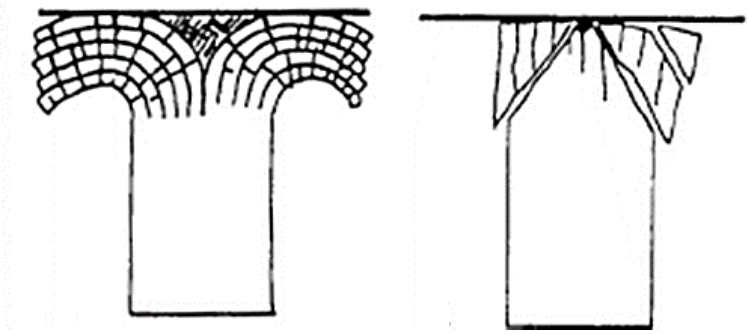

Figure 2.4. Schematics of the two failure modes identified by Hull: splaying mode (left) and fragmentation mode (right) [15].

In 1998, Carruthers [16] presents a review study comparing experimental work of composite tubular structures in which two main fracture modes (fragmentation and splaying) are identified. More importantly, in his study, Carruthers, demonstrated that the level of energy absorption from fragmentation mode is higher than the splaying mode since there are minimal amount of fiber breakage in splaying mode.

In 2009, Bisagni [17] stated that there are four main failure modes observed during the crushing of CFRP tubes which can be classified as tearing, socking, splaying and microfragmentation modes. Among all of these four modes (see from Figure 2.5), the microfragmentation mode seemed to be same failure mechanism as the "fragmentation mode" while the other three modes can be considered as different combinations of two main "fragmentation" and "splaying" modes which are both identified by Hull [15].

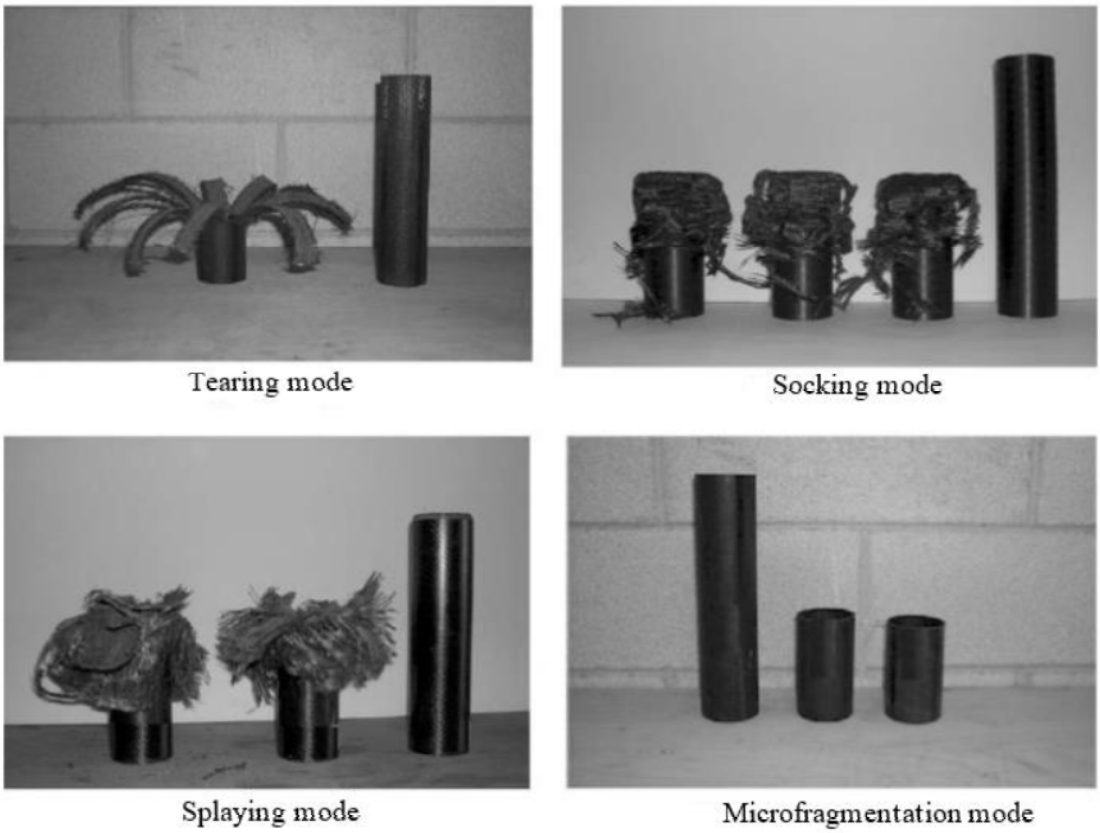

Figure 2.5. Four progressive crush failure modes as identified by Bisagni [17].

Recently Chen et al. [18] performed both quasi-static and dynamic experimental tests on CFRP circular tubes. At the end of the procedure, specimens demonstrate a similar crushing morphology as indicated by previous researchers which is the combination of two main failure modes: fragmentation and splaying. Failure modes identified by Chen are given in Figure 2.6. Apart from other studies, Chen et al. underlined the contribution of the friction on energy absorption by stating that the friction between the moving wall and the specimen dissipates approximately quarter of the total energy. The rest of this amount absorbed by the damage of CFRP tube; however, there is no information about the repartition of the energy for each failure mechanism.

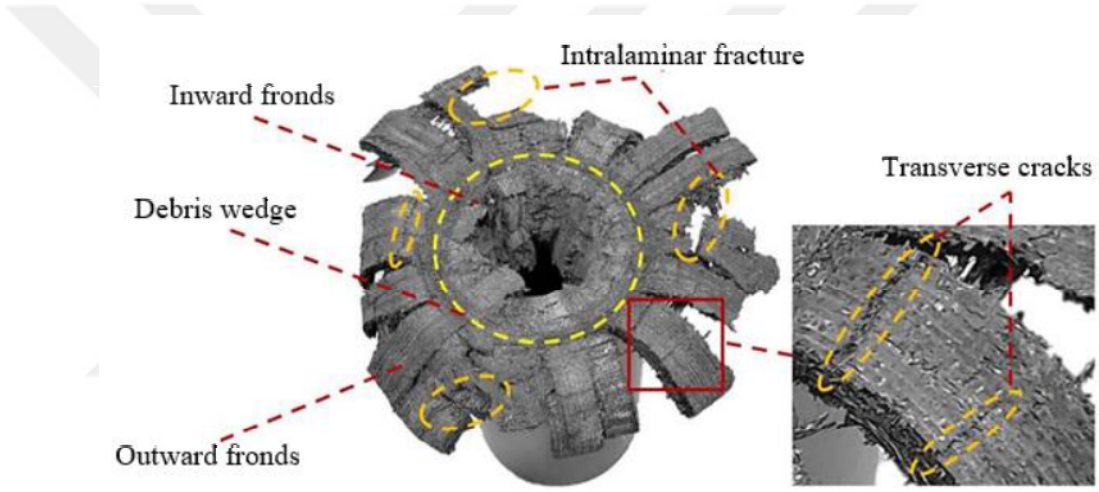

Figure 2.6. Failure modes identified by Chen et al. (Adapted from [18].)

Among the limited number of studies investigating the levels of energy absorption of different failure modes, Israr et al. [19] carried out both numerical and experimental investigations of the crushing process of CFRP plates and demonstrated that the fragmentation mode occurring due to the fiber breakage absorbs more energy than the other failure types such as delamination and splaying of layers.

To summarize the section presented so far, researchers are in a agreement that there are many failure modes occurring simultaneously during the crush event, each of which provides different capability of energy absorption, but a general disagreement also exists about which parameters affect these modes, and how their influence acts to define the dominant one. The dominant failure mode during the crushing of composite structures

depends on several factors, such as the selection of the material system, fiber orientation, the strain rate, and trigger mechanisms, which have been the subject of many studies in the past.

Across several experimental studies in which the influence of the selected material system has been investigated, it is widely agreed that carbon fiber reinforced composites absorb more energy than the composites reinforced with aramid and glass fibers [20-22]. The influence of fiber orientation on energy absorption capability is also investigated by various researchers; however, there is no consensus on the best lay-up. Ryzinska et al. [23] and Wang et. al [24] reported that using 15-degree UD plies leads the highest SEA value, where Farley and Jones [10] depicted that [0/45] or [±45] configurations absorb more energy than [0/15] or [±15] lay-ups. In contrast, Mahdi et al., using [60/-30] carbon/epoxy woven plies, obtained highest energy absorption performance for 20 mm crush [25]. Therefore, it is understood that the influence of fiber orientation on energy absorption can also be dependent on several other factors such as material type and geometric features. Crashworthiness studies showed that applying chamfered edge as a trigger mechanism is also necessary in order to prevent catastrophic failure occurring due to global buckling and to decrease the peak load. Without trigger mechanism, the progressive failure and continuous dissipation of energy cannot be possible. Although several crush triggers such as chamfered edges with different angles, saw tooth and steeples were designed in many studies, no consensus has been reached on which mechanism is the best [15, 26-29].

In recent years, the interest in flat composite coupon tests is increasing since they have an advantage of predicting the specific energy absorption (SEA) due to being easily manufactured that leads repeatable processes and test results with low margins of error and cost [19, 30-34]. Considering the numerous studies carried out on complex geometries (tubes, cones, and beams), the results from different studies are not suitable for comparison of material or lay-up performances since geometry also has a significant influence on the energy absorption capability of composite structures. Flat shaped composites, on the other hand, may provide a standardization so that the SEA can be easily obtained and compared for composite plates with different lay-ups and different mechanical characteristics. Moreover, these plates can also be a reference point for the estimation of energy absorption of complex structures.

The issue about the procedure for flat plates; however, is the requirement of a specialized supporting fixture to prevent potential buckling and ensuing catastrophic failure so that the crush failure modes can be clearly seen. Feraboli et al. [30] was one of the first researchers who designed a supporting mechanism to apply an experimental study for CFRP flat coupon plates. The fixture presented in Figure 2.7 was utilized to provide complete crushing of the specimen. As the upper rigid wall moves down, the specimen can slide between the knife edges and keep crushing for the total distance of the specimen. The fixture also introduces an unsupported length at the crush front which provides a region for free deformation. At the end of the study, it was found that if the unsupported length to the thickness ratio exceeds 6, flat plates start to fail unstably due to the observed buckling mode. Fixtures similar to the design developed in the study of Feraboli et. al [30] have been used to estimate the energy absorption capability of composite flat plates throughout the years. As one of the recent examples, Babaei et al. [35] conducted an experimental study for CFRP plates with a similar supporting mechanism to understand that the velocity and the mass of moving plate have no influence on the mean crushing load of the specimen as long as the overall impact energy remains same. The presented fixture design seemed to be convenient since it provides a complete crush of whole specimen; however, it has a major drawback of creating extra friction between the specimen and knife edges which may lead to inaccurate estimation of the energy absorption capability.

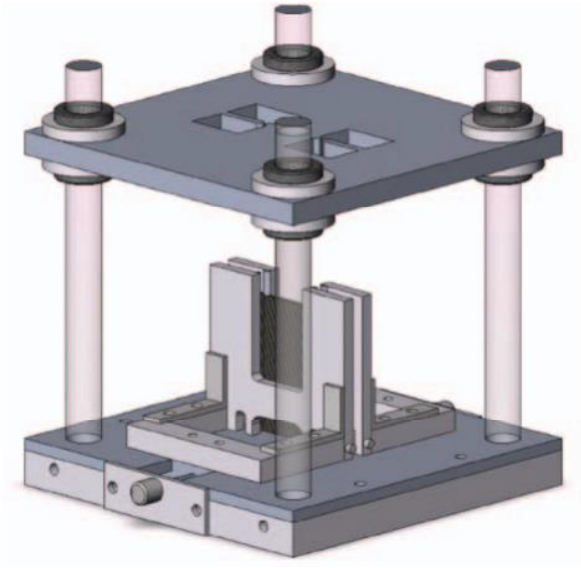

Figure 2.7. Flat coupon plate fixture proposed by Feraboli et al. [30].

Same problem is valid for the studies of Lausch et al.[33, 36] in which full lateral support is used that constrained flat plate specimens in each edge except upper side. Since the specimen is fully constrained during the deformation, in addition to expected failure modes, extensive ruptures occurred around the vertical supports which changes the levels of absorbed energy dramatically (see Figure 2.8). Although a technique is applied to identify and isolate the undesirable loads, the presented approach can mislead the failure mechanisms and prevents understanding of their relative contribution to the energy absorption. In order to prevent the problems caused by design complexities, a simple fixture can be more suitable for flat coupon tests.

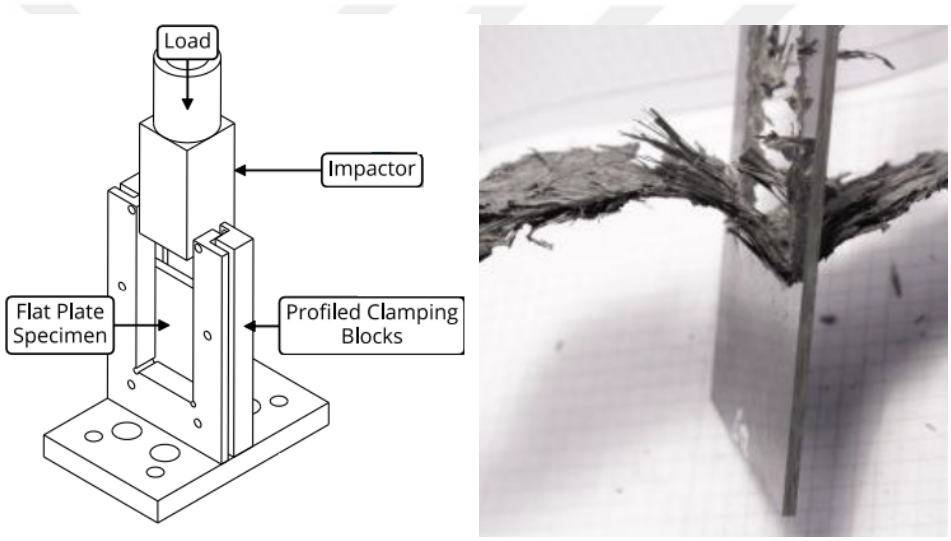

Figure 2.8. Experimental setup with full lateral fixture (left), crushed specimen (right) from the study of Lausch et al. [33].

Bru et al. [31] and Israr et al. [19] designed a simple support fixture restraining the specimen with an unsupported length which decrease during the crushing process. In study of Bru in which the influence of trigger mechanism on the SEA of unidirectional composite plates is investigated, the unsupported length should be maximum 4 times higher than the specimen thickness [31]. The limiting of crushed distance to a short range, on the other hand, does not cause any problems. Since the load required for the crush process stabilizes around a mean value after the peak load, the specified crushing distance is sufficient to predict the specific energy absorption. The design of the fixture and the placement of the specimen can be seen from the Figure 2.9.

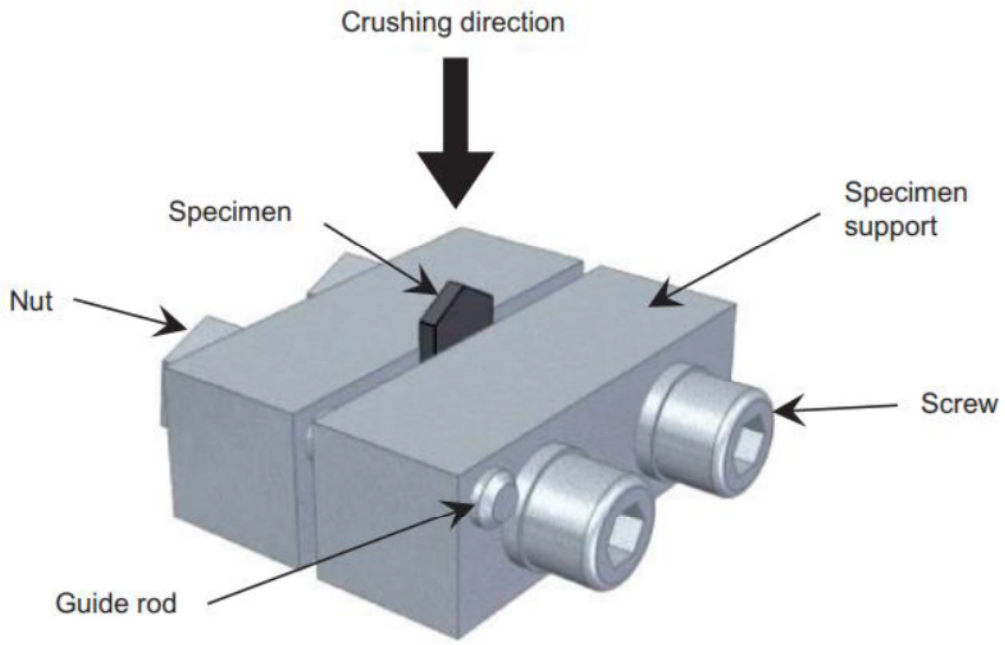

Figure 2.9. Simple support fixture presented by Bru et al. [31].

Although there are several studies focusing on energy absorption of composite flat plates to standardize the test method for SEA measurement of composite materials and to investigate the influence of parameters; there has been no work that correlates the output from coupon tests with the energy absorption capability of complex crash box structures.

Geometry is also one of the parameters that has a major influence on SEA. From the studies which have focused on closed geometric features such as tubular structures, Kindervater [37] and Mamalis et al. [38] both proved that circular tubes had better energy absorption performance than square composite tubes. In circular tubes, the diameter to thickness ratio directly affects the SEA value. According to the studies of Farley [39] and Mamalis et al. [40], it can be said that decreasing this ratio results in the increase in energy absorption. But the stated inverse proportion is only valid for the reasonable values of the tube thickness since overly thin and overly thick specimens have the tendency to fail catastrophically. Moving away from circular tubes, Farley and Jones [41] also stated that the energy absorption capability increases when the geometry becomes more elliptical. It is also known that corrugated designs such as sinusoidal geometries improve the energy absorption capability to a considerable extent. Among the limited number of studies consisting of

crushing tests of sinusoidal specimens, Hanagud et al. [42] exhibited that the sinusoidal geometry has a great potential in terms of energy absorption. Afterwards, Wiggenraad et al. [43] conducted a complete set of tests to understand the crashworthiness of subfloor composite sinusoidal structures designed for aerospace applications; however, the failure modes were not clearly identified, and the numerical attempts made to predict the crushing behavior were not quite successful. Sokolinsky et al. [44] then tested the crushing response of carbon/epoxy corrugated sinusoidal plates. However, this study has focused on only the validation of the numerical analysis with the experimental data obtained from one specific geometry. No discussion has been made on the failure modes occurring during the crushing process and how these modes affect the energy absorption capability of the structure. Overall, among the numerous studies focusing on the crashworthiness of different composite geometries, there has been no work conducting a systematic study to understand the influence of geometry on energy absorption capability, starting from flat plates to complex structures. Moreover, the change of failure modes with different geometries and the relationship between these modes and the amount of absorbed energy have been still unclear.

2.2. Numerical Studies

Predicting failure in composites is quite complicated. In some cases, composites may be able to sustain significantly larger load than that predicted by considerations of failure initiation alone (first ply failure). However, in order to fully exploit the design benefits of these materials, designers should be able to model the progressive damage growth. Each constituent of the composite materials fails progressively. Order of the failure of the constituents and ultimate stress and strain at failure is dependent upon the type of fiber and matrix, layup sequence, volume fraction and other such manufacturing related parameters. Due to the influence of several parameters on SEA performance of composites, wide variety of progressive failure outcomes can be obtained for composite structures with different characteristics. That is why, it is not easy to estimate the crushing behavior of composite structures through numerical analysis which should consider not only intralaminar failure mechanisms (in plane failure), but also interlaminar failure mechanisms (delamination).

The FE models suitable for the crash simulations of composite structures contain three parts: the elastic region defined by constitutive law, the failure initiation criteria and damage evolution which includes the post-failure damage with stiffness discount. As represented in the Figure 2.10, for all of the damage modes including matrix and fiber failures under tension and compression, the material response is first linear in the elastic region which is valid until the damage initiation and then softening region takes place.

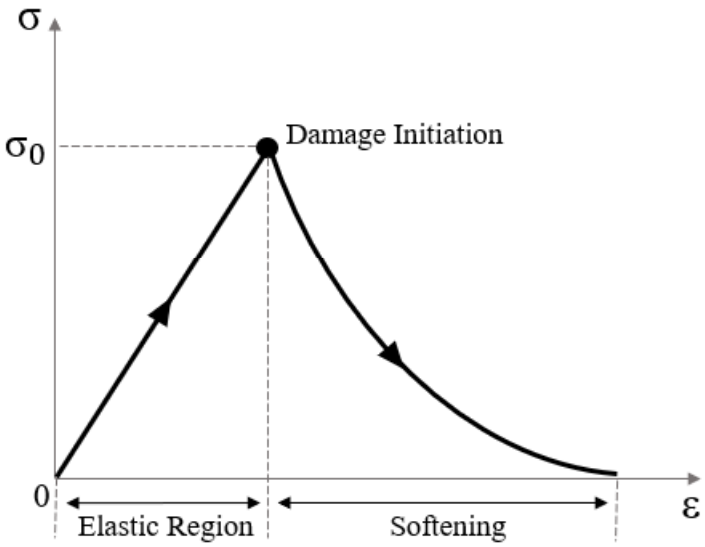

Figure 2.10. General schematic of damage propagation.

The elastic model uses plane stress stress-strain relations based on Hooke's Law and orthotropic constitutive properties measured from standardized material property experiments. Hooke's Law is expressed as

$$\begin{Bmatrix} \varepsilon_1 \\ \varepsilon_2 \\ \gamma_{12} \end{Bmatrix} = \begin{pmatrix} 1/E_1 & -v_{12}/E_1 & 0 \\ -v_{21}/E_2 & 1/E_2 & 0 \\ 0 & 0 & 1/G_{12} \end{pmatrix} \begin{Bmatrix} \sigma_1 \\ \sigma_2 \\ \tau_{12} \end{Bmatrix} . \tag{2.3}$$

In this expression, E_1 and E_2 are the Young's modulus in the fiber direction and the direction perpendicular to the fibers, G_{12} is the shear modulus, v_{12} and v_{21} are Poisson's ratios of the material.

Developing the accurate criterion to estimate the failure initiation within composites have been one of the major topics in the research field for decades [45-47]. As one of the early attempts, the maximum stress criteria have been commonly used for composite failure initiation since these criteria can be adapted to separate modes required due to the nature of composite failure: fiber and matrix failure under tension and compression [48]. The conditions for the failure initiation included in the criteria can be demonstrated as

Tensile fiber failure for $\sigma_{11} \geq 0$ $$\left(\frac{\sigma_{11}}{X_T}\right) \geq 1 \quad (2.4)$$

Compressive fiber failure for $\sigma_{11} < 0$ $$\left(\frac{\sigma_{11}}{X_C}\right) \geq 1 \quad (2.5)$$

Tensile matrix failure for $\sigma_{22} > 0$ $$\left(\frac{\sigma_{22}}{Y_T}\right) \geq 1 \quad (2.6)$$

Compressive matrix failure for $\sigma_{22} < 0$ $$\left(\frac{\sigma_{22}}{Y_C}\right) \geq 1 \quad (2.7)$$

Shear failure $$\left(\frac{\tau_{12}}{S}\right) \geq 1, \quad (2.8)$$

where σ_{11} and σ_{22} are normal stresses in fiber and transverse directions while τ_{12} symbolizes shear stress. X_T and X_C are fiber direction tensile and compressive strength values. Y_T and Y_C are transverse tensile and compressive strength; and S symbolizes the shear strength. The maximum stress criterion is linear and most basic criterion in which failure initiates when the stress components in longitudinal, transverse and shear directions are higher than the identified strength value in corresponding directions. These strength values are measured from the tension, compression, and shear tests of composite coupon specimens. However, the maximum stress criteria do not consider the interaction between stress components. Hashin failure criteria is one of the major initiation criteria taking the interactions between stress components into account and have been widely used in numerical models.

In 1980, as an elevated version of maximum shear stress criteria, Hashin created the quadratic formula [49] by adding in-plane shear terms making the estimation of failure initiation in unidirectional composite laminates more accurate for four distinct modes. Hashin's failure criteria can be expressed as

Tensile fiber failure for $\sigma_{11}\geq 0$ $$\left(\frac{\sigma_{11}}{X_T}\right)^2+\left(\frac{\tau_{12}}{S}\right)^2\geq 1 \quad (2.9)$$

Compressive fiber failure for $\sigma_{11}<0$ $$\left(\frac{\sigma_{11}}{X_C}\right)^2\geq 1 \quad (2.10)$$

Tensile matrix failure for $\sigma_{22}>0$ $$\left(\frac{\sigma_{22}}{Y_T}\right)^2+\left(\frac{\tau_{12}}{S}\right)^2\geq 1 \quad (2.11)$$

Compressive matrix failure for $\sigma_{22}<0$ $$\left(\frac{\sigma_{22}}{2S}\right)^2+\left[\left(\frac{Y_C}{2S}\right)^2-1\right]\frac{\sigma_{22}}{Y_C}+\left(\frac{\tau_{12}}{S}\right)^2\geq 1. \quad (2.12)$$

Chang-Chang's modification of Hashin's failure criteria has been widely utilized in literature which improves the fiber-matrix shearing term [50]. The matrix failure criteria derived by Chang-Chang can be written as

$$\left(\frac{\sigma_{22}}{Y_T}\right)^2+\frac{\frac{(\tau_{12})^2}{2G_{12}}+\frac{3}{4}\alpha(\tau_{12})^4}{\frac{(S_c)^2}{2G_{12}}+\frac{3}{4}\alpha(S_c)^4}\geq 1, \quad (2.13)$$

where G_{12} is shear modulus, S_c is the in-situ ply shear strength that needs to be measured from a cross-ply laminates. The new parameter α is a constant which has to be obtained by experimentally.

Normally, for the transverse compressive loading, 45-degree cracks are expected to occur in matrix throughout the thickness where shear stress reaches its maximum value. However, some experimental studies proved that this angle could reach up to 55 degrees [51] and the reason was explained by the existence of a friction stress acting in the matrix cracks. In order to consider the current outcomes and get more realistic estimations, first Puck and Shürmann [51] and then Davila et al. [52] developed a new criterion for matrix compressive failure which is a Mohr-Coulomb criterion-based formula including several extra parameters such as friction coefficient that can be demonstrated as

for $\sigma_{22}<0$ $$\left(\frac{\tau_T}{S_T-\mu_T\sigma_{22}}\right)^2+\left(\frac{\tau_L}{S_L-\mu_L\sigma_{22}}\right)^2\geq 1, \quad (2.14)$$

where σ_{22}, τ_T and τ_L are the normal and shear stresses in the fracture plane; S_T and S_L are shear strengths in transverse and longitudinal directions. The symbols μ_T and μ_L are friction coefficients in transverse and longitudinal directions.

Pinho et al. [53] then modified the latest version of Puck's criterion to create 3D failure criteria in which the fiber kinking in the fiber compression mode has also taken into consideration. The attempts made by Puck, Davila, and Pinho to define mode-based lamina failure lead good agreement with test results and failure performance. However, like Chang-Chang's modification, their criteria require unique experimental testing and curve fitting to find the parameters involved within, it was mostly evaluated as challenging [54].

For all of the previously mentioned failure initiation criteria, it is possible to state that each of the newly developed approach has some advantages over the previous one such as being more consistent and adaptable to a wider scope in certain respects. However, their implementation in finite element software programs, should also be taken into consideration. As one of the early approaches, Hashin's failure criteria, for instance, is embedded in ABAQUS/Explicit software so that it can be applied easily without any requirement of user defined subroutine. Although Hashin criteria is known to lead some inaccuracies for three-dimensional models, when the two-dimensional model is developed for UD composites, it is found to be the simplest model that appropriately captures failure modes successfully [55].

Following initial lamina failure, each composite material model must also specify a damage model to degrade the performance of the material until ultimate failure is specified. FE models based on Continuum Damage Mechanics (CDM) are currently very popular for the failure evolution in composite materials. CDM was initially suggested by Kachanov [56], and then improved by Lemaitre and Chaboche [57] in which material damage is defined using internal state variables contained in a set of equations which allow the material to remain a continuum with field equations. The internal damage variables are incorporated into the material constitutive equations to degrade the material performance as damage progresses. Talreja et al. [58] was one of the early researchers which utilizes a CDM model for composite failure, and further examples of CDM models have been given in following years [59-66]. Donadon et al. [59], Falzon et al. [60-62] and recently Boyina et al. [63] developed CDM based three-dimensional (3D) model to investigate the failure throughout the thickness of each composite ply. In each of these models, damage factors are introduced into the ply stress-strain equations which have an inverse relationship with the material constitutive properties. This has the effect of degrading the ply stresses following failure according to the damage evolution function defined by the material model. The analysis

continues until the stress is degraded to zero. When it reached to zero, this means that failure is totally completed.

Besides in-plane failure, delamination is another predominant form of failure since especially under axial loading, the energy is absorbed by delamination process to a considerable extent. In the case of axial crash, instead of single mode, mixed-mode delamination occurs containing opening and shearing modes. Therefore, it is required to apply a general formulation dealing with mixed-mode delamination onset and propagation (see Figure 2.11.) [67-69].

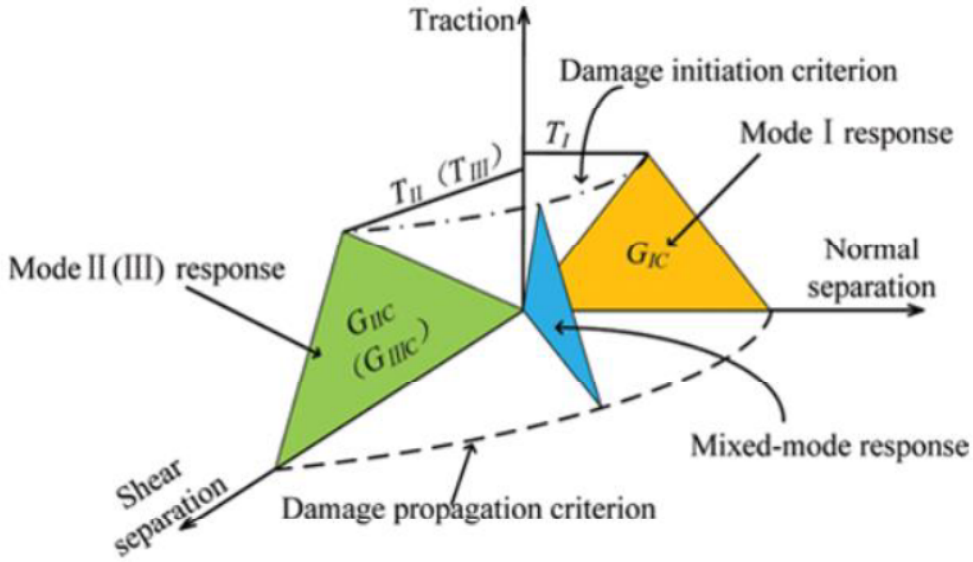

Figure 2.11. Mixed-mode delamination [68].

Cohesive Zone Model (CZM) was developed in which decohesion elements predict the onset of the softening process at the interface between plies by strength-based approach and by using fracture mechanics to predict delamination propagation. The primary study on CZM can be traced back to the works of Barenblatt [70] and Dugdale [71] on the fracture behavior around the crack tip in brittle materials and steel. Hillerborg et al. [72] combined fracture mechanics with FEA to obtain more realistic results on crack formation and evolution. The CZM considers a cohesive zone (process zone) ahead of the crack tip to count for crack initiation and extension by using sets of constitutive equations such as traction-

separation laws. The traction-separation laws associate the opposing tractions of the cohesive zone to the opening displacements. Depending on the crack opening mode (Mode I, II or III), the traction-separation laws are defined based on initial stiffness, maximum traction, interfacial strength and the area under the stress-displacement curve which is considered as the critical energy release rate G_c [73]. Different forms of traction-separation laws exist but the linear elastic-linear softening behavior is commonly selected to be implemented in the simulations as can be seen from Figure 2.11. The constitutive laws for the delamination initiation and the softening can be seen as

$$\left(\frac{\sigma_{\mathrm{I}}}{\tau_{\mathrm{I}}}\right)^2+\left(\frac{\sigma_{\mathrm{II}}}{\tau_{\mathrm{II}}}\right)^2+\left(\frac{\sigma_{\mathrm{III}}}{\tau_{\mathrm{III}}}\right)^2=1 \tag{2.15}$$

$$\left(\frac{G_{\mathrm{I}}}{G_I^c}\right)^{\propto}+\left(\frac{G_{\mathrm{II}}}{G_{\mathrm{II}}^c}\right)^{\propto}+\left(\frac{G_{\mathrm{III}}}{G_{\mathrm{III}}^c}\right)^{\propto}=1, \tag{2.16}$$

where τ_{I}, τ_{II} and τ_{III} are interfacial strength values of Mode-I, Mode II and Mode-III. G_I^c is normal fracture toughness; G_{II}^c and G_{III}^c are shear fracture toughness values for Mode-II and Mode-III respectively. G_{I} is the normal strain energy release rate, G_{II} and G_{III} are shear strain energy release rates for Mode-II and Mode-III respectively.

During the crushing of composite structures under axial compression, the global nonlinear behavior observed requires accurate modelling strategy. Explicit FEA codes are robust computational schemes for dealing with the nonlinear behavior which are used in several commercial finite element software. In literature, there are several studies based on numerical simulation of composite structures by using LS-DYNA [74-80]. Mamalis et al. [75], for example, simulated the crash response of CFRP square tubes made of hybrid sandwich material and there was a satisfactory consistency between the experimental and numerical results. Hörmann and Wacker [76] used the LS-DYNA explicit code to simulate thermoplastic crash boxes. Both studies used modified Chang–Chang failure model for the individually extruded shell layers. A continuum damage mechanics (CDM) based simulation in LS-DYNA was also applied by Kiani et.al. [77] to estimate the energy absorption capability in the crushing process of glass fiber reinforced tubes. Sensitivity of the critical material parameters defined for shell elements were discussed. Recently Liu et al. [78] modelled the crushing response of CFRP multi-cell complex structures by using the orthotropic material model MAT54 which is based on again Chang-Chang failure criteria.

The main problem about the Chang-Chang criteria embedded in LS-DYNA is the requirement of non-physical parameters which can be found by conducting the unique experiments.

Many researchers have also made major efforts in FEA software ABAQUS/Explicit to increase the accuracy of numerical analysis applied for crushing of composites. Indermuehle et al. [81] simulated the performance of composite cone structure in ABAQUS/Explicit including the common failure modes of delamination, fracture, and matrix damage. By implementing a continuum damage mechanics approach using the constitutive model in ABAQUS/Explicit, a VUMAT user subroutine was utilized for the material damage. As another example for accurate results between test and simulations in ABAQUS, Sokolinsky et al. [44] investigated the crushing behavior of composite sine wave beam made of carbon/epoxy TORAYCA fabric. Continuum shell elements were used and delamination is simulated by using Cohesive Zone Model. Falzon et al. [82] performed the simulation of flat wedge-shaped specimen made of unidirectional CFRP prepregs by using two methods: the built-in damage model based on Hashin failure criteria and an in-house VUMAT subroutine. While the load-displacement curves obtained from FE analysis by implementing VUMAT subroutine showed good agreement with the experimental morphologies, the FE results predicted the SEA of the specimen almost %20 less then the actual data. Moreover, it was stated that the simulation was terminated at early stages due to the excessive distortion occurring in an element. In the FE analysis, the premature termination can be actually prevented by several methods such as mesh size regulations, applying mass scaling and hourglass control. Since other methods mostly require extra parameters that should be obtained by extra tests, isn't it possible to get accurate results by only utilizing the Hashin's Criteria? Jahani et al. [83], for example, used modified Hashin Criteria to predict damage initiation in the crushing process of CFRP tubular structures in ABAQUS/Explicit. The numerical results were in consistency with the test data.

Although advances in commercial Finite Element Analysis (FEA) software have enabled engineers to realistically simulate the performance of composite components, computational cost is still an issue for numeric studies. The reason why explicit dynamic finite element simulations require long execution times is directly related to the method of solving the system of equations during the crushing of composite structures. In

Abaqus/Explicit, corresponding equation of motion is solved within small time steps, each of which should not exceed the amount of time stress waves take to propagate across the dimension of one element. That is what explicit modelling makes “stable”. In a complex model such as crushing event, these time steps can become much smaller, thereby resulting in long computational times [84].

Some regulations are applied to the FE models to artificially decrease the run times. One strategy is to apply mass scaling to the extruded structure. Since the maximum preferable time step is directly proportional to the density of the composite material, artificial increase in the mass leads higher critical time step [85]. Another approach is to model half or quarter of the geometry with symmetry conditions [86]. Another strategy is to increase the velocity of moving plate; however, in this case artificially increasing the loading rate may differ the load response of the structure due to the strain rate dependency. That is why, one should apply these strategies carefully [44].

Apart from the aforementioned approaches, Turon et al. [87] focuses on mesh size increase to decrease run time for which interlaminar properties are adjusted to eliminate instabilities and obtain accurate results. Although this is a successful and beneficial attempt, it should be noted that the increasing mesh size alone is not enough to provide meaningful gains in terms of computational costs, especially for the complex geometry models. Lately, some researchers performed studies applying CZone add-on module for Abaqus, in which crush stress parameters obtained from experimental coupon tests are used as an input [88,89]. CZone leads run time efficiency but the extra material data is required which might be unavailable. All in all, enhanced and accurate modelling methods leading feasible computational (CPU) costs are still required.

2.3. Summary, Problem Statement and Objectives

Predicting the progressive crushing behavior of composite structures is a complex phenomenon since there are many distinct failure modes occurring simultaneously during the crush event, each providing a different energy absorption capability. Furthermore, the

types and occurrence order of the failure mechanisms during the process depend on several factors such as the selection of the material system, fiber orientation, thickness, trigger mechanisms, etc. As explained in the previous section, despite the extensive literature of experimental and numerical studies, it is still unclear how these parameters affect failure modes and determine the level of absorbed energy.

Geometry is one of the parameters that have a significant influence on the SEA of composite structures. The variation of geometry, directly affecting the failure modes, leads a prominent difference in the energy absorption performance. In literature, there have been various studies focusing on CFRP composite structures with different geometric features. However, it is impossible to compare the energy absorption capabilities of these geometries presented in separate studies since each structure has mostly different characteristics in terms of material, fiber orientation and thickness which also have an influence on SEA. More importantly, there has been no work conducting a systematic study to understand the influence of geometry on energy absorption capability, starting from simple coupon plates to complex structures.

Most of the crashworthiness studies conducted for the composite structures have included experimental studies. Experimental methods, however, are time consuming and expensive. Therefore, there is a growing interest in commercial Finite Element Analysis (FEA) programs which enable engineers and researchers to simulate the crushing process of composite structures and to design structures having superior energy absorption performance at lower costs. FE Models conducted for the crushing process of composite structures, on the other hand, cannot always provide accurate estimations due to the complex nature of the crushing process of composite structures including not only intralaminar failure mechanisms (in plane failure), but also interlaminar failure mechanisms (delamination).

When it comes to numerical analysis of the crushing process of complex composite structures, computational cost is still an important issue that needs to be dealt with. Explicit dynamic FE simulations require long execution times due to small time steps utilized to solve system of equations. Although there are some attempts made in numerical studies to decrease run times, accurate modelling methods leading feasible computational (CPU) costs are still required.

Based on the problems summarized above, main objectives of this thesis are listed as follows:

- to provide a better understanding of the relationship between the energy absorption capability and the failure mechanisms occurring during the crushing process.
- to investigate the influence of thickness and stacking sequence on SEA of composite flat plates.
- to conduct a systematic study, investigating the crushing process from flat plates to complex structures to understand the influence of geometry on SEA.
- to identify how failure modes change with various geometric features and the relationship between these modes and the energy absorption capability.
- to apply same procedure by using laminates using unidirectional and woven CFRP material to investigate how failure modes and the SEA performance resulting from these modes change for structures as the material system changes.
- to propose a novel FE modelling approach for the progressive failure of composite plates in which computational cost is reduced considerably while obtaining accurate estimations of energy absorption capability during the crushing process.
- to design and manufacture a novel self-supporting composite crash box structure having higher energy absorption capability by taking all previously obtained results into consideration.

2.4. Organization of the Thesis

Chapter 3 will present the experimental and numerical investigation of the crushing process of AS4/8552 flat coupon plates. Cross-ply and angle-ply specimens with number of plies of 8, 12 and 16 are manufactured and tested in order to understand and discuss the failure mechanisms occurring during the crushing process in detail and the influence of plate thickness on SEA. In this section, conventional FE model for the progressive failure of AS4/8552 plates under quasi-static axial loading are developed in ABAQUS/Explicit and the results are compared with the experimental data.

Due to the simplicity in its nature, the utilization of composite flat plates in numerical analysis provides less complex modelling and great opportunity to improve FE models having lower run times. Chapter 3 presents a novel numerical approach for the crushing process of AS4/8852 flat coupon plates in which computational cost is decreased by reducing the number of interfaces between plies by a sub-laminate approach and modifying the interlaminar and lamina properties. Moreover, to demonstrate the validity of novel FE model for different stacking sequences and to investigate the influence of fiber orientation, same procedure is applied to an angle ply laminate with a stacking sequence of $[0/45/0/-45]_s$.

In Chapter 4, the influence of geometry on the SEA of AS4/8552 carbon/epoxy composite structures is investigated through various geometries such as flat plate, semi-circle, and sinusoidal specimens. By keeping the cross-sectional area (weight) constant, sinusoidal structures with different number of curvatures and diametral sizes are tested and their energy absorption capabilities are compared. In addition to experimental tests, a Finite Element (FE) Model is developed in ABAQUS/Explicit for sinusoidal structures to estimate SEA numerically. For the accurate prediction of the crushing behavior and the failure mechanisms, the idea of artificial plug-initiator is incorporated into the FE Model. By utilizing the validated FE Model, further sinusoidal designs having more curvatures are simulated and the sinusoidal structure having the highest energy absorption capability is identified. In this chapter, novel cost-effective numerical approach developed for flat plates is also applied to the crushing process of sinusoidal structures to show the validity of FE model for the complex geometries.

Last but not least, in order to understand how the relationship between the geometry and the absorbed energy varies when a different material system is used, Chapter 4 also presents the manufacturing and testing of the flat and sinusoidal specimens made of a woven fabric prepreg. The SEA results obtained from the crushing process of woven fabric composite structures are compared with the results of structures made of unidirectional composite and the differences in failure mechanisms are discussed in detail.

Chapter 5 includes the manufacturing, testing and simulation processes of a novel crash box geometry designed by considering all the outcomes obtained from previous sections. First, the influence of nesting and adding T-joints on SEA is investigated experimentally by using unidirectional carbon/epoxy material. Then, several design attempts in ABAQUS/Explicit are made merging a couple of sinusoidal structures with T-joints. The final geometry performing highest energy absorption capability is manufactured and tested under quasi-static compression. The results are compared with the numerical analysis in terms of load-displacement data and the observed failure mechanisms. During the crush event, it is expected from a crashworthy structure to absorb as much energy as possible, but the same time not to create high level of initial peak load since this leads an excessive deceleration causing a fatal damage on the passengers. Therefore, in the final part of this chapter, the new version geometry of geometry, in which the edges are tapered to decrease initial peak load, is presented. This tapered geometry is tested, and the results are compared with the previous one.

Finally, in Chapter 6, whole investigation process is summarized including the discussion about future work and possible improvements in design and manufacturing of proposed composite crash box.

3. EXPERIMENTAL AND NUMERICAL INVESTIGATION OF COMPOSITE FLAT COUPONS

The idea of utilizing flat coupons to investigate the crashworthiness of composites is highly efficient since they can be easily manufactured without any requirement of special tooling. Moreover, FE models applied for the crushing process of flat plates has also an advantage of having reasonable run times compared to crushing simulations of complex structures. Therefore, both numerical and experimental studies aiming to characterize the influence of parameters on SEA can be applied in a short amount of time. Besides, due to the simplicity in its nature, progressive failure of flat plates provides a great opportunity to propose and validate new cost-effective modelling approaches that can be used as a basis for the crushing models of complex structures.

This chapter presents the experimental and numerical investigation for the crushing process of unidirectional flat coupons conducted for a better understanding of failure mechanisms and their influences on the energy absorption capability. First, the experimental study for the cross-ply composite plates is presented and the results and main failure mechanisms are going to be discussed. The influence of plate thickness on SEA is also included in this section. Secondly, FE analysis of flat plates including both conventional and novel numerical approaches are going to be presented. By applying conventional FE models for the crushing process of composite flat plates in ABAQUS/Explicit, it is aimed to estimate not only energy absorption capability but also the crush-induced failure mechanisms in a good agreement with the experiments. The novel numerical approach is developed and presented for the crushing process of flat plates in which computational cost is decreased by reducing the number of interfaces between plies and modifying the interlaminar and lamina properties. Moreover, by modelling the plates with a stacking sequence of $[0/45/0/-45]_s$, the validity of novel FE model for different stacking sequences is demonstrated.

It should not be forgotten that every material system leads different specific energy absorption results due to the accompanying failure modes during the crash event and the influence of parameters also varies by selected material. Therefore, it is quite important to

broaden the horizons of the studies on crashworthiness with different fiber-matrix combinations. In this thesis work, AS4/8552 carbon fiber/epoxy composite material is selected which was not considered in any crashworthiness study before.

3.1. Experimental

The flat plate specimens are manufactured from Hexcel AS4/8552 carbon-epoxy UD prepregs with 198 g/m^2 areal weight. During the preparation process of the cross-ply specimens, 8, 12 and 16 plies of prepregs are stacked with $[0/90]_{ns}$ lay-up on the flat steel mold where n is selected as 2,3 and 4. Moreover, 8 plies of prepregs are stacked with $[0/45/0/-45]_s$ configuration again on the same flat mold. Stacking sequences for $[0/90]_{2s}$ and $[0/45/0/-45]_s$ plates are demonstrated in Figure 3.1.

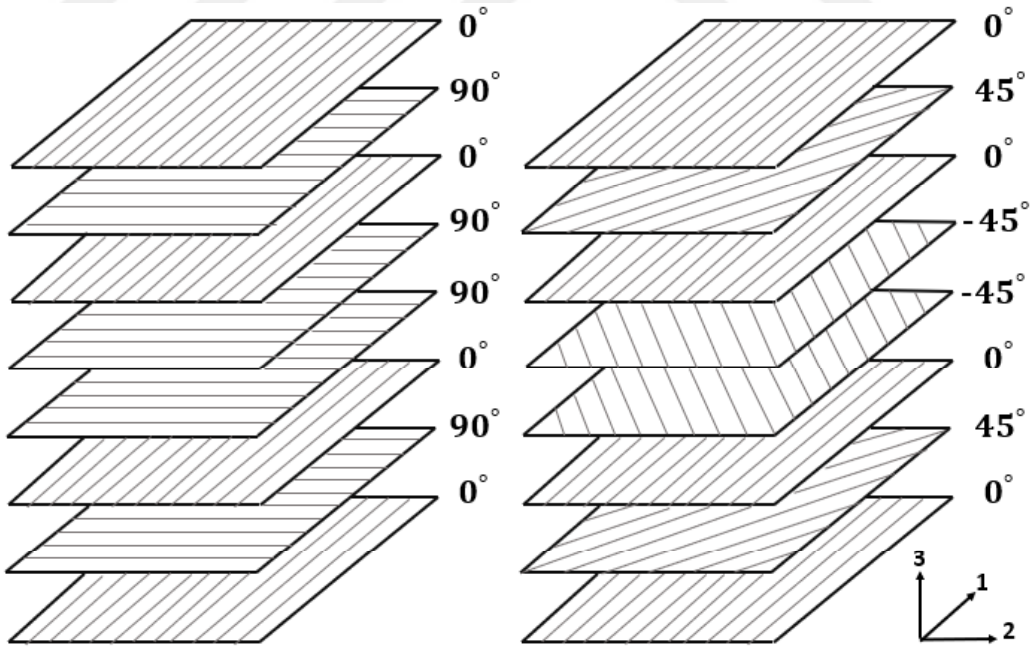

Figure 3.1. Schematics of stacking sequences of composite plates: [0/90]2s (left) and [0/45/0/-45]s (right).

Prepared laminates are vacuum bagged, and the manufacturing process is carried out in an autoclave, shown in the Figure 3.2, in the Composites Laboratory at Boğaziçi University according to the Manufacturer's Recommended Cure Cycle shown in Figure 3.3 [90].

The curing process involves a series of steps that are necessary for a composite material to achieve the desired properties. As can be seen from Figure 3.3, the initial step involves heating the specimen from ambient temperature to 120 °C at a constant rate of 2°C/min, followed by a 1-hour dwell period at the current temperature. In third step, gelation takes place, the temperature raised to 180 °C at a heating rate of 2 °C/min. In the following step, the specimen is held at 180 °C for a further 2 hours in which the vitrification is completed. Then, the specimen is cooled down to ambient temperature, thus completing the cycle.

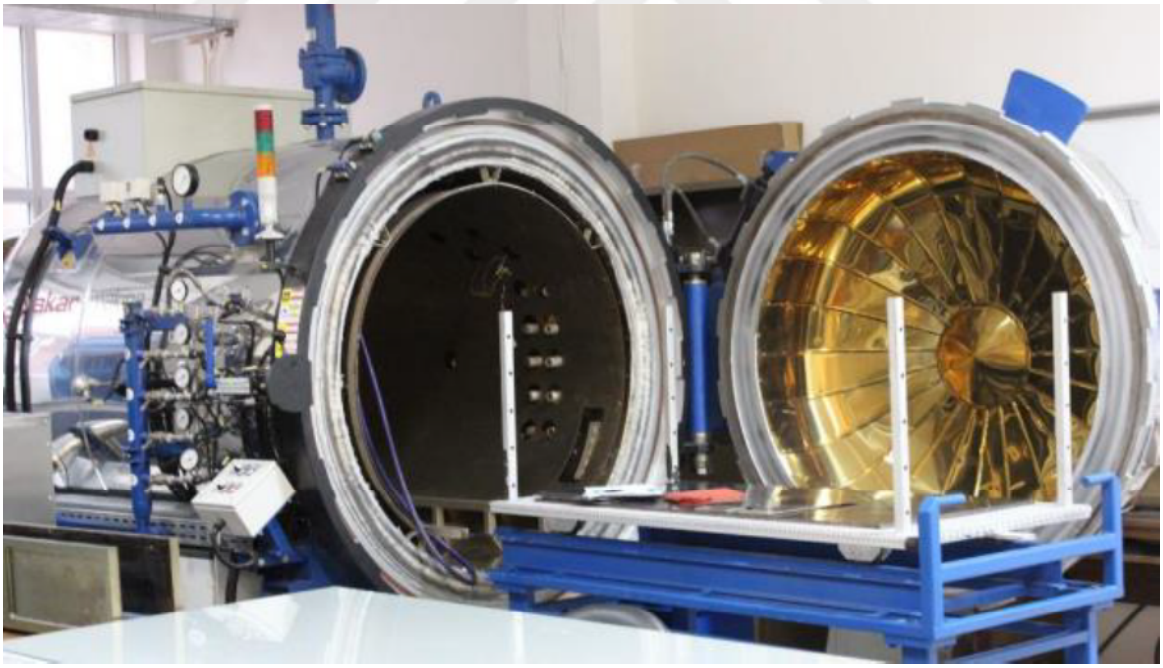

Figure 3.2. Autoclave in Composites Laboratory at Boğaziçi University.

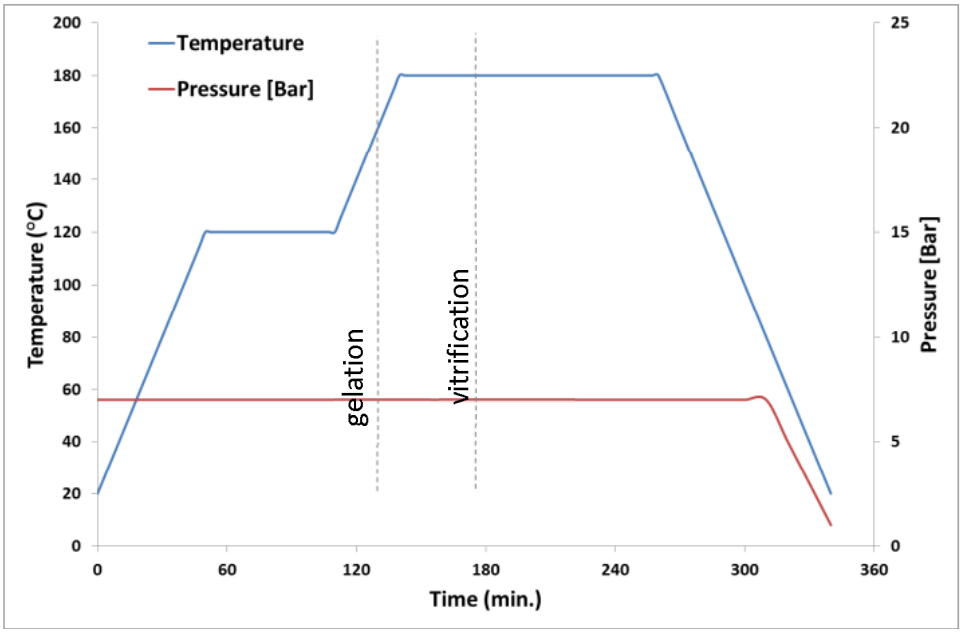

Figure 3.3. Manufacturer recommended cure cycle for AS4/8852 [90].

300 mm x 300 mm plates thus manufactured are then cut by a diamond disk cutter into final test coupons. The upper edge of the coupon is required to be chamfered to ensure progressive failure by delamination initiation and prevent catastrophic damage. Among all these studies conducted for the crushing of composite flat plates, there is no standard or cooperation for the definition of chamfer angle. Therefore, 45° chamfered edge is selected and applied, since it is simple to manufacture with the cutting tool. 45° chamfered edges are then polished by emery paper and inspected visually for possible delamination. It was observed that the cutting operation does not cause any damage in the specimens. Three specimens are tested for each lay-up, dimensions of which are given in Table 3.1.

Table 3.1. Dimensions of the test samples.

Lay-up	# of plies	Thickness [mm]	Width [mm]	Length [mm]	Unsupported Length [mm]
$[0/90]_{2s}$	8	1.47	20	56	6
$[0/90]_{3s}$	12	2.20	20	59	9
$[0/90]_{4s}$	16	2.94	20	62	12
$[0/45/0/-45]_{s}$	8	1.47	20	56	6

A simple fixture with 50 mm length is designed to avoid buckling and provide a supporting system. The illustration of the fixture, the specimen with chamfered edge and the test setup are presented in Figure 3.4. The determination of the unsupported length is significant as it may cause buckling if the dimension is higher than a certain critical value [91]. According to some researchers [31,91], the unsupported length to thickness ratio should vary between approximately 2 and 4. To ensure the stabilization around a mean value in load-displacement curve after peak load, the ratio is specified to be approximately 4. The unsupported length and the specimen lengths are defined according to this specified ratio (see Table 3.1).

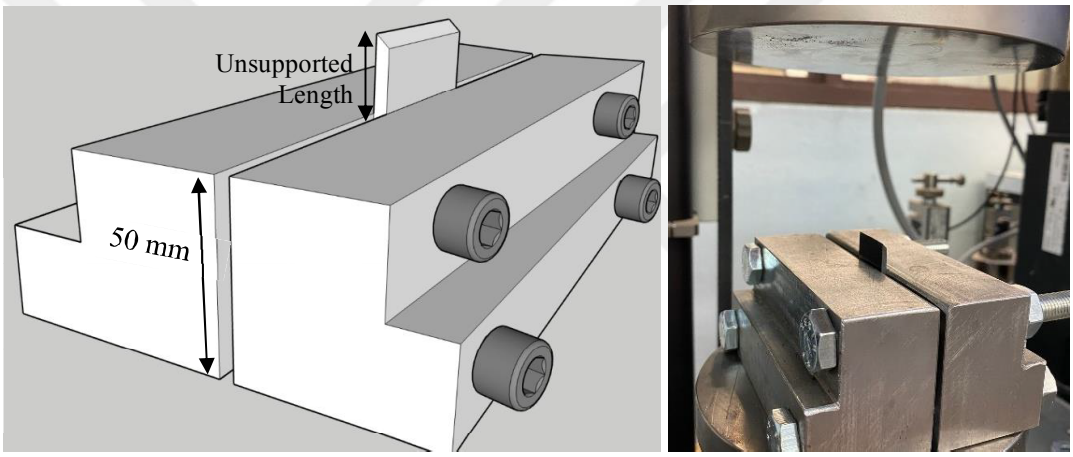

Figure 3.4. The illustration of the specimen and the supporting fixture (left), test setup (right).

As can be seen from the Figure 3.4, the end of the specimen is in contact with the base plate to avoid problems related to slip of the specimen inside the fixture. Bolts are tightened with a light hand tightening to avoid excessive compressive stresses in the grip region. The function of the fixture is just to provide support for buckling without applying extra clamping forces.

Specimens are tested in the Zwick Z100 testing machine with quasi-static speed of 0.5 mm/min as applied in the study of Bru et al [31]. The tests are ended manually before crushing plate compresses the specimen fixture. Load and displacement data is measured from the load cell and the crosshead of the testing machine, respectively.

3.2. Numerical

3.2.1. Conventional Model

For the numerical analysis to simulate crushing of AS4/8552 carbon fiber/epoxy flat coupons, a progressive failure model is developed by using ABAQUS/Explicit software consisting of both intralaminar and interlaminar damage mechanisms. For $[0/90]_{ns}$ specimens, generalized plane strain conditions are applied to the model and only one element is generated throughout the unit thickness of 1 mm. On the other hand, full FE model without plain strain or symmetry conditions is constructed for $[0/45/0/-45]_s$ flat coupons in order to allow rotation of 45° plies to get realistic and accurate results.

In all models, each ply having 0,184 mm thickness is individually extruded and meshed by using continuum shell elements (SC8R). Continuum shell elements in ABAQUS have the geometry of a three-dimensional solid element but their kinematic and constitutive behavior are similar to those of conventional shell elements. Boundary conditions are applied to be coherent with experimental procedure as can be seen from Figure 3.5.

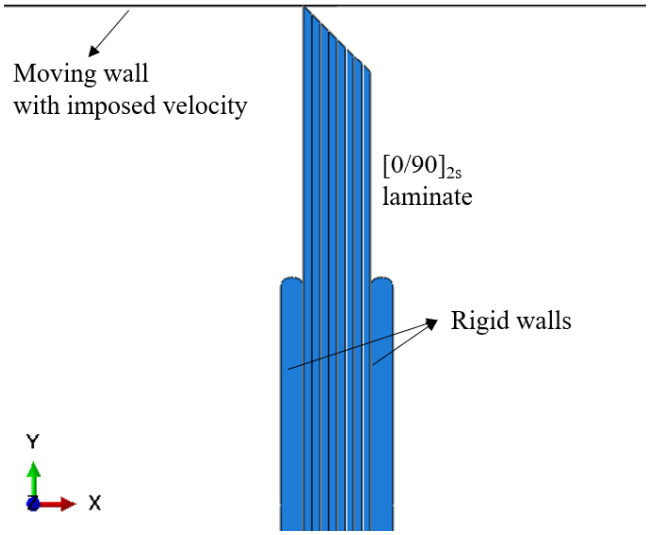

Figure 3.5. ABAQUS/CAE model of the composite flat plates with rigid side walls.

The in-plane response of the composite plies is modelled according to the Hashin damage criteria [49] as a homogeneous orthotropic material, which is capable of sustaining progressive stiffness degradation due to fiber/matrix cracking. Failure initiation criteria can be demonstrated as

Tensile fiber failure for $\sigma_{11}\geq 0$ $$\left(\frac{\sigma_{11}}{X_T}\right)^2+\alpha\left(\frac{\sigma_{12}}{S}\right)^2\geq 1 \quad (3.1)$$

Compressive fiber failure for $\sigma_{11}<0$ $$\left(\frac{\sigma_{11}}{X_C}\right)^2\geq 1 \quad (3.2)$$

Tensile matrix failure for $\sigma_{22}>0$ $$\left(\frac{\sigma_{22}}{Y_T}\right)^2+\alpha\left(\frac{\sigma_{12}}{S}\right)^2\geq 1 \quad (3.3)$$

Compressive matrix for $\sigma_{22}<0$ $$\left(\frac{\sigma_{22}}{2S}\right)^2+\left[\left(\frac{Y_C}{2S}\right)^2-1\right]\frac{\sigma_{22}}{Y_C}+\left(\frac{\sigma_{12}}{S}\right)^2\geq 1, \quad (3.4)$$

where σ_{11} and σ_{22} are normal stresses in fiber and transverse directions while σ_{12} symbolizes shear stress. X_T and X_C are fiber direction tensile and compressive strength values. Y_T and Y_C are transverse tensile and compressive strength; and S symbolizes shear strength. The behavior of the material after damage onset is determined by damage evolution that is characterized by the degradation of material stiffness. The response of the material is computed from

$$C_d=\frac{1}{D}\begin{bmatrix}(1-d_1)E_{11} & (1-d_1)(1-d_2)v_{21}E_{11} & 0\\ (1-d_1)(1-d_2)v_{12}E_{22} & (1-d_2)E_{22} & 0\\ 0 & 0 & (1-d_{12})G_{12}D\end{bmatrix}, \quad (3.5)$$

where $D=1-(1-d_1)(1-d_2)v_{12}v_{21}$, E_{11} and E_{22} are Young's modulus in fiber and transverse directions. G_{12} is the shear modulus, and v_{12}, v_{21} denotes the Poisson's ratios. The symbols d_1, d_2 and d_{12} represent the current state of fiber, matrix, and shear damages.

In the progressive damage algorithm of Abaqus, even if one type of damage completed, the element is not deleted unless all other damage variables reach to 1. This damaged, but not deleted elements can still bear some load; however, they have a mostly negligible effect on energy absorption capability. On the other hand, the influence of these elements on the crushing morphology during the deformation can be an issue to overcome.

Besides in-plane failure, delamination is another predominant mode of failure that should also be considered in numerical analysis of composite structures. The mixed-mode delamination containing opening and shearing modes are applied to the interaction surfaces between unidirectional plies according to the Cohesive Zone Method (CZM). CZM utilizes the general formulations for the relation between the cohesive surface tractions and separations that can capture delamination initiation and progress under mixed-mode conditions [68]. Different forms of traction-separation law are given in Figure 3.6 in which δ^0 denotes the critical opening displacement for damage onset [68].

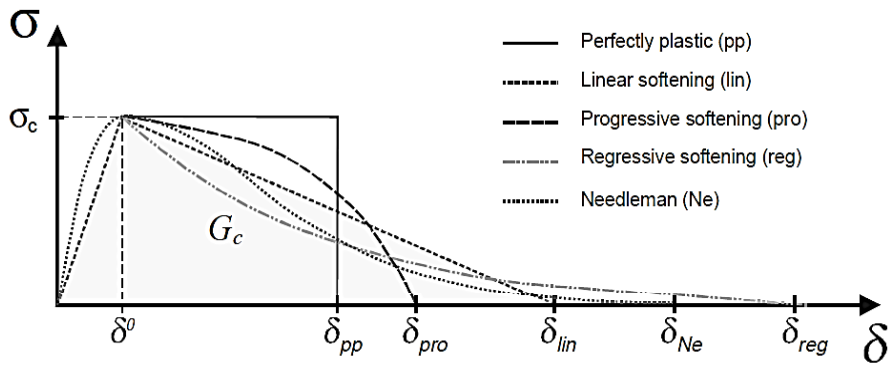

Figure 3.6. Various forms of traction-separation curves [68].

In ABAQUS/Explicit, the damage initiation is calculated by quadratic formula given in Equation 3.6. Linear softening damage law is used for the cohesive damage softening with the mixed-mode fracture energy criteria based on Power Law that can be seen as:

$$\left(\frac{\sigma_{\mathrm{I}}}{\tau_{\mathrm{I}}}\right)^2+\left(\frac{\sigma_{\mathrm{II}}}{\tau_{\mathrm{II}}}\right)^2+\left(\frac{\sigma_{\mathrm{III}}}{\tau_{\mathrm{III}}}\right)^2=1 \tag{3.6}$$

$$\left(\frac{G_{\mathrm{I}}}{G_I^c}\right)^{\propto}+\left(\frac{G_{\mathrm{II}}}{G_{\mathrm{II}}^c}\right)^{\propto}+\left(\frac{G_{\mathrm{III}}}{G_{\mathrm{III}}^c}\right)^{\propto}=1 \tag{3.7}$$

where τ_{I}, τ_{II} and τ_{III} are interfacial strength values of Mode-I, Mode II and Mode-III. G_I^c is normal fracture toughness; $G_{\mathrm{II}}^c$and G_{III}^c are shear fracture toughness values for Mode-II and Mode-III respectively. G_{I} is the normal strain energy release rate, G_{II} and G_{III} are shear strain energy release rates for Mode-II and Mode-III respectively. The input properties required for the modelling of elastic behavior, in-plane failure, and the delamination of AS4/8552 carbon/epoxy plies are listed in Table 3.2 [90, 92, 93].

Table 3.2. The Material properties of AS4/8552 composite [90, 92, 93].

Description	Unit	Variable	Value
Density	g/cm^3	ρ	1.58
Longitudinal Modulus	GPa	E_{11}	141
Transverse Modulus	GPa	$E_{22} = E_{33}$	9.75
Principal Poisson's Ratio	-	v_{12}	0.267
Shear Moduli in 1-2 Plane	GPa	$G_{12} = G_{13}$	5.2
Shear Moduli in 2-3 Plane	GPa	G_{23}	3.19
Longitudinal Tensile Strength	MPa	X_T	2200
Longitudinal Compressive Strength	MPa	X_C	1500
Transverse Tensile Strength	MPa	Y_T	81
Transverse Compressive Strength	MPa	Y_C	260
In-plane Shear Strength	MPa	S	80
Interfacial Strength (Mode I)	MPa	τ_{I}	35
Interfacial Strength (Mode II and III)	MPa	$\tau_{\mathrm{II}} = \tau_{\mathrm{III}}$	70
Fracture Toughness (Normal)	[kJ/mm^2]	G_I^c	0.28
Fracture Toughness (Shear)	[kJ/mm^2]	$G_{\mathrm{II}}^c = G_{\mathrm{III}}^c$	2.59

The interfacial strength parameter for MODE I delamination, τ_{I} given in Table 3.2 is an extrapolated value to be able to use larger elements as suggested in the study of Turon et al. [87]. This study proposed a modelling approach for cost-effective simulations which is based on an artificial increase of the cohesive zone length by lowering the interfacial strength so that larger elements can be utilized. According to Turon, Cohesive zone length, l_{CZ}, the distance between the crack tip and the element with maximum traction, should be bigger than element size. l_{CZ} is formulated as:

$$l_{CZ} = ME\frac{G_c}{(\tau^0)^2} \quad , \tag{3.8}$$

where E is the elastic modulus, G_c is the critical energy release rate, τ^0 is the maximum interfacial strength and the constant value for M depends on the selected cohesive zone model. M is selected as one according to study of Hillerborg et al. [72]. The minimum number of elements, N_e, required in cohesive zone to obtain more accurate stress distribution within this zone in FE model, is not well addressed. Falk et al. [94] have assigned 2-5 elements and Turon et al. have suggested 4 elements. This leads us to calculate the required element size, l_e that can be expressed as

$$N_e = \frac{l_{cz}}{l_e} \geq 4 \quad . \tag{3.9}$$

To eliminate this computationally inefficient barrier caused by assigning super fine mesh, Turon suggests the reduction of maximum interfacial strength to enlarge the cohesive zone length. The value of the interfacial strength, τ^0, required for desired number of elements within the cohesive zone, N_e, is derived from Eq. 3.8 and Eq. 3.9 which can be given as:

$$\bar{\tau}^0 = \sqrt{\frac{EG_c}{N_e l_e}} \quad . \tag{3.10}$$

The desired size of the elements utilized in numerical analysis of the crushing behavior of AS4/8552 plates is selected as 1 mm. That is why, the required interfacial strength is calculated from the equations given above as 35 MPa. Using this interfacial strength value should ensure that there are sufficient number of one-millimeter elements in cohesive zone length. In order to verify this outcome, a 2D numerical model is developed to simulate Double Cantilever Beam (DCB) tests in ABAQUS.

Figure 3.7 shows the FE model consisting of 1 mm sized elements and also the applied boundary conditions. The deformed state of the 2D DCB model is demonstrated in Figure 3.8.

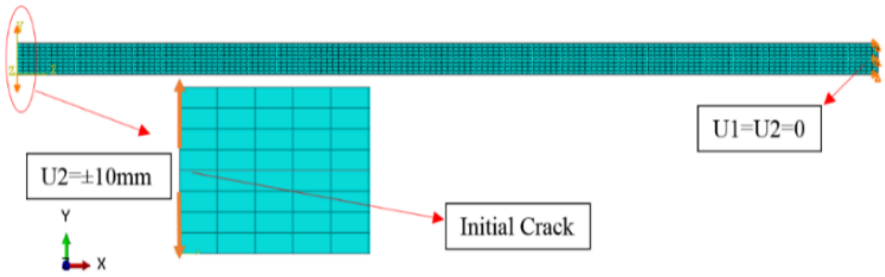

Figure 3.7. Mesh and boundary conditions for 2D DCB model.

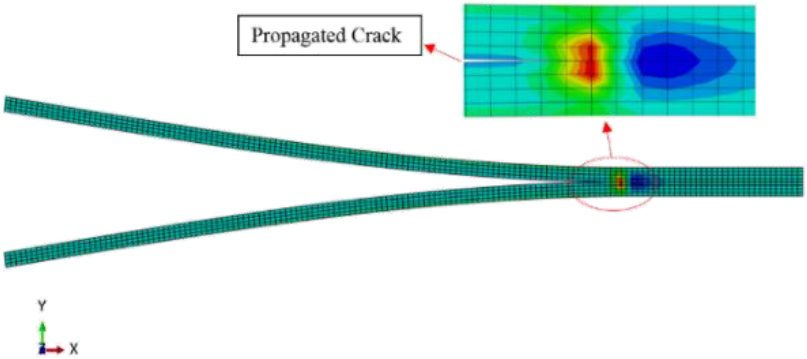

Figure 3.8. Deformed state of the 2D DCB model.

The required material properties for the model are utilized from the Table 3.2. When the numerical results are compared with the experimental data obtained from the applied DCB Tests for AS4/8552 laminates, element size of 1mm with reduced interfacial strength by as 35 MPa has been found to represent the load-displacement curve during testing as shown in Figure 3.9. Satisfying results have been captured with reduced interfacial strength and a coarser mesh when compared to experimental test.

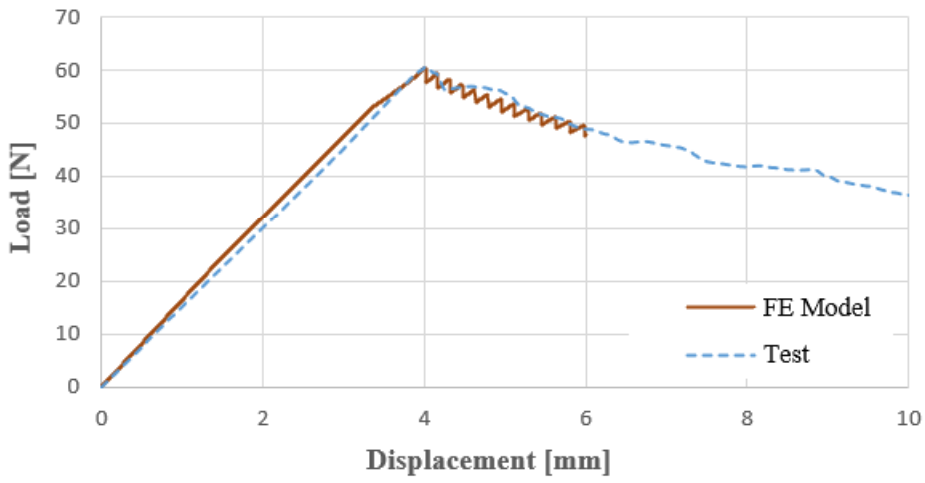

Figure 3.9. The Load- Displacement responses of experimental and numerical DCB tests.

After applying Turon's work and finding consistent strength result for 1 mm element size, the process of deciding on all the parameters needed for the model to work properly was completed. Other relevant details of the conventional FE model for the crushing process of the composite cross-ply and $[0/45/0/-45]_s$ plates are given as follows:

- The velocity of rigid upper wall is defined as 200 mm/s.
- Total step time of the analysis is defined according to velocity of moving wall and the desired crushing distance. For 4 mm displacement, step time is defined as 0.02 s.
- The friction coefficient between the composite specimen and the moving upper wall, which plays a significant role for the consistency, is taken to be 0.3 as suggested in Sokolinsky et al. [44].
- The coefficient of friction between plies is decided to be 0.15 after several trial-and-error runs.
- Mass scaling with the factor of 10^2 is applied to the composite structures which is a technique of artificial mass increase of the structure to obtain a larger time step that leads lower run times [95].

3.2.2. Novel Numerical Approach to Decrease Computational Cost

As discussed in previous chapter in detail, decreasing run times for the numerical models with some parametric regulations such as increasing mesh sizes or mass scaling are inadequate so that radical solutions are required especially for more complex structures, run times of which can be tedious. In this study, a novel modelling approach that leads reasonable run times is developed. The method proposes to model only one interface between every two plies with cohesive elements instead of one interface between each ply of the structure. Thus, original model for n-ply structure requires n-1 interfaces whereas modified model requires only n/2-1 interfaces.

Modelling idea for flat specimen with 8 plies is shown in Figure 3.10. In this model, four [0/90] sub-laminates are modelled with one element through the thickness instead of eight individual plies. Each [0/90] sub-laminate is modelled by one continuum shell element composite lay-up with Hashin Damage parameters. By doing this, the number of the interfaces is reduced, and the number of elements is decreased as compared to the original model. However, to reach accurate results in compliance with the experimental data, both in-plane and interlaminar properties used in FE model should be modified by using a heuristic method.

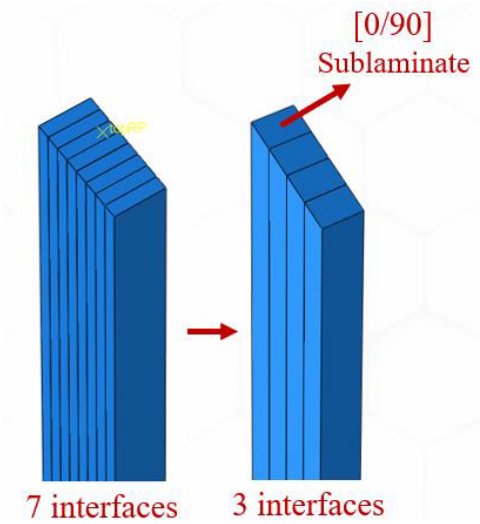

Figure 3.10. Modelling idea for novel numerical approach.

At that point, it is quite important to understand how and why some parametric adjustments are required in terms of failure mechanisms and nature of the crash event. As adapted from the study of Israr et al. [19], Figure 3.11 gives the repartition of energy during the crushing of cross-ply composite plates.

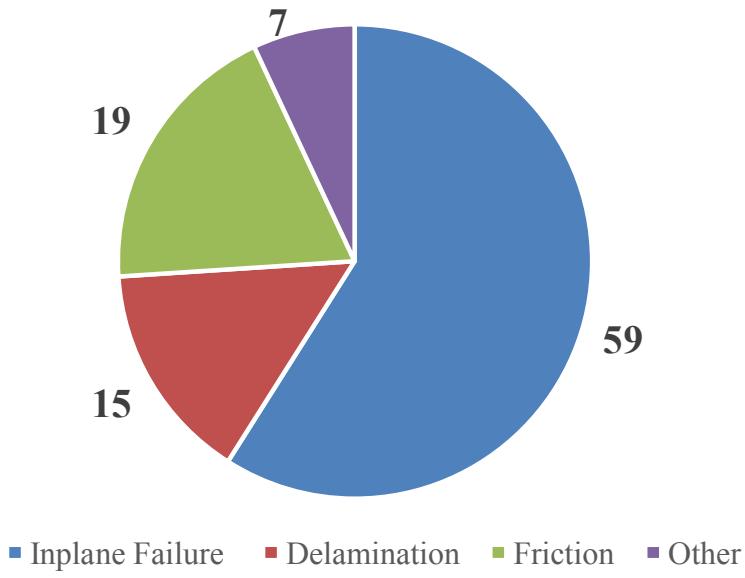

Figure 3.11. Repartition of energy (%) in the crushing process of flat plates (Created from the data presented by Israr et al. [19]).

Regarding the share of various mechanisms in energy distribution, it can be said that %15 of total energy is absorbed due to the delamination and this value decreases when the number of delaminating interfaces is reduced. The interlaminar properties should be increased to compensate energy for the reduced interfaces. The first response may be doubling the fracture toughness values (G); however, adjusting only G values will lead instability in numerical results since the cohesive zone length also change. In order to keep the cohesive zone length (formulized by Turon et al. as given in Equation 3.8.) same, interfacial strength values should also be increased by the square root of the increase in G value. Therefore, in numerical approach, the interfacial strength values are increased by %41 while fracture toughness values are doubled.

Besides delamination, as can be seen again from Figure 3.11, most of the energy is absorbed by the in-plane failure. Since the stacking sequence is kept the same, there will be no change in the energy absorbed by fiber and matrix failures. However, one should also consider the splaying mode, which is an important mode of failure especially in composite structures made of unidirectional plies stacked at various angles.

During the splaying of plies, bending [0/90] sub-laminate may absorb more energy than bending two individual 0 and 90° plies. Therefore, to balance the energy absorption, in-plane parameters should be reduced. To prove this idea, 3-point bending (3PB) test models are simulated for 0°, 45°, 90° plies as well as [0/90] and [0/45] sub-laminates as shown in Figure 3.12, which also shows the resultant load-displacement curves until failure.

The absorbed energy values are calculated from the area under the load-displacement curves and the results are given in Table 3.3. Same procedure is applied to the 45° ply and [0/45] sub-laminate and the energy results are demonstrated in Table 3.4.

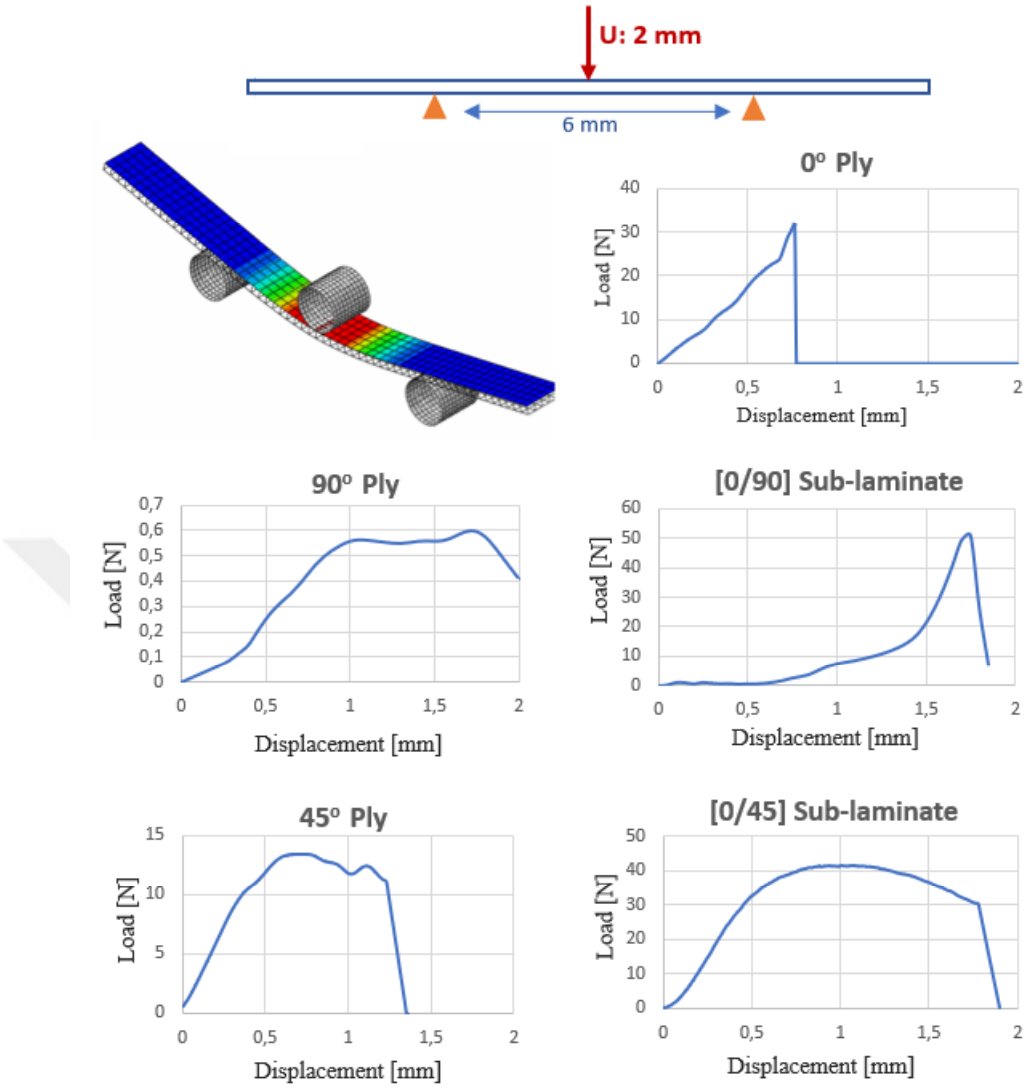

Figure 3.12. 3-point bending test model and simulated load-displacement results.

Table 3.3. Energy absorption of 0º, 90º plies and [0/90] sub-laminate.

	0º	**90º**	**0º + 90º**	**[0/90]**	**Required Reduction [%]**
Energy [mJ]	9.01	0.81	9.82	19.78	49.64

Table 3.4. Energy absorption of 0º, 45º plies and [0/45] sub-laminate.

	0º	**45º**	**0º + 45º**	**[0/45]**	**Required Reduction [%]**
Energy [mJ]	9.01	14.2	23.21	53.1	56.29

According to these results, the energy absorbed by [0/90] plate is approximately two times higher than the sum of energies absorbed by individual 0 and 90-degree plies. Therefore, to reach the accurate outcomes from the novel numerical approach, in-plane parameters are decreased by 50% since it is observed that [0/90] sub-laminates do not remain intact during crushing. According to the results given in Table 3.4, for the novel numerical model of $[0/45/0/-45]_s$ plate, in-plane parameters are decreased by 55%.

Despite parametric adjustments, in the numerical analysis applied in ABAQUS/Explicit, the imposed velocity, boundary conditions and element types are kept the same with the original model. With the new numerical approach, energy absorption capability of composite flat plates can be estimated accurately, and the computational time is decreased considerably. The results are examined in the following section.

3.3. Results and Discussion

3.3.1. Test Results

One of the purposes of this study is to understand failure mechanisms that creates crushing morphology and the load-displacement trend. Figure 3.13 presents the load-displacement curves of cross-ply $[0/90]_{2s}$ flat plates with 8 plies obtained from the quasi-static crush tests. Some snapshots of gradual crushing of one of the specimens is given in Figure 3.14.

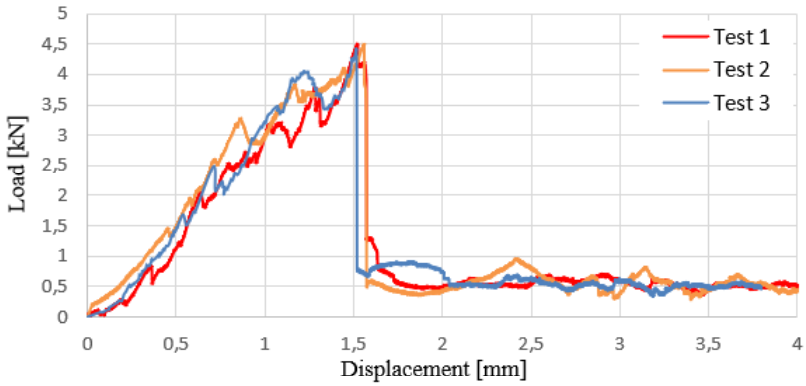

Figure 3.13. The load-displacement curve of the $[0/90]_{2s}$ flat specimen with 8 plies.

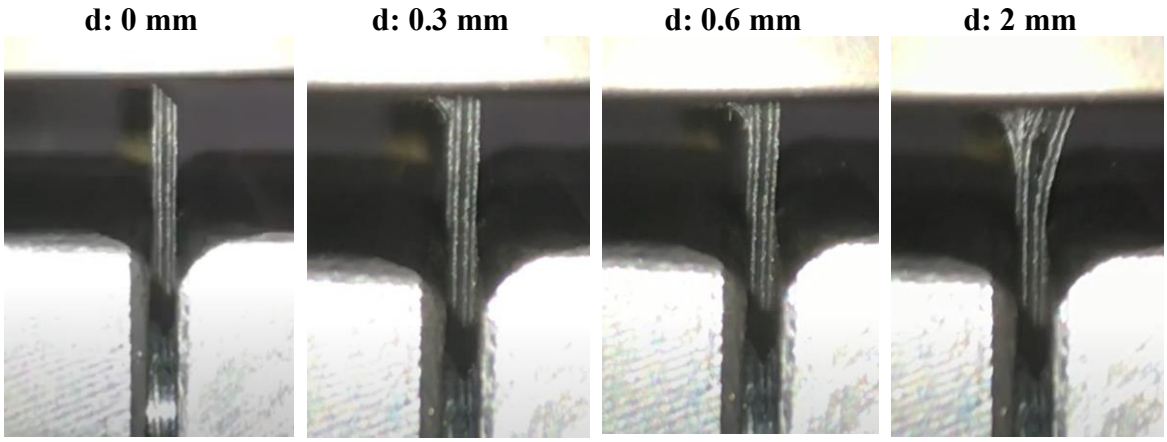

Figure 3.14. The crushing process of $[0/90]_{2s}$ flat plate specimen with 8 plies from Test 1.

According to the observations made from the crushing morphology, at the beginning of the crushing process of flat coupon plates, delamination starts at the interface between first and second plies due to the high stress levels at the tip of the chamfer. After that point, the first ply, subjected to axial load by moving rigid wall, starts to bend and that creates splaying mode. The length of the bent ply depends on the length of the interlaminar crack that occurs at the interface. Since the length of the interlaminar cracks is variable throughout the thickness, one can see different levels of splaying mode during the crash event. In a cross-ply specimen, generally 0-degree plies have higher tendency to bend; therefore, fiber tensile failures can be seen due to the bending mode.

After splaying of some plies, fragmentation occurs at the plies that do not bend or splay. The fragmentation mode is characterized by two types of failure. The first type is matrix cracks that occur in the 90-degree plies due to shear. Debris is formed by these accumulated fragments. The second type is fiber failure in the 0-degree plies, located in the center, due to micro-buckling of the fibers at the tip or fiber breakage as a result of a combination of compression and bending. Usually, the fragmentation mode starts first with 45-degree cracks in 90-degree plies. If the transverse force is high enough (causing larger cracks), splaying mode can be initiated in other 0-degree plies. If this is not the case, adjacent 0-degree plies are also subjected to local fragmentation.

After delamination has initiated at all seven interfaces, the load reaches its peak level and then stable zone starts after about 1.5 mm crush where the load fluctuates around a mean load and the main failure modes are micro-fragmentation and splaying. Cross ply specimens with 12 and 16 plies are also tested using the same experimental procedure and the load-displacement curves and failure mechanisms can be seen in Figures 3.15, 3.16, 3.17 and 3.18.

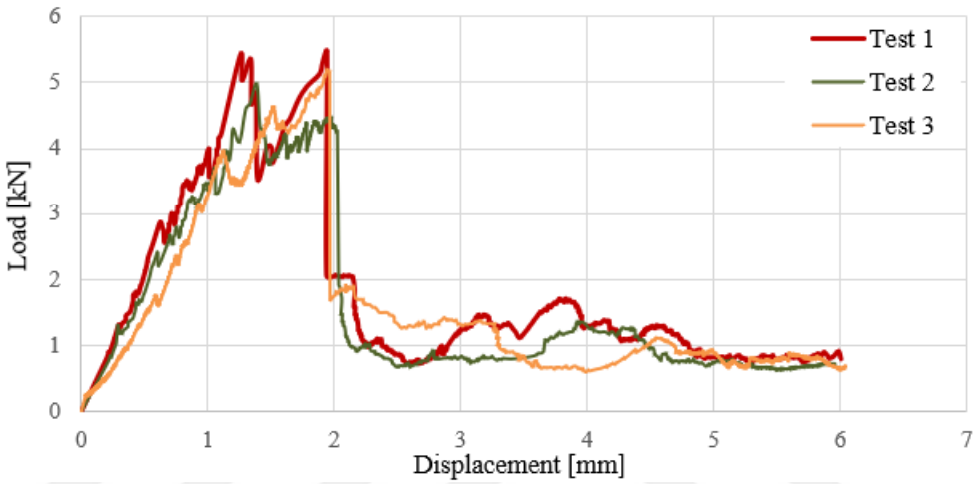

Figure 3.15. The load-displacement curve of $[0/90]_{3s}$ flat specimen with 12 plies

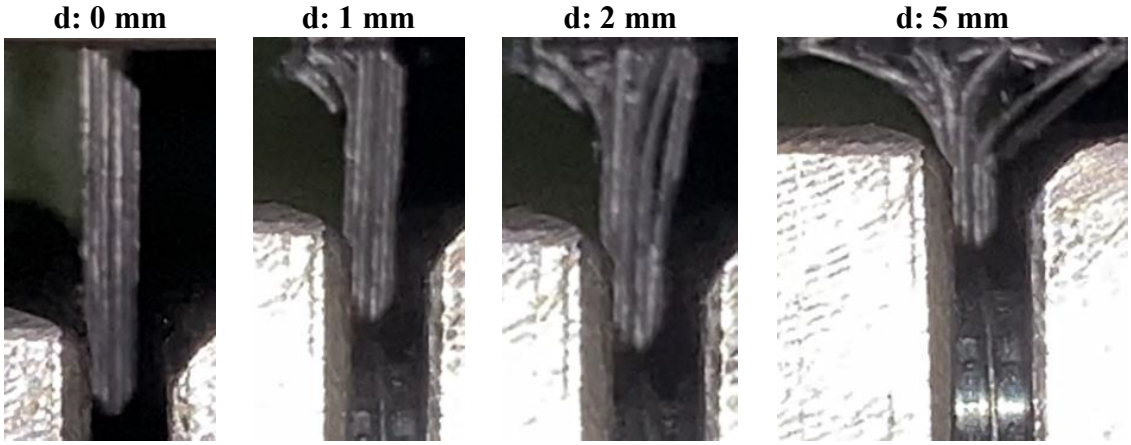

Figure 3.16. The crushing morphology of $[0/90]_{3s}$ flat specimen with 12 plies from Test 1.

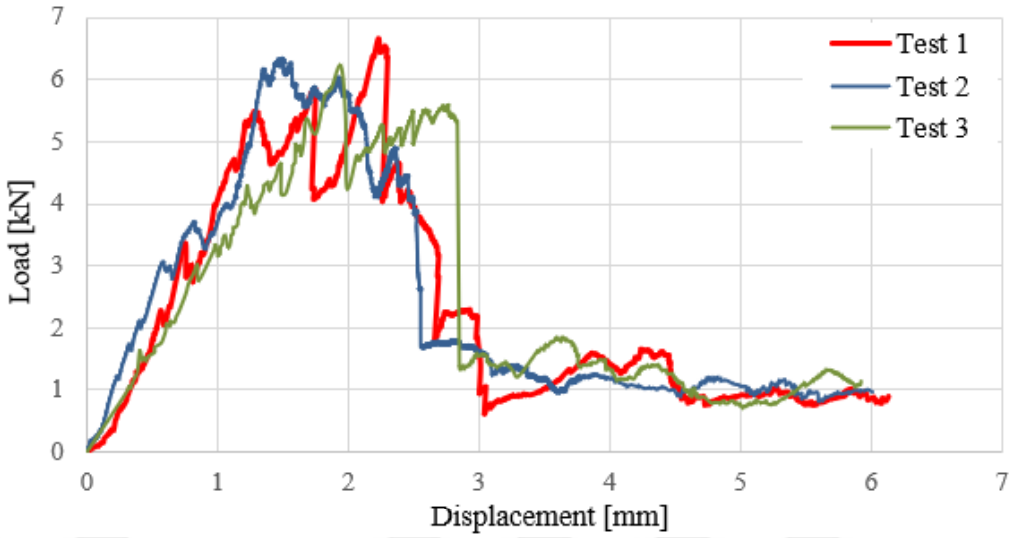

Figure 3.17. The load-displacement curve of $[0/90]_{4s}$ flat specimen with 16 plies.

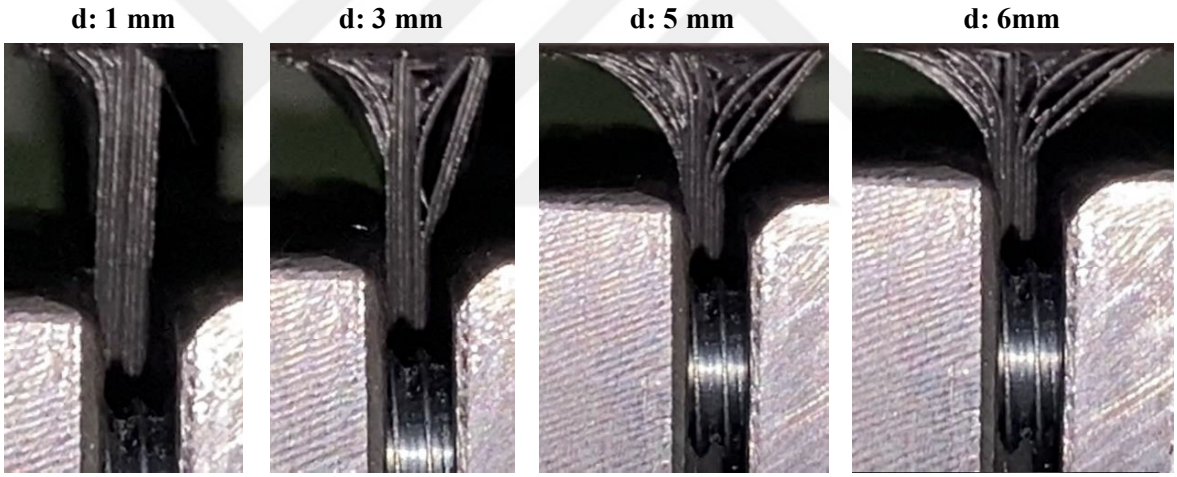

Figure 3.18. The crushing morphology of $[0/90]_{4s}$ flat specimen with 16 plies from Test 1.

Specific energy absorption (SEA) is calculated for all thicknesses and the results are compared in Table 3.5. For the specimens with different thicknesses, SEA values are quite close to each other. It can be deduced that thickness has no influence on SEA for flat plate specimens.

Table 3.5. The comparison of SEA values for different thicknesses.

# of Plies	Specimen No	SEA [J/g]	Average
8	#1	32,31	32,14
	#2	32,18	
	#3	31,94	
12	#1	32,22	32,19
	#2	31,94	
	#3	32,42	
16	#1	32,28	32,20
	#2	32,01	
	#3	32,32	

The load-displacement curves and the snapshot of $[0/45/0/-45]_s$ plate taken at the end of the test is demonstrated in Figure 3.19.

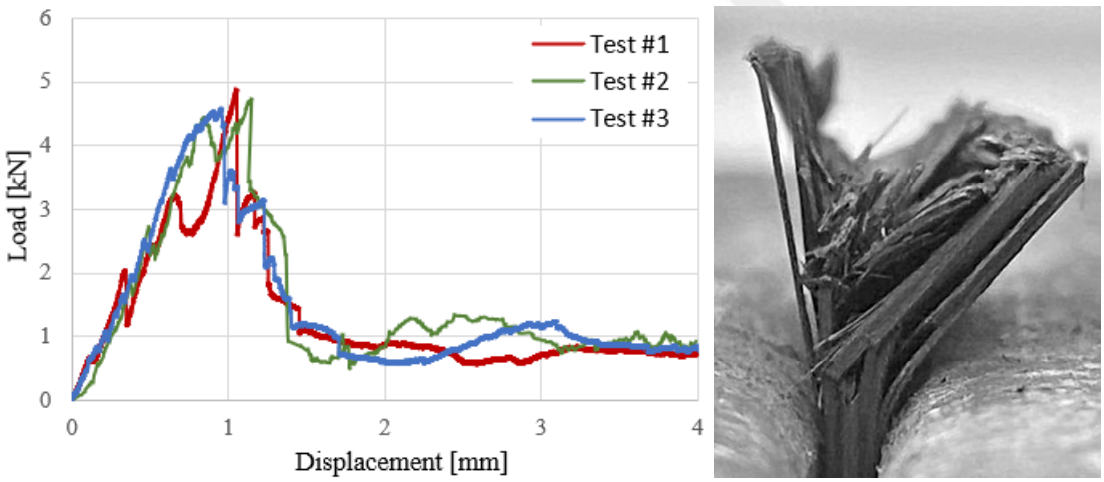

Figure 3.19. Experimental results of $[0/45/0/-45]_s$ flat specimens: load-displacement curve (left), crushed morphology (right).

For three $[0/45/0/-45]_s$ plates, the mean value of the load at the stabilized region is higher than the loads obtained from $[0/90]_{2s}$ plates which means that they can absorb more energy than cross ply specimens. The average SEA value of $[0/45/0/-45]_s$ plates is calculated from the load-displacement curves as 41,82 J/g. According to the observations made from the crushing morphology during the quasi-static compression tests, the reason behind that increase in the energy absorption capability can be explained with the increase in the number

of fragmentated fibers. When compared to 90-degree plies, where matrix cracks leading to splaying is the dominant mechanism, in 45-degree plies, more fiber breakage is observed which is the mode that absorbs highest energy among all in-plane failure modes.

3.3.2. Results of Numerical Analyses

The comparison between the load-displacement curves of the experimental and numerical studies is presented in Figure 3.20. In this figure, numerical results are obtained using the model with cohesive elements in every interface between each ply. Although there are some fluctuations in the load-displacement curve obtained by numerical study, the overall trend is similar to the experimental data and more importantly, the model can predict the amount of energy absorbed during the crushing process accurately (see Figure 3.21). Here the kink in the energy-displacement curve corresponds to the point where crush zone reaches to the end of the chamfer, after which the energy absorption is uniformly increases as crush zone proceeds.

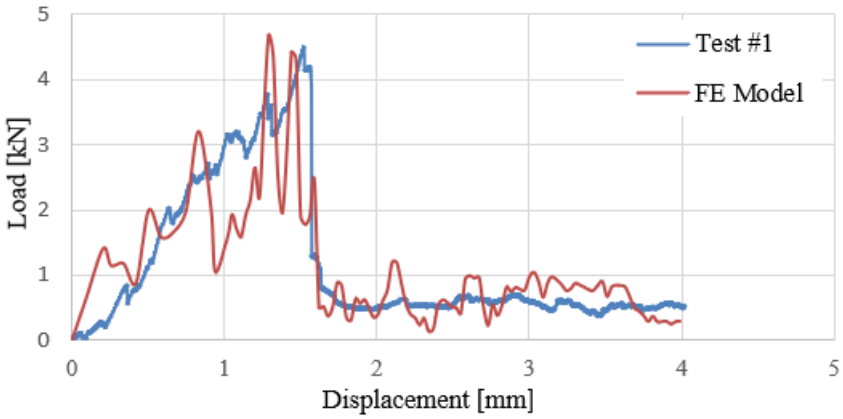

Figure 3.20. Comparison between the load–displacement curves of the experimental test and FE analysis for $[0/90]_{2s}$ flat plate specimen.

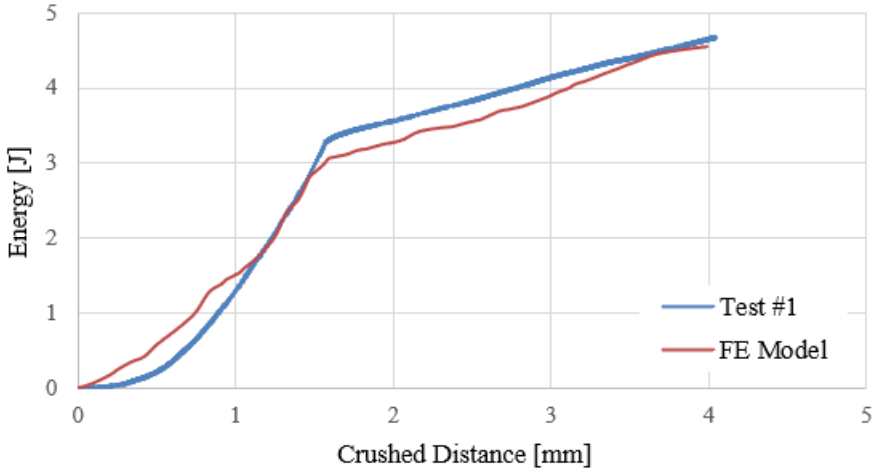

Figure 3.21. Comparison between absorbed energy values of $[0/90]_{2s}$ flat plate during the experimental test and FE analysis.

The model is also successful to demonstrate the failure mechanisms accurately when compared with the actual tests (see Figure 3.22). The numerical model can predict the specimen behavior consistently during the crushing process. In third row of the Figure 3.22, delamination growth is also presented step by step which is also consistent with the actual propagation. The in-plane damages occurring inside the flat plate specimen at the end of the crushing process are given in the Figure 3.23. Model shows the fiber failure in 0-degree plies while matrix failure is formed in 90-degree plies.

The results obtained from the novel numerical model applied to the 8-ply specimen are demonstrated in Figure 3.24. As can be seen from the figure, experimental data are compared with the results of two novel FE models (with and without parametric adjustments). It should be noted that, for a clear comparison, SAE filter with 180 Hz frequency cut-off is applied to the numerical results of the novel approach which reduces the numerical noise occurring due to the explicit analysis [95]. Without any parametric adjustments, FEA model with 3 interfaces shows no consistency with the test curve and the value of absorbed energy at the end of the crushing process is much higher than the test data as can be seen from Figure 3.25. After adjusting the parameters (increasing interlaminar properties and decreasing in-plane properties), a good agreement in terms of load–displacement curves and the energy values between the model and test is achieved.

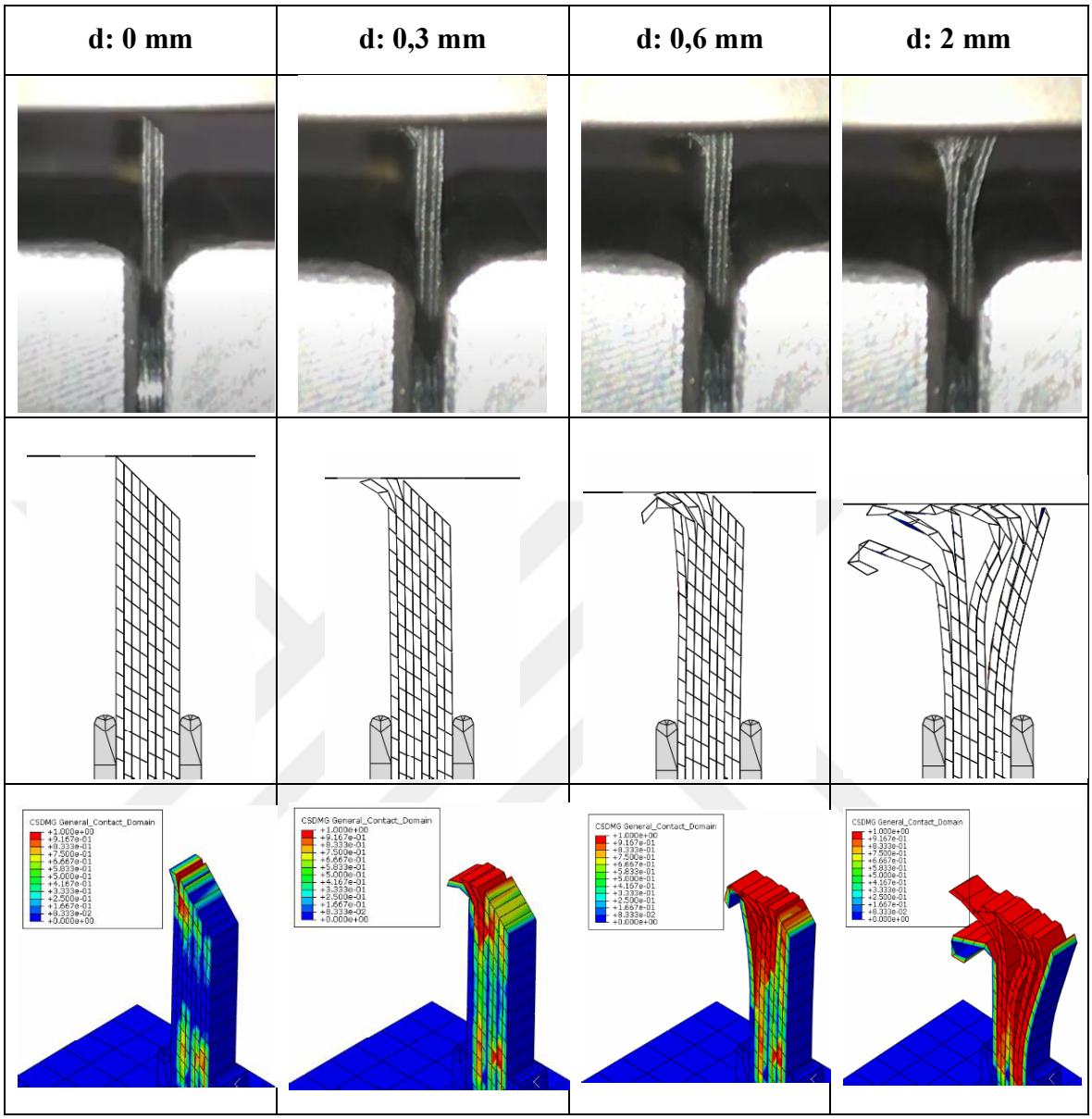

Figure 3.22. Comparison of experimental and numerical analysis of progressive damage of $[0/90]_{2s}$ plates: Test photos (top), Front view of propagation of crush (middle), isometric view of numerical model and delamination growth (bottom, colour code corresponds to interface damage due to delamination).

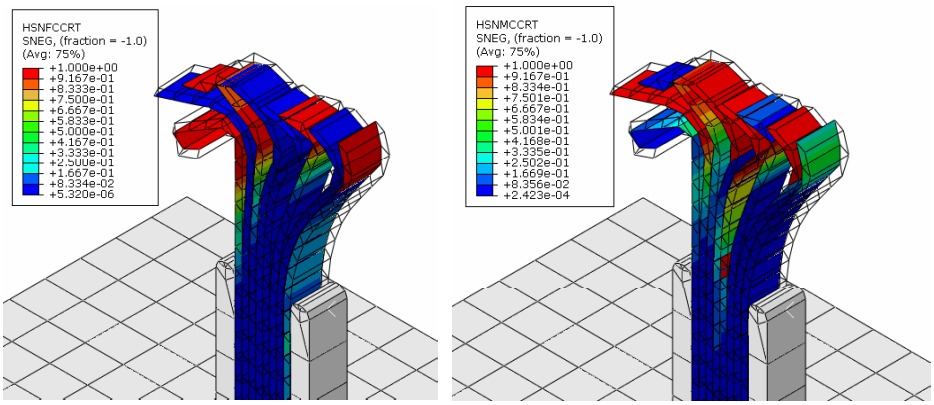

Figure 3.23. In-plane failures in $[0/90]_{2s}$ flat plate after 2 mm crash: Fiber failure (left), matrix failure (right).

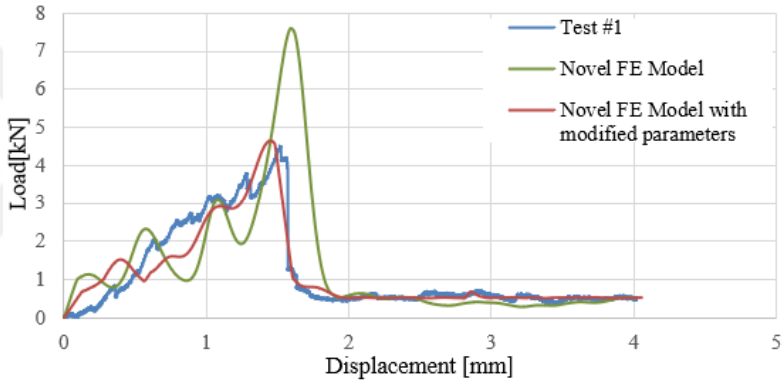

Figure 3.24. Load-displacement curves of the novel approach and comparison with the test data for $[0/90]_{2s}$ specimen.

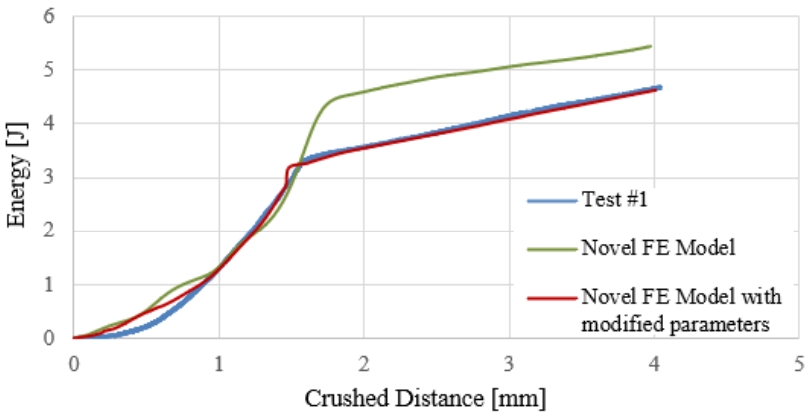

Figure 3.25. Energy results of the novel approach and comparison with the test data for $[0/90]_{2s}$ specimen.

To test the applicability of the novel numerical approach to thicker specimens, same process is applied for specimens with 12 and 16 plies. Same parametric adjustments are applied, and it can be said from the Figure 3.26, the numerical results for 12-ply specimen also show good agreement with the test data in terms of both load and energy trends. Figure 3.27 compares load-displacement and energy curves of 16-ply specimen obtained from numerical analyses with the experimental data. The overall trends of novel numerical approach can be accepted as consistent with conventional model and the test data.

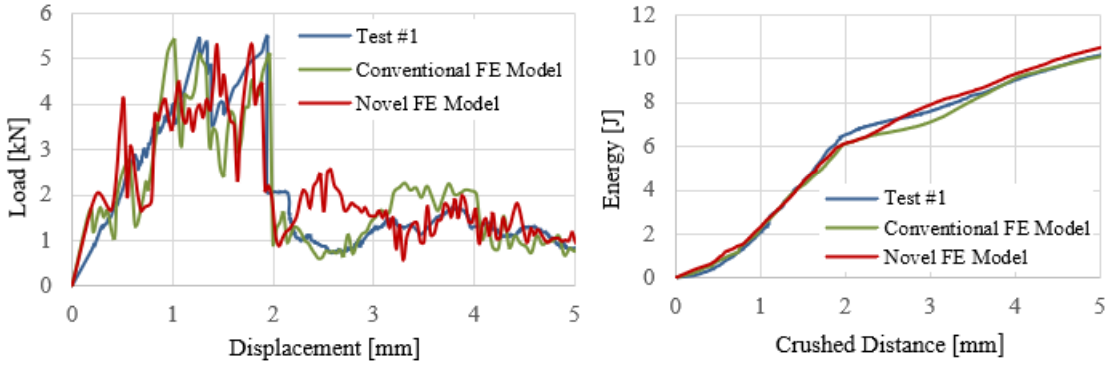

Figure 3.26. Comparison of 12-ply $[0/90]_{3s}$ plate model results with experimental tests in terms of load-displacement (left) and absorbed energy curves (right).

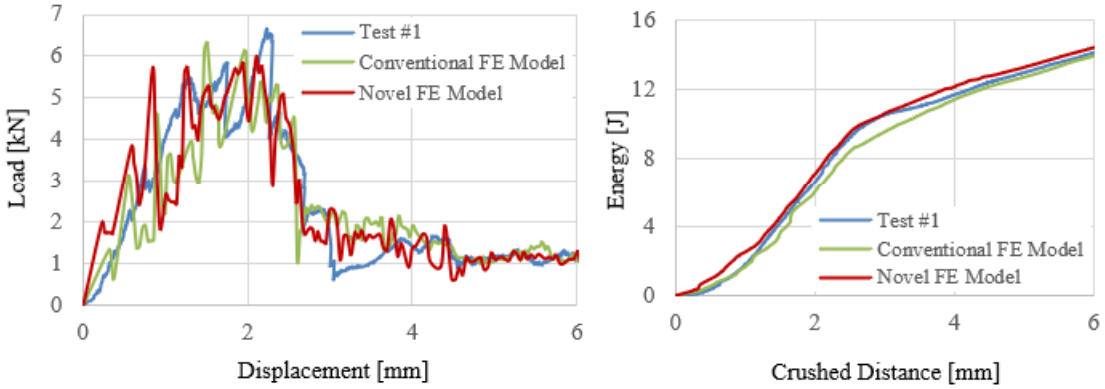

Figure 3.27. Comparison of 16-ply $[0/90]_{4s}$ plate model results with experimental tests in terms of load-displacement (left) and absorbed energy curves (right).

The novel numerical approach developed by creating sub-laminates of two plies stacked together and decreasing the number of elements leads lower computational costs for the composite plates having different ply numbers. Run times are decreased by more than 50% for 8, 12 and 16-ply cross-ply composite plate models. Table 3.6 demonstrates the reduction in computational time for each model.

Table 3.6. Computational times of FE models for different thicknesses.

# of Plies	**Run Time *(Conventional)* [min]**	**Run Time (*Novel*)) [min]**	**% Decrease**
8	32	14.5	54.7
12	48.5	23.5	51.5
16	77.5	37	52.3

The novel numerical approach is validated by applying the same procedure to the $[0/45/0/-45]_s$ flat coupon plates which is significant to understand the applicability of the model to composite plates having various stacking sequences. Figure 3.28 presents the comparison of load-displacement and energy curves of $[0/45/0/-45]_s$ specimen among experimental data, conventional FE model and novel FE model results. Results clearly show that, for the model with 3-interface, doubling interlaminar properties and decreasing in-plane parameters according to the bending energy results can estimate SEA values consistently in shorter amount of time when compared to conventional 7-interface FE models.

To summarize the experimental and numerical studies conducted for composite flat plates, it can be said that a comprehensive understanding of the failure mechanisms taking place during the crushing of flat plates is achieved. In a cross-ply specimen, while outer 0-degree plies have higher tendency to bend which creates splaying mode, fragmentation mode is observed mostly due to the matrix cracks in 90-degree plies. For $[0/45/0/-45]_s$ plate, more fiber breakages in 45-degree plies are observed and this increases the energy absorption capability. In the numerical analyses, a FE model for the crushing of composite flat plates is developed which is shown to be capable of estimating both failure mechanisms and the SEA performance. More importantly, with the novel modelling idea of creating sub-laminates, the objective of estimating energy absorption capabilities in shorter times is accomplished, and the computational time is decreased by more than 50% for flat plate models.

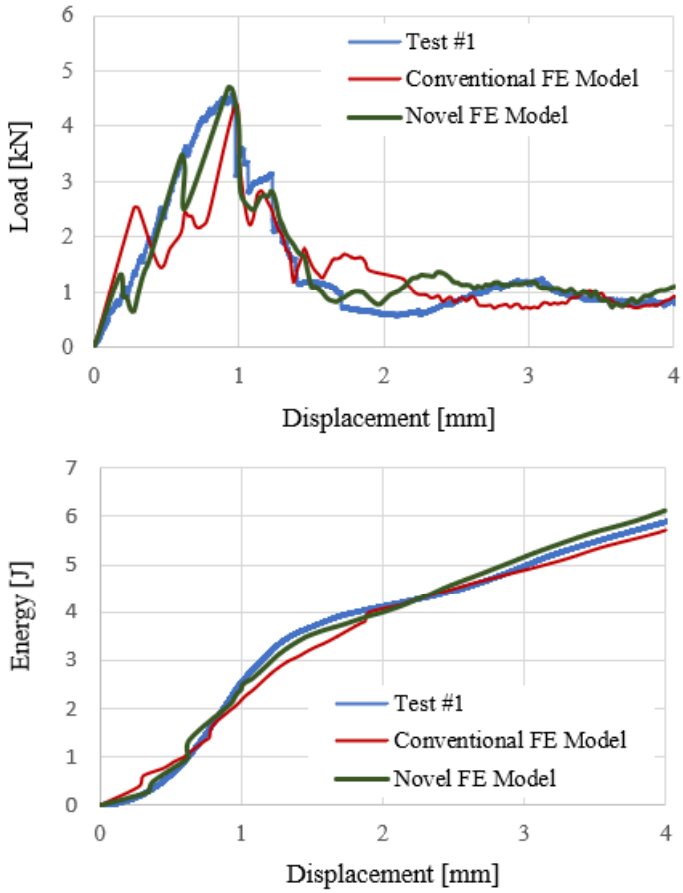

Figure 3.28. Comparison of $[0/45/0/-45]_s$ plate model results with experimental tests in terms of load-displacement (top) and absorbed energy curves (bottom).

4. FROM FLAT PLATES TO COMPLEX STRUCTURES: THE INFLUENCE OF GEOMETRY ON SEA

The expected failure modes during the crushing process of composite structures depend on many different factors. Geometry, among these factors, stands out as a significant one since the geometric design improvements of the structure with same amount of material can lead much improved SEA performances. Especially corrugated designs such as sinusoidal geometries are known to improve energy absorption capability to a considerable extent. However, there is a gap in literature in terms of conducting a systematic study to understand the influence of geometry on energy absorption capability, starting from simple coupon plates to complex structures. More importantly, the change of failure modes with different geometries and the relationship between these modes and the amount of absorbed energy still remains unclear. Therefore, this section aims to build on the work done in the previous chapter and will examine how failure modes and corresponding SEA performance change with different geometries.

In this chapter, the influence of geometry on the SEA of composite structures made of unidirectional AS4/8552 carbon/epoxy is investigated through various geometries such as semi-circle and sinusoidal specimens with different geometric characteristics. By keeping the cross-sectional area (hence the weight of the structure) constant, sinusoidal structures with different number of curvatures and diametral sizes are manufactured and tested. The resultant energy absorption capabilities and corresponding failure modes will be compared not only within themselves but also with flat coupon and semi-circle structures.

The experimental section also presents the manufacturing and testing of the flat and sinusoidal specimens made of woven fabric prepregs in order to understand how the relationship between the geometry and the absorbed energy varies when a different material system is used.

In addition to experimental tests, a Finite Element (FE) Model is developed in ABAQUS/Explicit for sinusoidal structures to estimate SEA numerically. For the accurate prediction of the crushing behavior and the failure mechanisms, the idea of artificial plug-initiator is incorporated into the FE Model. By utilizing the validated FE Model, further sinusoidal designs having more curvatures are simulated and the sinusoidal structure having the highest energy absorption capability is identified.

In previous chapter, a novel cost-effective numerical approach that leads reasonable run times was developed in which only one interface between every two plies is modelled instead of one interface between each ply of the structure by making necessary modifications to both interlaminar and intralaminar properties. In the last part of this chapter, novel modelling approach developed for flat plates is also applied to the crushing process of sinusoidal structures to show the validity of FE model for the complex geometries.

4.1. Experimental

4.1.1. Manufacturing and Testing of AS4/8552 Semi-Circle and Sinusoidal Structures

The semi-circle specimens are manufactured from Hexcel AS4/8552 carbon-epoxy UD prepregs by using same technique with the flat plates. 8 plies of prepregs are stacked on custom design mold with $[0/90]_{2s}$ cross-ply configuration. Manufacturing process is carried in the autoclave at Boğaziçi University according to the same Manufacturer's Recommended Cure Cycle, applying the same conditions in the manufacturing of flat plates as described in the previous chapter. The schematic of the cross-section is shown in Figure 4.1. The cross-section of the structure has a semi-circle with 45 mm radius and 8 mm straight lines positioned at each end-lips for extra stability. Manufactured specimens having 1.47 mm thickness are cut to 56 mm in length. 45° chamfer is also machined to one edge of specimens to avoid catastrophic failure and decrease the peak load.

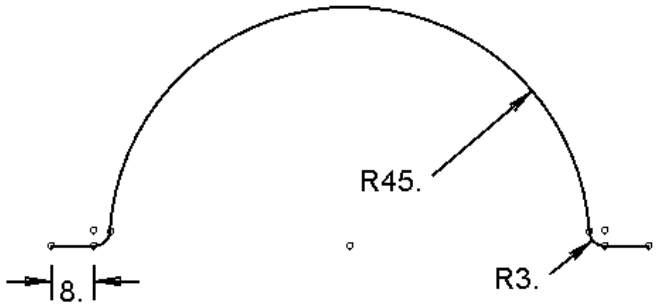

Figure 4.1. The schematic of the cross section of semi-circle specimen.

The design of sinusoidal structures consists of different number of repeating semi-circle curvatures. The idea is to keep the weight of material used constant while adding more semi-circle curvatures which leads the decrease in radii. So, sinusoidal structure with 3 curvatures (having 15 mm radii) and with 5 curvatures (having 9 mm radii) are designed and manufactured. Both structures have 8 mm straight lines positioned at each end-lips, same as semi-circle specimens. The schematic of cross sections of the sinusoidal structures with 3 and 5 curvatures can be seen in Figure 4.2.

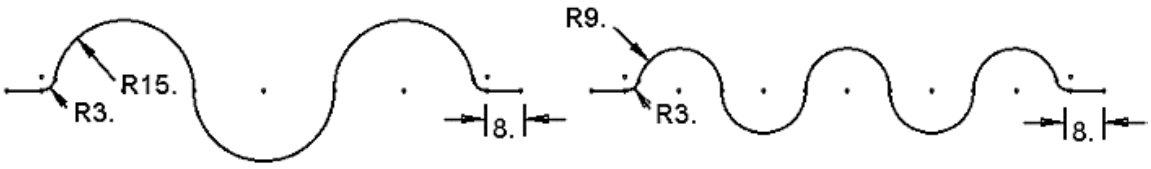

Figure 4.2. The schematic of the cross sections of sinusoidal structures with 3 curvatures (left), and 5 curvatures (right) (all dimensions are given in millimeters.).

The manufacturing process is again carried out in autoclave by stacking 8 plies of AS4/8552 carbon-epoxy UD prepregs on the custom design molds with $[0/90]_{2s}$ configuration. Figure 4.3 gives a snapshot taken during the manufacturing process demonstrating the vacuum bagged semi-circle and sinusoidal specimens on a custom designed mold before entering the autoclave.

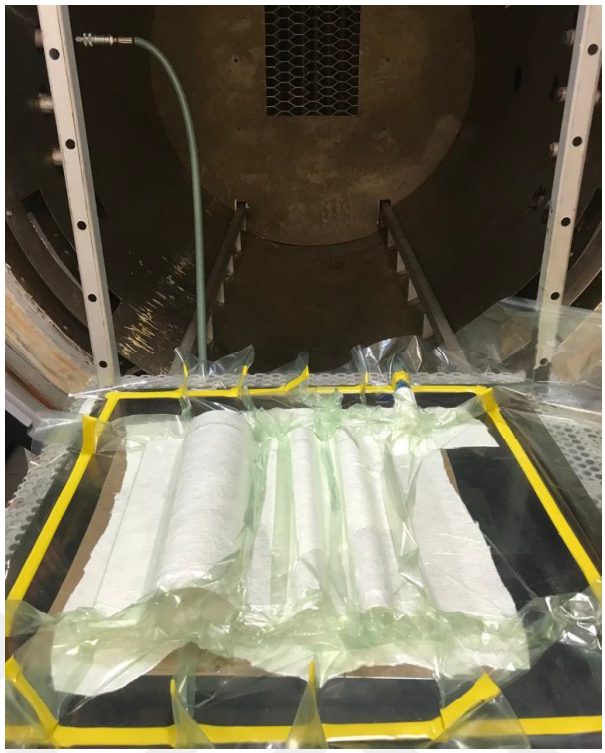

Figure 4.3. A snapshot taken during the manufacturing process.

Figure 4.4 shows final products of semi-circle and sinusoidal geometries with 3 and 5 curvatures.



(a) (b) (c)

Figure 4.4. Manufactured structures: semi-circle (a) and sinusoidal specimens with 3 (b), 5 curvatures (c).

Figure 4.5 demonstrates the test setup. Three specimens of each geometry are tested in the Zwick Z100 testing machine equipped with 100 kN load cell with crosshead speed of 0.5 mm/min. Tests are ended after the displacement of the crushing plate reaches 20 mm and the load-displacement curves are obtained.

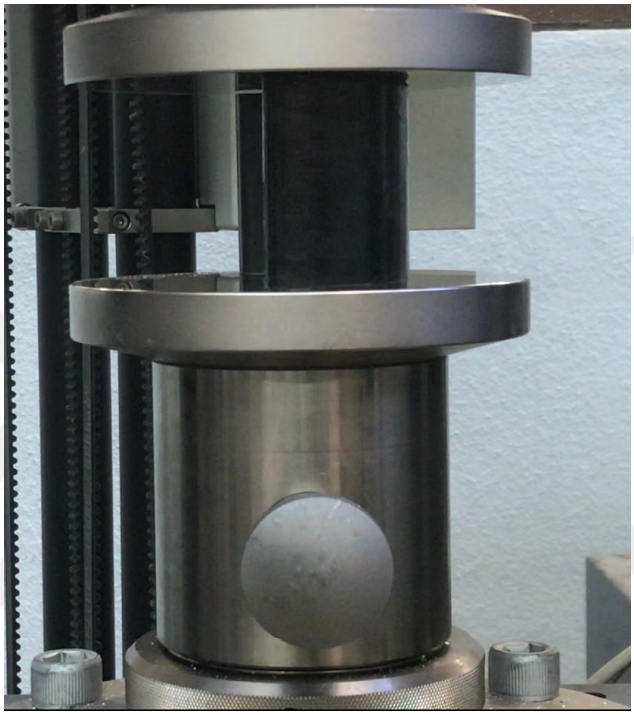

Figure 4.5. Test setup.

4.1.2. Manufacturing and Testing of Flat and Sinusoidal Structures Made of Woven Prepregs

This section presents the manufacturing and testing of composite flat and sinusoidal structures made of woven fabric prepregs, provided by KORDSA, with a product designation of KOM10T/PL200 and consists of a plain weave fabric of 200 gsm made of TORAY T300 3K carbon fiber tows and epoxy resin. The textile nature of woven fabric prepregs demonstrates different deformation and SEA characteristics when compared to the unidirectional composites [96].

This section aims to conduct a comparative analysis between the experimental results obtained from the crushing of structures made of woven fabric prepregs and the SEA results in previous sections (obtained from structures made of unidirectional prepregs) which will allow to examine how the relationship between the geometry and the absorbed energy varies when a different material system is preferred. For that purpose, the flat plate and sinusoidal specimens are manufactured from KOM10T/PL200 prepregs.

The Manufacturer Recommended Curing Cycle (MRCC) of the woven fabric prepreg can be seen in Figure 4.6 [97]. According to the presented curing cycle, specimens are cured at 130 °C for 100 minutes in the autoclave in Composites Lab at Boğaziçi University.

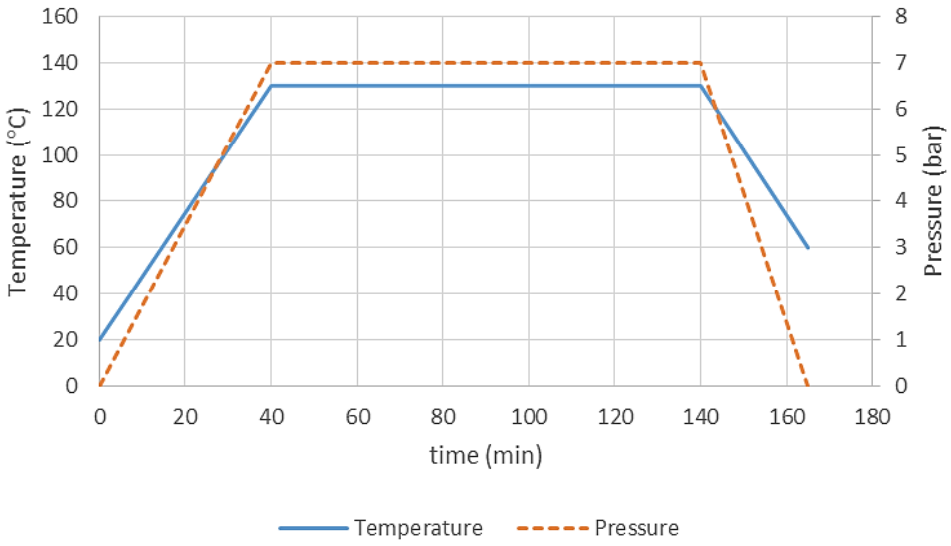

Figure 4.6. MRCC for KOM10T/PL200 woven prepregs [97].

The 300 mm x 300 mm plates manufactured by stacking 8 plies of prepregs on a flat mold are then cut by a diamond disk cutter into final test coupons. Final specimens have 20 mm width, 56 mm length and 1.6 mm thickness. The upper edge of the coupon is again 45° chamfered to prevent catastrophic damage as applied in unidirectional flat plates. The supporting fixture with 50 mm length is used to avoid buckling. The specimen with chamfered edge and the close-up photo of the material are presented in Figure 4.7.

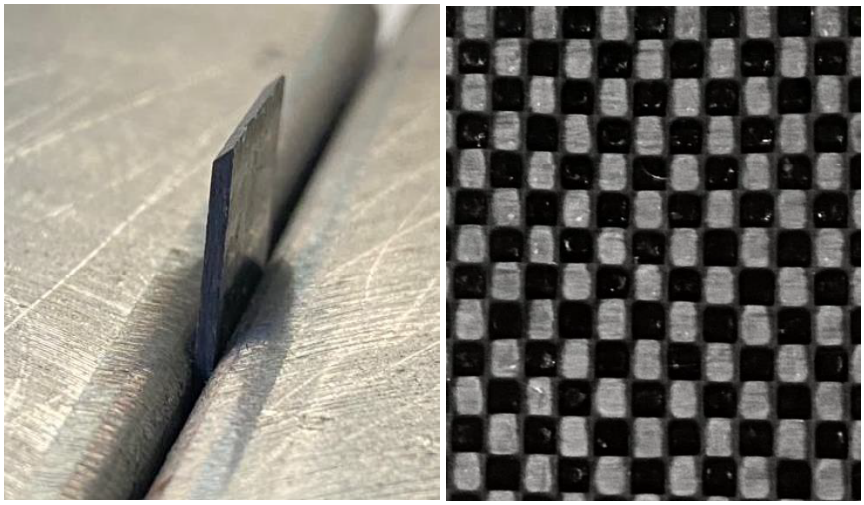

Figure 4.7. The flat specimen (left) and a close-up photo of the woven material (right).

Sinusoidal specimens having 3 and 5 curvatures are manufactured by stacking 6 plies of woven prepregs on the same molds used previously for structures made of unidirectional prepregs (see Figure 4.2 for the dimensions). Figure 4.8 demonstrates the manufactured woven fabric sinusoidal structures. Before proceeding to the testing phase, the specimens were cut to 56 mm in length and the top edges were chamfered at 45° as applied to unidirectional specimens. Then, three specimens of each geometry are tested in the Zwick Z100 testing machine with quasi-static speed of 0.5 mm/min.

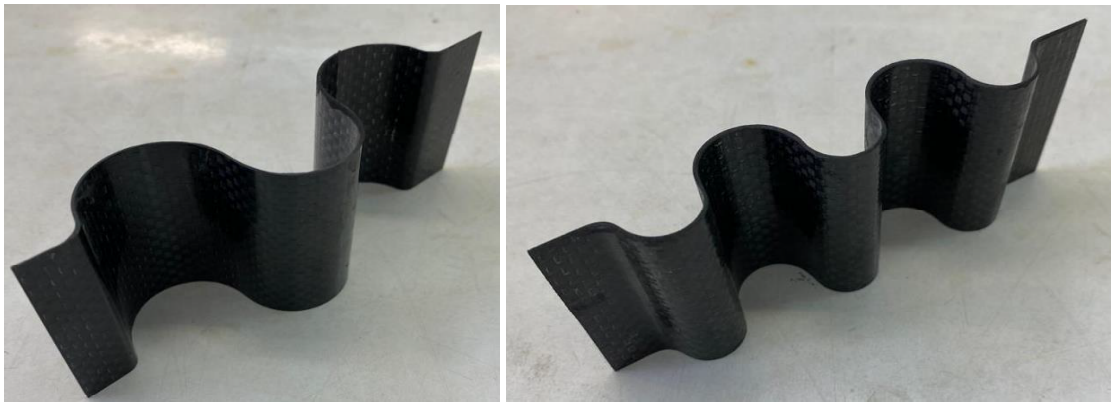

Figure 4.8. Manufactured sinusoidal specimens with 3 (left) and 5 curvatures (right).

4.2. Numerical

4.2.1. Conventional FE Model with Artificial Plug Initiator

The FE model for the progressive damage of AS4/8552 carbon fiber/epoxy sinusoidal structures with 3 and 5 curvatures are developed in Abaqus/Explicit considering both intralaminar (in-plane) and interlaminar (delamination) damage mechanisms. Half of the geometry is modelled by applying symmetry conditions. Each of the eight plies were individually extruded and meshed with 1 mm continuum shell elements (SC8R). Continuum shell elements in ABAQUS have the geometry of a three-dimensional solid element but their kinematic and constitutive behavior are similar to those of conventional shell elements. Boundary conditions are applied to be coherent with experimental procedure. Abaqus/CAE model can be seen from Figure 4.9.

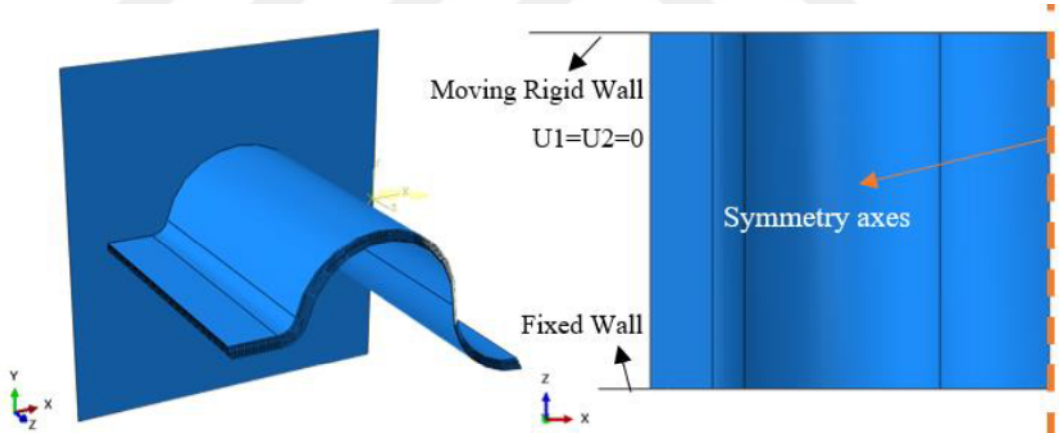

Figure 4.9. Abaqus/CAE half model of the sinusoidal structure with 3 curvatures: isometric view (left), front view (right).

As applied in the numerical analysis of AS4/8552 flat plates, the in-plane response of the individually extruded plies is modelled according to the Hashin Damage Criteria [49] and the mixed-mode delamination containing opening and shearing modes are applied to the interaction surfaces between unidirectional plies according to the Cohesive Zone Method (CZM).

The velocity of rigid upper wall is defined as 200 mm/s. Higher value of velocity than quasi-static test speed is utilized in the simulation in order to reduce step time which leads low computational cost. Since dynamic effects become important when the velocity is higher than 500 mm/s, this amount of artificial increase has no significant influence on simulation results [44]. The friction coefficient is taken to be 0.3.

One of the purposes of this study is to correlate the crushing behavior of the structures in the numerical analysis to the observed, actual modes. As will be elaborated in results section, although the numerical results show good agreement with the experimental data in terms of load-displacement curves, there are some mismatches occurring between observed failure modes and simulated crushing morphology. At that point, the idea of using artificial plug-initiator in the finite element model is proposed to initiate delamination properly and create a V-shape area to simulate the debris wedge formation during testing. Various geometries are designed and implemented in FE Model and Figure 4.10 demonstrates the final shape of the artificial plug-initiator giving most accurate results. The different attempts made for plug-initiator design and their influences on numerical results are presented in results section.

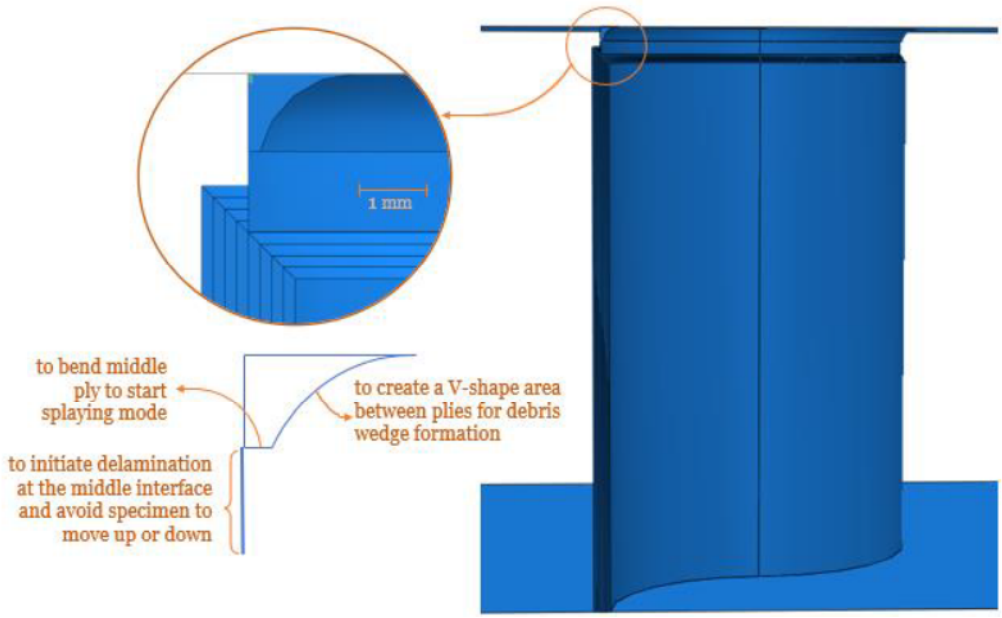

Figure 4.10. The finalized version of artificial plug-initiator design with the position in assembly.

In addition to sinusoidal structures having 3 and 5 semi-circle curvatures, for a deeper understanding of the influence of geometry on SEA, the crushing of sinusoidal structure with 7 curvatures is required to be investigated. This part of the study is carried out with numerical analysis only for two main purposes: to develop a FE Model which can predict the energy absorption capability of complex structures with accurate crushing behavior and to avoid extra manufacturing cost for tooling of structures with 7 curvatures. Before that stage, FE Model should be validated by using sinusoidal structure with 3 and 5 curvatures for which experimental data has already been obtained.

The validated FE model in Abaqus/Explicit is then applied for AS4/8552 carbon fiber/epoxy sinusoidal structures with 7 curvatures by again modelling half of the geometry to benefit from the symmetry conditions. Since the amount of material is desired to be same as previous geometries, the radius of repeating semi-circle segments is determined to be 6.43 mm. The schematic of the cross section and the Abaqus/CAE half model is presented in Figure 4.11. The simulation of 10 mm crush takes 244 minutes of run time on a 16-core workstation.

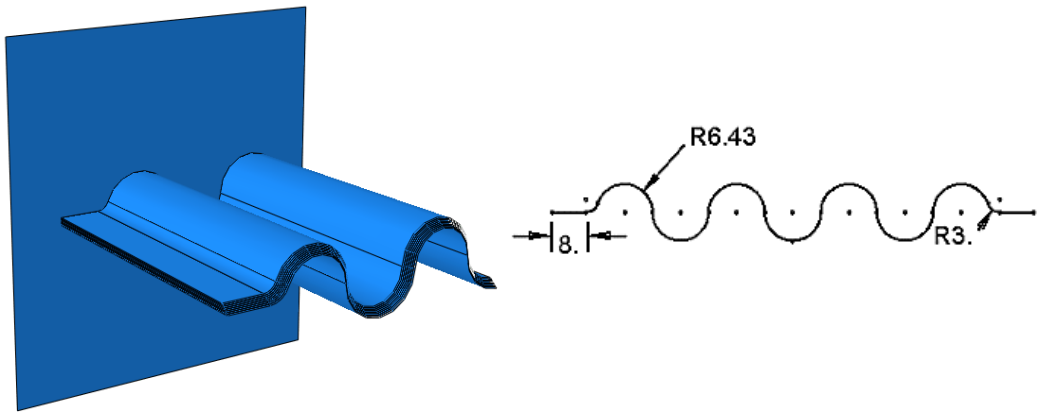

Figure 4.11. Abaqus/CAE half model (right) and the schematic of the mid-plane of sinusoidal structures with 7 curvatures (left) (all dimensions are given in millimeters).

4.2.2. Novel Modelling Approach Applied to AS4/8552 Sinusoidal Structure

In the previous chapter, a novel modelling approach that leads reasonable run times was developed and validated for flat plates. The modelling idea for the specimen with 8 plies is to extrude four [0/90] sub-laminates with one element through the thickness instead of eight individual plies and thus reduce the number of interfaces from 7 to 3. In the process of developing the approach, it was found that consistent results from the novel approach could only be obtained by making certain changes to the parameters: halving the in-plane parameters and doubling the fracture toughness while increasing the interfacial strength by %41. In this section, same approach is applied to the sinusoidal structure to see if it also works for a complex geometry. Accomplishing this attempt is significant to get faster results in such complex models for which computational cost is a serious issue.

The novel FE model in Abaqus/Explicit is applied for AS4/8552 cross-ply sinusoidal structures with 3 curvatures by again modelling half of the geometry with the plug initiator proposed in the previous section (see Figure 4.12). The imposed velocity, boundary conditions and element types are kept the same with the conventional model. The results of numerical studies are examined in the following section.

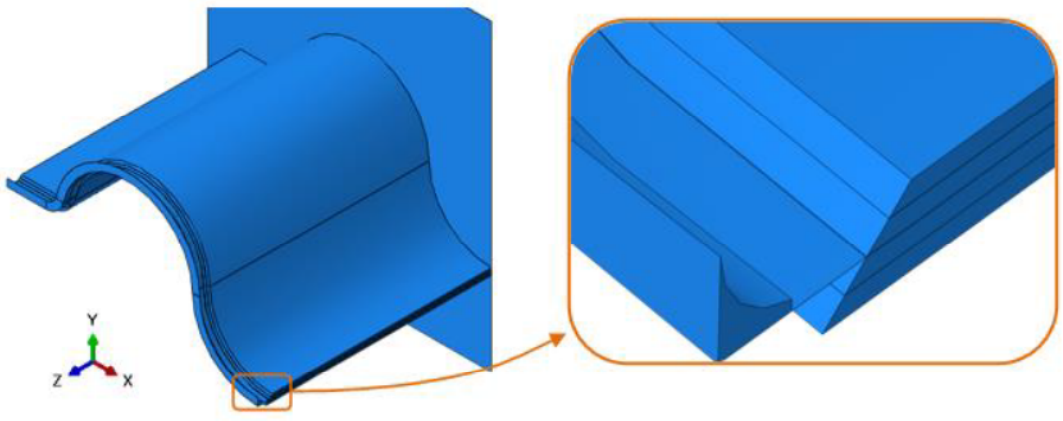

Figure 4.12. Abaqus/CAE novel FE model of $[0/90]_{2s}$ sinusoidal structures with 3 curvatures.

4.3. Results and Discussion

4.3.1. Test Results of Semi-circle and Sinusoidal Structures Made of UD Prepregs

The load-displacement curves of three semi-circle specimens made of UD prepregs tested under quasi-static compression and the crushed state of the first specimen are given in Figures 4.13 and 4.14.

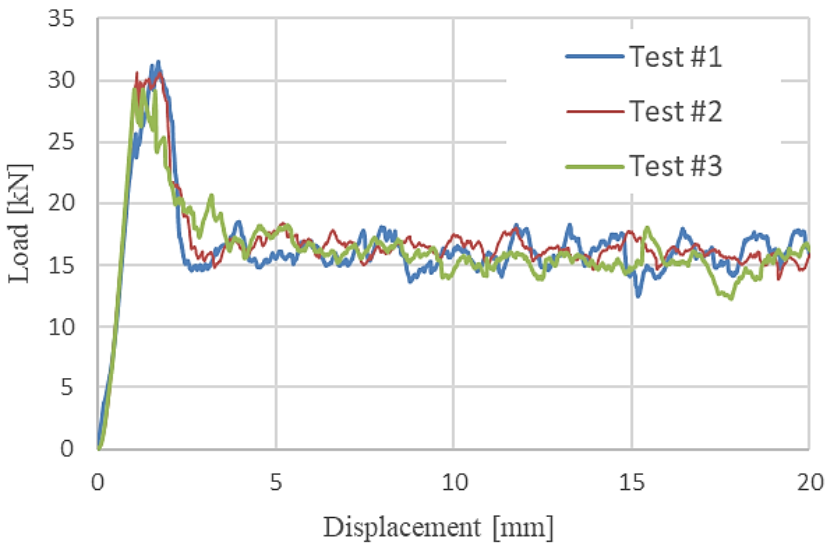

Figure 4.13. The load-displacement curves of the semi-circle specimens made of UD prepregs.

The SEA value for each specimen is calculated from the division of the area under the curve to the crushed weight and the average of the results is evaluated as 48.09 J/g (see Table 4.1.). The reason behind the increase in energy absorption capability by approximately 50% when compared to flat specimens can be explained by the change of failure mechanisms. During the crushing process, in addition to the splaying of 0-degree plies, vertical ruptures occurred which are characterized by long matrix cracks. Moreover, the level of fragmentation increased in the plies located near the center which automatically leads higher amount of energy absorption.



Figure 4.14. The crushed shape of the semi-circle specimen made of UD prepregs at the end of the test.

Table 4.1. The SEA values of semi-circle specimens made of UD prepregs.

Specimen No	**SEA [J/g]**	**Average**
#1	48.22	48.09
#2	48.94	
#3	47.12	

The deformed shapes of sinusoidal structures having 3 and 5 curvatures are given in Figure 4.15. According to the observations made during the tests, it can be said that the reflection points in the sinusoidal structure, which connect one of the repeating semi-circle segments to another, create obstacles that makes the splaying of the plies more difficult. Therefore, more micro-buckling occurred in 0-degree plies resulting in fiber breakage and more matrix cracks are initiated in the 90-degree plies located in the center. Moreover, for sinusoidal structures having 3 curvatures, the number of vertical ruptures occurring at the outer plies increase when compared to semi-circle specimens. This number becomes much higher for sinusoidal structure having 5 curvatures. These observations lead to the conclusion that sinusoidal structures have better performance in terms of energy absorption. The load displacement curves (see Figure 4.16), and the SEA results evaluated from these curves (see Table 4.2) confirm this conclusion. Sinusoidal structures with 5 curvatures absorb more energy than the others.



Figure 4.15. The deformed shapes of sinusoidal specimens made of UD prepregs with 3 curvatures (left), and 5 curvatures (right).

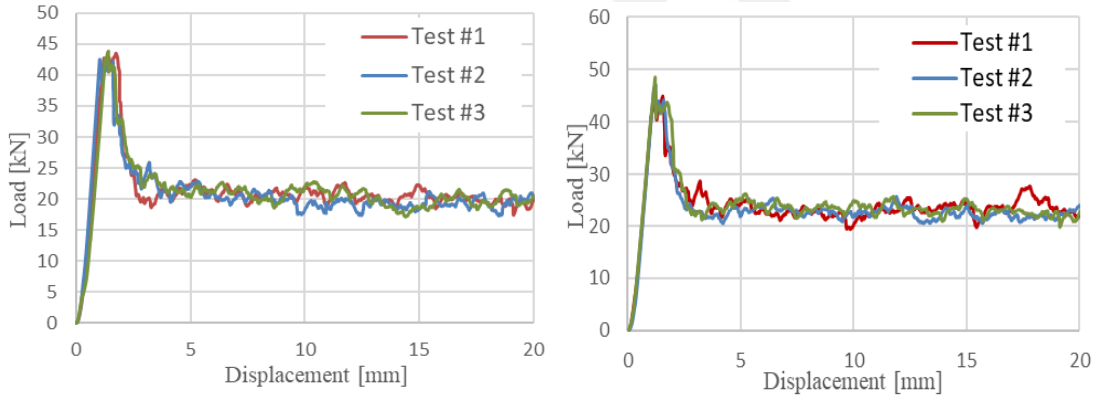

Figure 4.16. The Load-displacement curves of sinusoidal specimens made of UD prepregs with 3 (left), and 5 curvatures (right).

Table 4.2. The SEA values of sinusoidal specimens made of UD prepregs.

# of Curvatures	Specimen No	SEA [J/g]	Average
3	#1	62.71	62.64
	#2	62.18	
	#3	63.03	
5	#1	69.01	68.73
	#2	68.24	
	#3	68.94	

4.3.2. Test Results of Sinusoidal Structures Made of WF Prepregs

The purpose of conducting the quasi-static crush tests for specimens made of woven fabric (WF) prepregs is to understand the failure mechanisms occurring during the process which led to a different load-displacement trend and SEA performance than unidirectional specimens. Figure 4.17 shows the load-displacement curve results of flat plates specimens made of WF prepregs and the crushed morphology of one of the specimens.

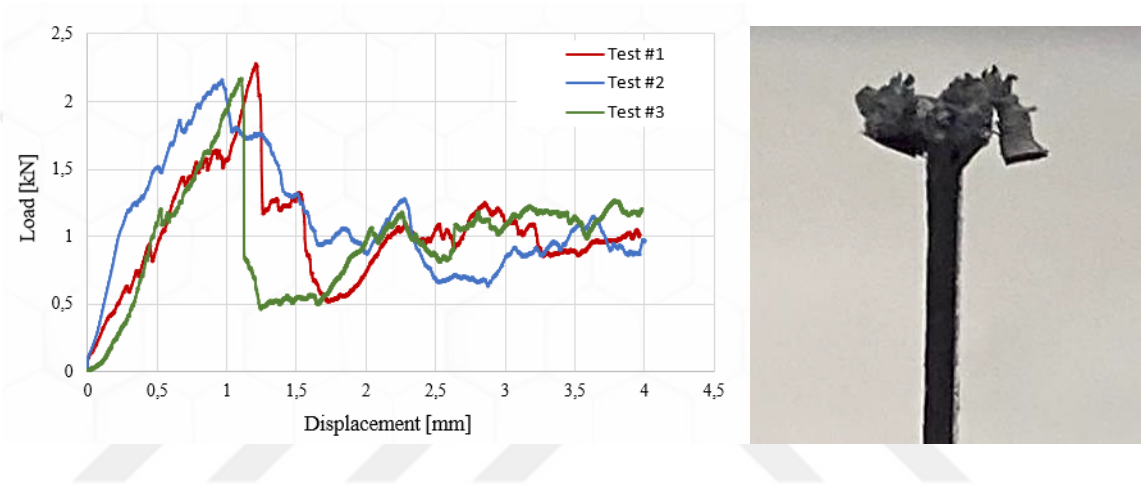

Figure 4.17. Experimental results of flat specimens made of WF prepregs: load-displacement curve (left), crushed morphology (right).

Table 4.3 demonstrates the SEA results of flat specimens made of WF prepregs evaluated by dividing the area under load-displacement curves by the crushed specimen mass. According to the table, it can be said that woven fabric composites have higher energy absorption capability than the unidirectional composites. This outcome should be explained and evaluated in parallel with the observations made from the crushing morphology.

At the beginning of the process of specimens made of WF prepregs, after the first delamination occurred at the interface between first and second plies, both matrix cracks and fiber fractures begin to occur directly in the first ply, after a small amount of bending. The fragmentation mode characterized by matrix cracks and fiber failure continue to be seen in the rest of the plies and the debris is formed by these accumulated fragments. The textile nature of woven fabric prepregs obtained by interlocking yarns is the reason why more

fragmentation mode is seen throughout the process rather than splaying mode which is dominant in specimens made of WF prepregs. Since more fragmentation means higher levels of energy absorption, flat specimens made of WF prepregs exhibit greater SEA performance than the cross-ply specimens made of UD prepregs in which 0-degree plies inside the laminate tend to bend; therefore, the splaying mode becomes dominant to a certain extent resulting lower energy absorption compared to specimens made of WF prepregs .

Table 4.3. The SEA values of flat specimens made of WF prepregs.

Specimen No	SEA [J/g]	Average
#1	51.75	50.42
#2	51.05	
#3	48.46	

The load-displacement curves of sinusoidal specimens made of WF prepregs with 3 and 5 curvatures are given in Figures 4.18 and 4.19. According to experimental data taken during the quasi-static tests, the load first reaches its peak level for all specimens and then stable zone starts where the load fluctuates around a mean load. While the mean load is evaluated as 28,5 kN for sinusoidal structure with 3 curvatures, this value increases to 31,2 kN for sinusoidal structure with 5 curvatures.

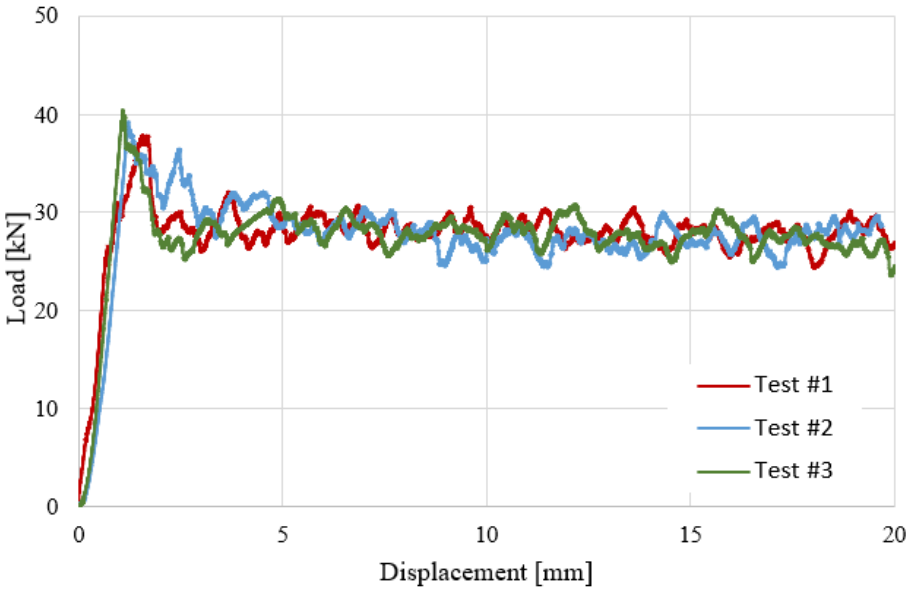

Figure 4.18. The load-displacement curves of specimens made of WF prepregs having 3 curvatures.

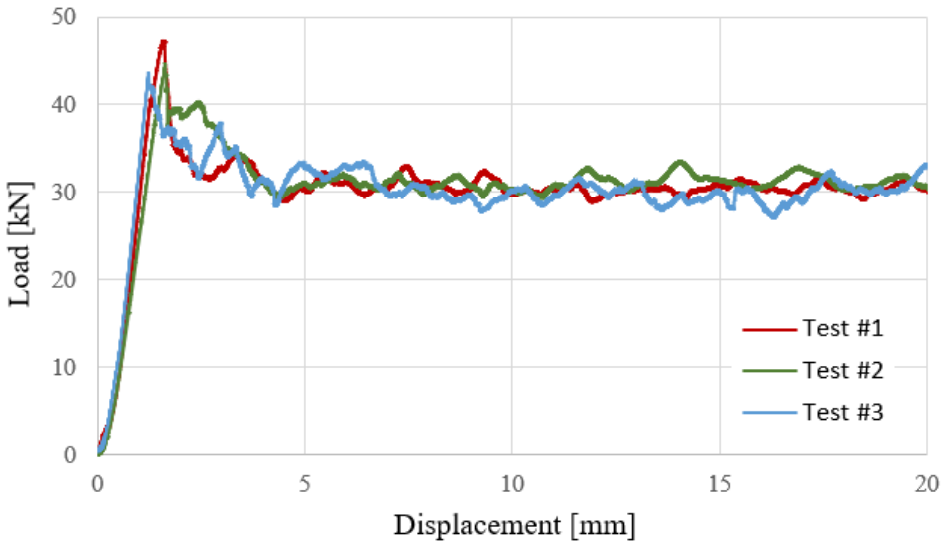

Figure 4.19. The load-displacement curves of specimens made of WF prepregs having 5 curvatures.

The deformed shapes of sinusoidal structures made of WF prepregs having 3 and 5 curvatures are given in Figure 4.20. According to the observations made during the tests, it can be said that the connection points between one of the repeating semi-circle segments and another create obstacles and prevent plies from splaying. Therefore, more vertical fiber ruptures and so more fragmentation mode occurs. These observations lead to the conclusion that sinusoidal structures have better performance in terms of energy absorption. Moreover, due to having more inflection points, the mean load and the resultant energy absorption performance of sinusoidal structure having 5 curvatures is higher than the others. The SEA results evaluated for these specimens also confirm this conclusion as can be seen from Table 4.4. When it comes to the sinusoidal structure with 5 curvatures, SEA value increases by 50% compared to the flat plate and 38% compared to the sinusoidal structure with 3 curvatures.

Table 4.5 gives the overall comparison of SEA performances between structures made of unidirectional and woven prepregs including flat and sinusoidal geometries. In general, considering how SEA is affected by the change in geometry, it can be said that for both material systems there is a similar relationship that SEA increases when moving from flat plate to sinusoidal geometry. Moreover, even though a different material system is selected, the sinusoidal structure having 5 curvatures exhibits the highest performance.

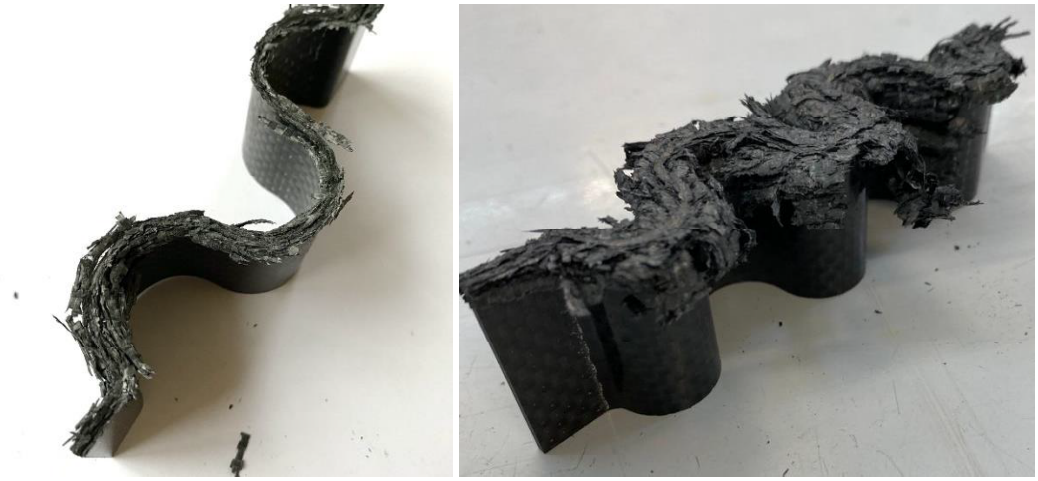

Figure 4.20. The deformed shapes of sinusoidal specimens made of WF prepregs.

Table 4.4. The SEA values of sinusoidal specimens made of WF prepregs.

Geometry	Specimen No	SEA [J/g]	Average
Sinusoidal (3 Curvatures)	#1	69.84	69.33
	#2	68.94	
	#3	69.20	
Sinusoidal (5 Curvatures)	#1	76.01	76.37
	#2	77.40	
	#3	75.72	

Looking at the details, the difference in the SEA value between flat and sinusoidal geometry is not as large in the woven fabric specimens as in the UD ones. The reason for this can be explained with that there is a significant change in the dominant mode in structures made of UD prepregs when moving from flat to sinusoidal geometries (from splaying to fragmentation), while in specimens made of WF prepregs, the fragmentation mode is already dominant in both geometries. When the performances of two sinusoidal geometries is evaluated for both materials, it is interesting to identify that the amounts of SEA increase from 3 to 5 curvatures are same for both materials which is approximately 10%.

Table 4.5. The SEA comparison between structures unidirectional (UD) and woven fabric (WF) prepregs.

	UD	WF
Flat Plate	32.14 J/g	50.24 J/g
Sinusoidal (3 Curvatures)	62.64 J/g	69.33 J/g
Sinusoidal (5 Curvatures)	68.72 J/g	76.37 J/g

4.3.3. Conventional Numerical Results

The FE model was developed for the progressive damage of sinusoidal structures made of unidirectional carbon fiber/epoxy prepreg with 3 curvatures and the comparison between the load-displacement and energy curves of the experimental and numerical studies is presented in Figure 4.21. Although there are some fluctuations in the load-displacement curve obtained by numerical study, the overall trend is similar to the experimental data and more importantly, the model can predict the amount of energy absorbed during the crushing process accurately. Here the slight kink in the energy-displacement curve corresponds to the point where crush zone reaches to the end of the chamfer after which the energy absorption is uniformly increases as the crush zone proceeds.

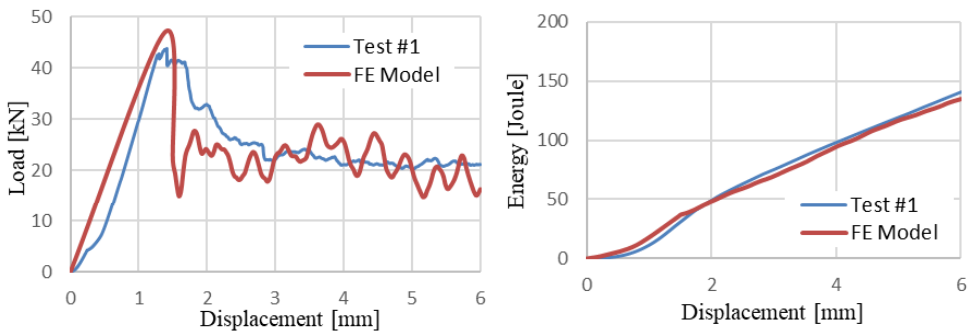

Figure 4.21. Comparison of FE model of sinusoidal specimen having 3 curvatures with experimental tests: load-displacement curves (left), and energy curves (right).

The main problem encountered in the model, however, is being unable to simulate the crushing behavior and corresponding failure mechanisms correctly. Figure 4.22 gives the crushed shape at the end of the simulation when the displacement is 6 mm. As can be seen from the right side of the figure, demonstrating the cross-sectional view from the middle of the specimen, instead of splaying of outer plies and micro-buckling in inner plies, a global buckling occurred which leads a catastrophic failure. Due to the excessive distortion, model is aborted at a crush distance of 6 mm and does not proceed. Even though the simulated crushing behavior is different from the experimentally observed one, it is interesting that FE model can still estimate the SEA of the composite structure accurately. The reason behind this can be explained by the repartition of the energy balance during the process. At early stages of deformation, although the order of occurrence and the distribution of damage modes differs from experimentally observed ones, overall energy absorbed by those damage modes can be consistent with the actual data. However, the main problem arises after some level of deformation, when the damage mode changes dramatically, and catastrophic failure occurs due to local buckling which terminates the model. Therefore, an artificial plug-initiator is introduced into the simulation to provide an accurate FE model in which damage modes can occur in the correct order and levels.

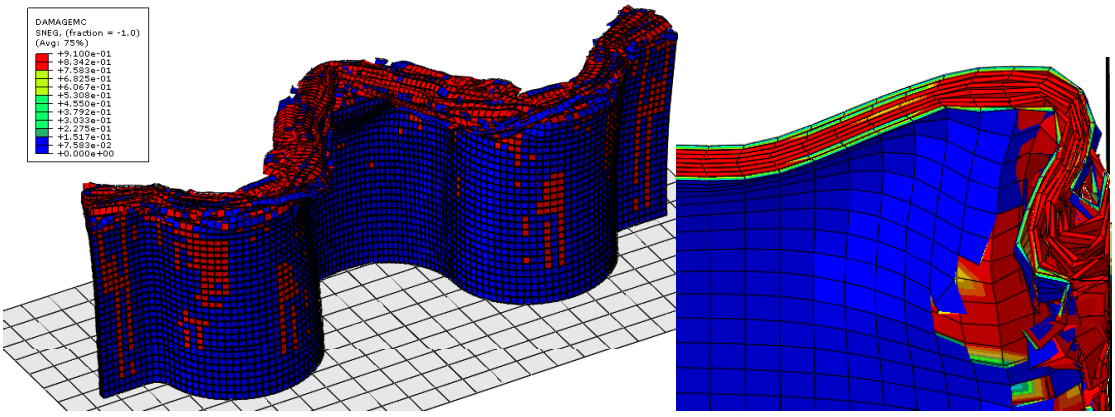

Figure 4.22. Simulated crushed shapes of sinusoidal specimen having 3 curvatures: isometric view with demonstrated matrix failure (left), and cross-sectional view from the mid-plane (right).

During the numerical study, various geometries for the plug-initiator are designed and tried within the FE Model. The purpose behind including the plug-initiator into the FE Model is to simulate the experimentally observed splaying mode and to create a V-shaped separation between delaminated plies which leads debris formation as occurred in actual tests. Figure 4.23 shows three types of plug initiator and their corresponding simulation results to show the evaluation of the damage. As can be seen from the figure, with the type III plug-initiator, FE Model shows consistency in terms of crushing morphology observed experimentally. Simulation results show that the model is successful to demonstrate the failure mechanisms accurately when compared with the actual tests. The numerical model can predict the specimen behavior consistently without global buckling mode and excessive distortion (see Figure 4.24). Moreover, in Figure 4.25, matrix crack growth at outer plies and the delamination growth at first interface is presented step by step which is also consistent with the actual damage progression.

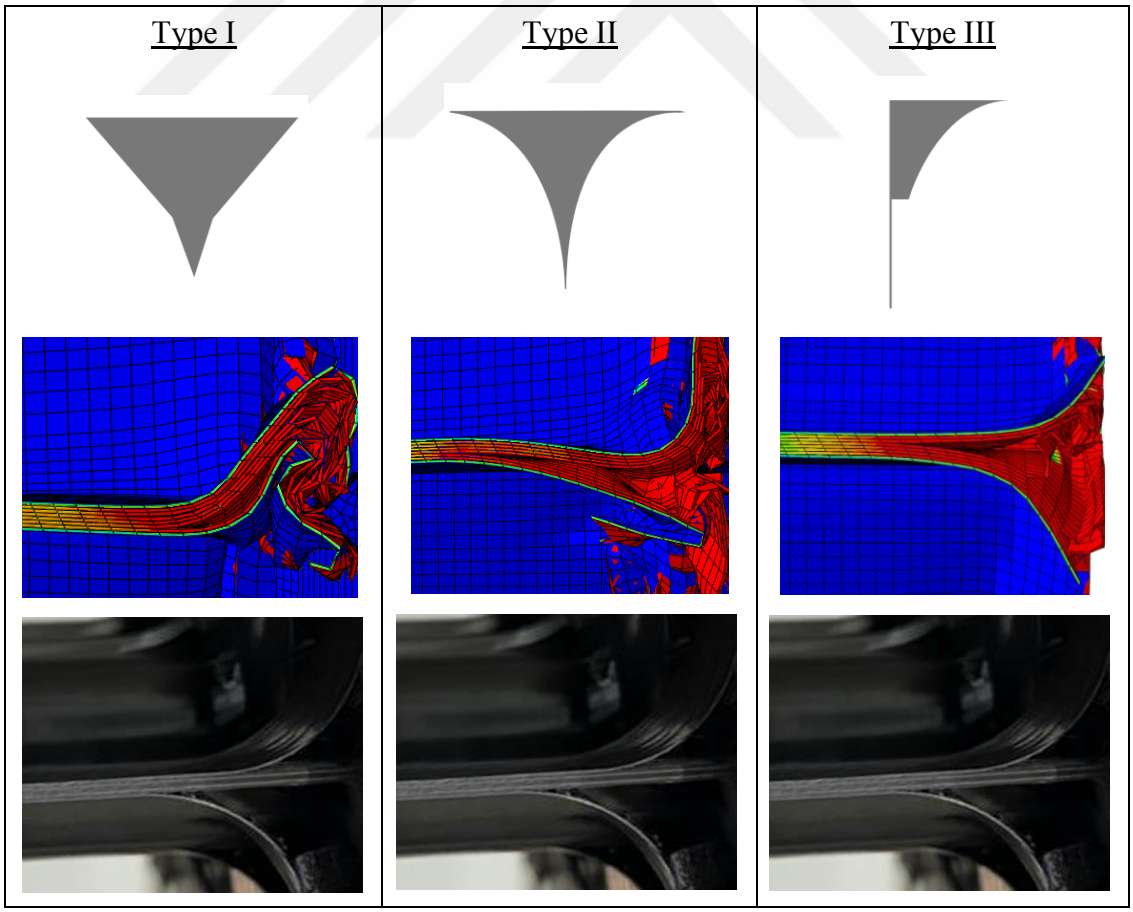

Figure 4.23. Evaluation of the artificial plug-initiator geometry and corresponding simulation results compared with the experimentally observed failure modes.

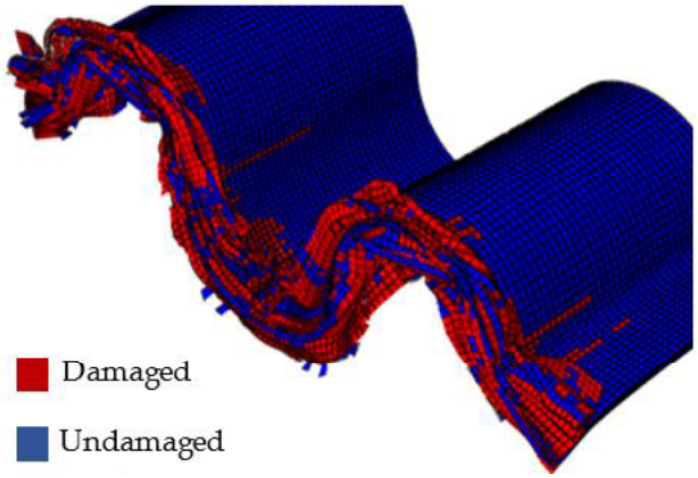

Figure 4.24. Simulated deformed shape with artificial plug-initiator.

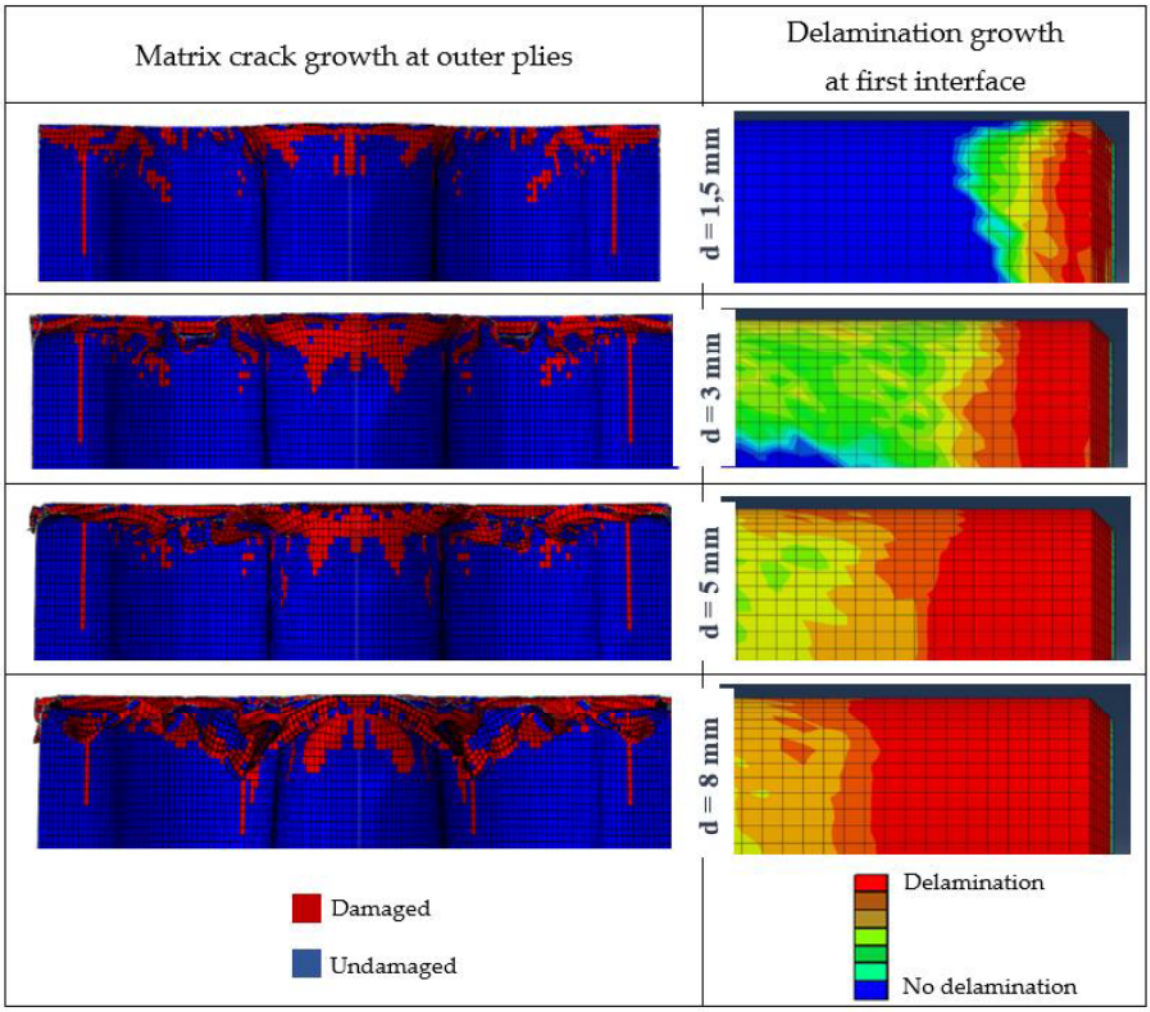

Figure 4.25. Matrix crack and delamination growth in FE Model with artificial plug-initiator.

Besides demonstrating crushing behavior correctly, FE Model with plug-initiator estimates the amount of energy absorbed during the crush event accurately. As can be seen from the Figure 4.26, numerical results enable more stability and show good agreement with the experimental tests in terms of load-displacement and energy curves.

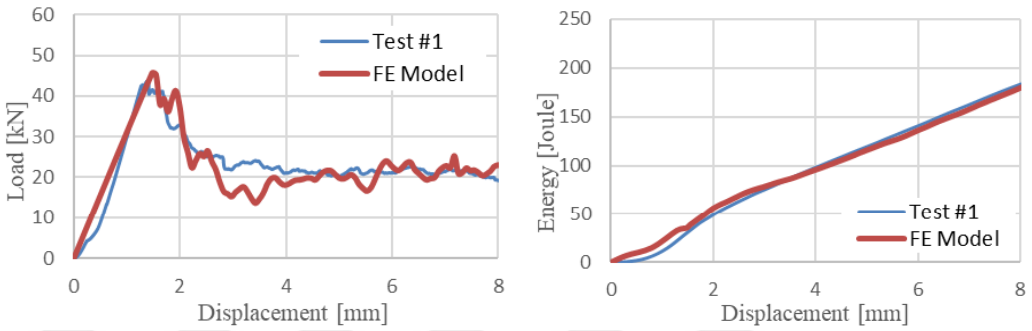

Figure 4.26. Comparison of FE model (with plug-initiator) with experimental tests: load-displacement curves (left), and energy curves (right) of sinusoidal having 3 curvatures.

FE model is also validated by applying the numerical analysis of sinusoidal structure with 5 curvatures. According to the results given in Figure 4.27, numerical results have a good correlation with the experimental data. Same approach is applied for sinusoidal specimens with 7 curvatures with same properties, boundary conditions, element types and artificial plug-initiator geometry. The results are presented in Figures 4.28 and 4.29. SEA value of the sinusoidal structure with 7 curvatures, which is the energy obtained from the area under the load-displacement curve per crushed mass, is calculated as 66,5 J/g.

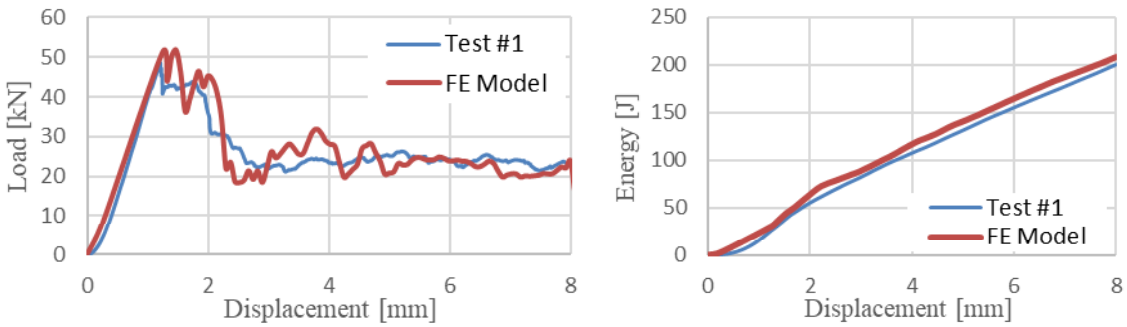

Figure 4.27. Comparison of FE model with experimental tests: load-displacement curves (left), and energy curves (right) of sinusoidal structure having 5 curvatures.

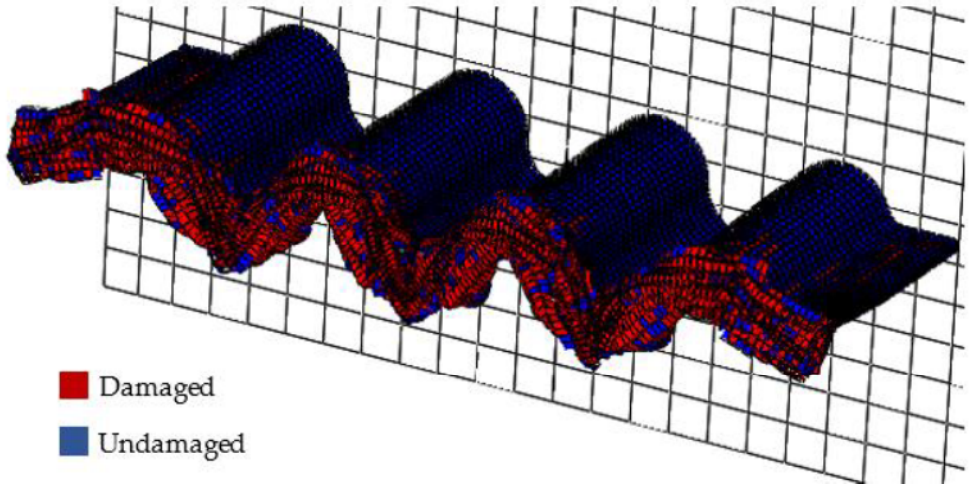

Figure 4.28. Simulated deformed shape of sinusoidal specimen with 7 curvatures.

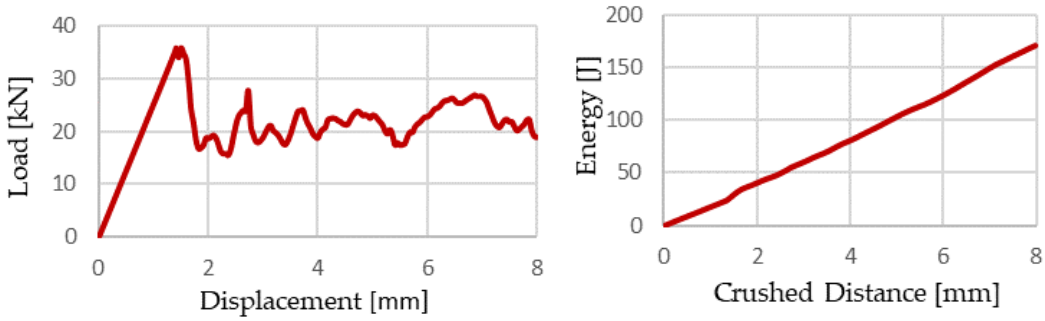

Figure 4.29. Simulation results of sinusoidal structure with 7 curvatures: load displacement curve (left), energy curve (right).

Figure 4.30 shows the overall comparison of SEA values for various geometries, and it can be seen that sinusoidal structure with 5 curvatures gives highest energy absorption capability. Beyond that structure, as the number of curvatures increase the performance related to energy absorption starts to decrease. The reason behind this observation can be explained with the decrease of aspect ratio. By decreasing the diameter of curvatures below a certain level to increase the number of curvatures, specimen geometry converges to the flat plate shape when its low width-to-length ratio is taken into consideration. Therefore, more instabilities are occurring, and the energy absorption performance is not getting higher than the five-curvature specimen.

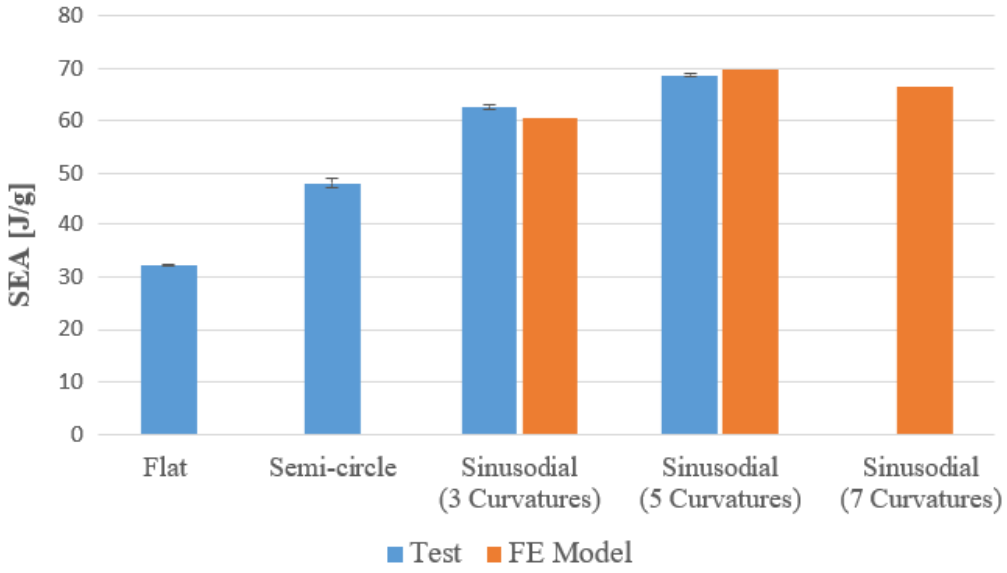

Figure 4.30. The overall comparison of SEA values of structures.

4.3.4. The Results of Novel Numerical Approach

The load-displacement and the energy results obtained from the novel FE model applied for the $[0/90]_{2s}$ sinusoidal specimen with 3 curvatures are compared with the experimental data as can be seen from Figure 4.31.

Load-displacement and energy results clearly show that the novel model with 3-interface in which interlaminar properties are doubled and the in-plane parameters are decreased according to the bending energy results can estimate SEA values of sinusoidal structure consistently in a shorter runtime when compared to conventional 7-interface FE models. Computational time required to complete the simulation was reduced by 46%, from 241 minutes to 130 minutes on a 16-core computer. In conclusion, it can be stated that this novel cost-effective approach developed for flat plates is proved to be applicable in the design process of complex geometries.

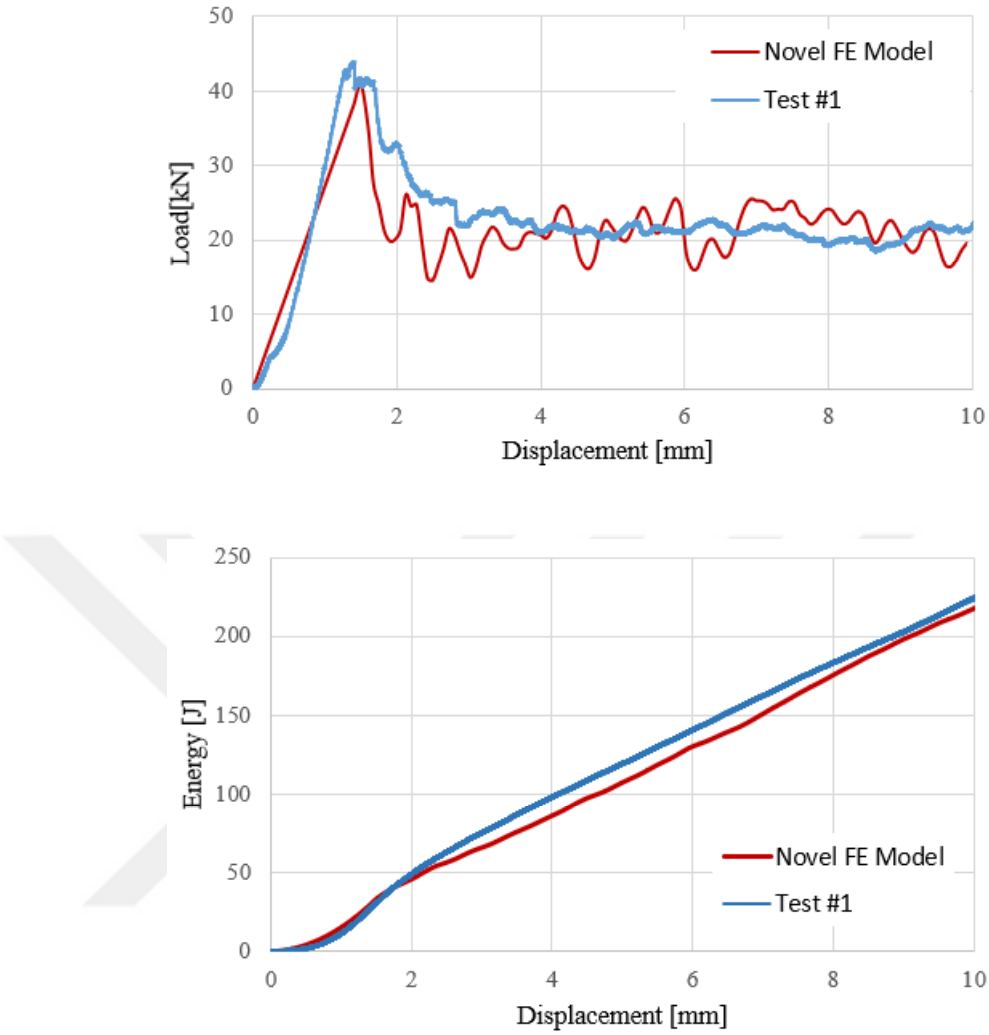

Figure 4.31. Comparison of the novel FE model of sinusoidal structure having 3 curvatures with experimental tests in terms of load-displacement (top) and absorbed energy curves (bottom).

5. DESIGN, ANALYSIS AND MANUFACTURING OF A CRASH BOX

The crashworthiness is the protection level of the occupants of vehicle in a crash event which depends on the rate of energy absorption and dissipation. Bumpers and crash boxes, for example, are crashworthy components equipped at the front and rear of the vehicles. During a crush event, it is expected from these structures to collapse and absorb as much crash energy as possible so that the damage of the frame is minimized, and lives of passengers are saved.

The experimental and numerical studies in literature have shown that typical metal tubes, which are still in widespread use as crashworthy structures, have SEA values between 15 and 20 J/g [98]. With more complex designs, this value can only increase to about 30 J/g for aluminum structures [99]. CFRP composite structures, on the other hand, are known to display better crashworthiness capabilities. As depicted in the previous chapters of this thesis work, a single unidirectional sinusoidal structure can absorb 68,72 J/g. This leads to the conclusion that the required amount of energy can be absorbed by composite structures with much lower weights than metallic ones. In fact, the SEA values can be increased even more by designing complex geometries in which multiple sinusoidal plates are combined in different configurations.

The main objective of this chapter is to design and manufacture a novel crash box geometry by combining two or more sinusoidal structures having 5 curvatures. In order to accomplish this goal, before the design phase, a preliminary study is required on how these sinusoidal parts will be joined. For this reason, in this chapter, the influences of nesting and adding T-joints on SEA of the complex structures are investigated first to decide which one is the most effective joining method for the crash box design. Then, several design attempts in ABAQUS/Explicit are made by merging a couple of sinusoidal structures having 5 curvatures. The final geometry performing highest energy absorption capability is manufactured and tested under quasi-static compression. In the final part of the chapter, tapering is applied to the crash box structure in order to decrease the initial peak load to

prevent an excessive deceleration causing a fatal damage to the passengers. Experimental results obtained from the tapered geometry are compared with the previous data.

5.1. The Influence of Nesting

This section contains the manufacturing and testing of a complex composite structure obtained by nesting of two sinusoidal geometries so that the influence of the joining method on energy absorption capability can be investigated. Nesting is a joining technique made by creating vertical line cuts in two separate composite specimens, which are then interlocked and glued together.

In the beginning of the specimen preparation process, two sinusoidal composite structures with 5 semi-circle curvatures are manufactured by using AS4/8552 UD prepregs (for the details on the manufacturing process and the final dimensions of single sinusoidal structure, please see Section 4.1). Vertical cuts are then made by diamond disk cutter in the center of each sinusoidal specimens at half of their lengths. Finally, the two specimens are merged by using epoxy resin-based adhesive so that the cut areas overlapped each other. Figure 5.1 demonstrates two separate sinusoidal specimens in which vertical cuts are created before the assembly. The final state of the nested structure is depicted in Figure 5.2.



Figure 5.1. Two sinusoidal composite specimens with vertical line cuts.

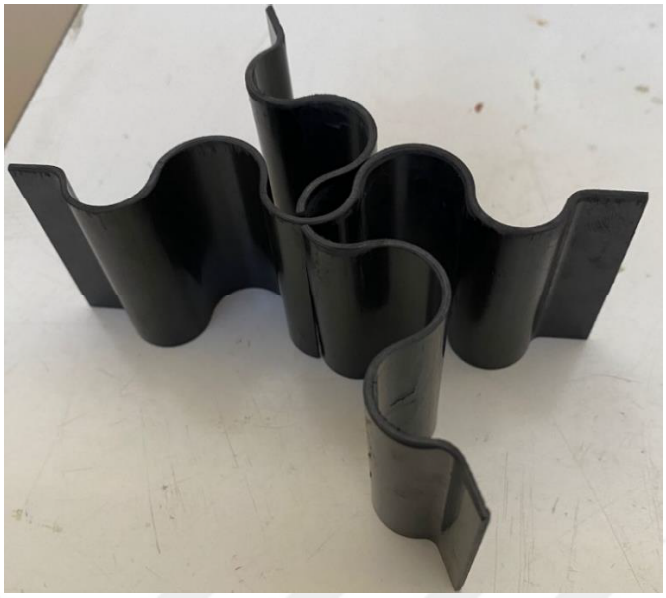

Figure 5.2. The nested composite structure.

The structure is tested in the Zwick Z100 testing machine with quasi-static speed of 1 mm/min and the load-displacement results with crushed morphology are given in Figure 5.3. SEA value of the structure is calculated by dividing the total amount of energy to the mass of crushed material and the result is compared with the performance of the single sinusoidal specimen (see Table 5.1).

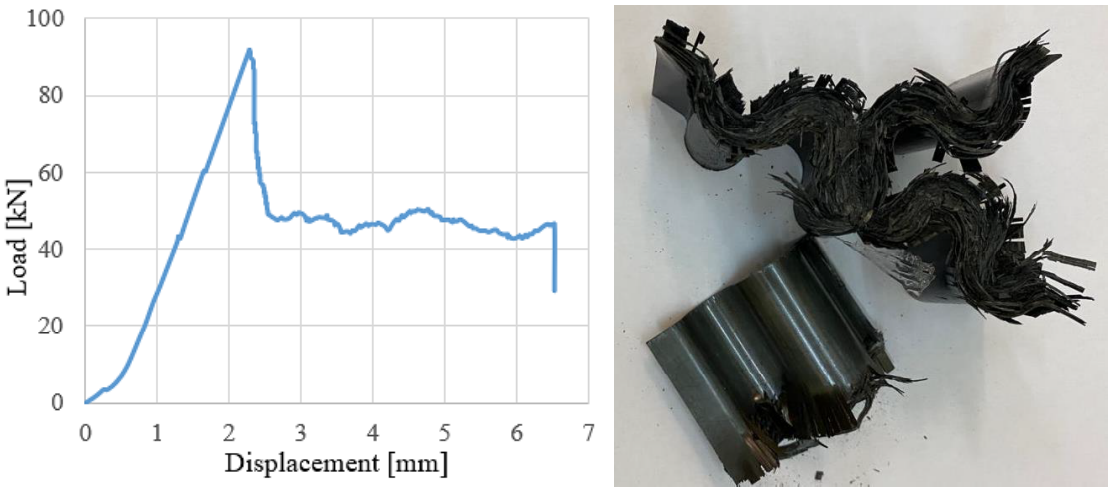

Figure 5.3. Experimental results of the nested structure: load-displacement curve (left), crushed morphology (right).

Table 5.1. SEA of nested structure and the difference from the single sinusoidal.

Crushed Distance [mm]	Crushed Mass [g]	Absorbed Energy [J]	SEA [J/g]	Difference from Single Sinusoidal
6.51	4.173	295.9	70.9	3.17%

The method of a forming a complex structure by nesting two separate sinusoidal specimens, which has an advantage of being easy to implement in a short amount of time, was considered to observe whether or not it could significantly improve the energy absorption capability. However, the results given in Table 5.1 show that by using the nesting method, the SEA of the structure can only be increased marginally by 3.17%. This increase is because the junction point leads the splayed layers intertwined and more fragmentation occurs. On the other hand, when the crushed displacement reached to 6.5 mm, the stress concentration at the ends of the cut line segments causes a catastrophic failure that terminated the process. This makes the structure impractical in terms of crashworthiness since it cannot provide a stable energy absorption mechanism until the specimen is crushed to the end. This outcome led to investigation of another method to combine sinusoidal plates by designing a complex structure having T-joint connection points.

5.2. The Influence of Adding T-Joints

In the previous section, as an idea of creating a complex structure, the influence of nesting on SEA was investigated and the results showed that besides the fact that energy absorption capability improved only marginally, the progressive failure of the composite structure was also interrupted by a sudden catastrophic failure. Unlike nesting, which involves joining previously manufactured parts by using an adhesive, it would be more beneficial to obtain a one-piece complex structure having T-shaped joints which are created directly during the composite manufacturing phase. Therefore, this section aims to understand the influence of adding T-joints in the complex shape on the SEA performance of the composite structure. For that purpose, a corrugated specimen having 4 T-joints will be manufactured and tested under quasi-static compression load so that it can be seen

whether there will be an increase in the performance by comparing with the results of previous samples. It is worth mentioning at this point that T-shaped joints, just like reflection points on sinusoidal geometry, are expected to create extra obstacles and therefore increase the amount of energy absorbed by unit mass.

The corrugated structure is manufactured by using the same process in autoclave as detailed in previous chapters. The UD AS4/8552 prepregs are stacked with $[0/90]_{2s}$ configuration by winding around steel moulds having rectangular cross sections. The cross-sectional view of the structure with required dimensions and the schematic representation of the lay-up method are given in Figures 5.4 and 5.5.

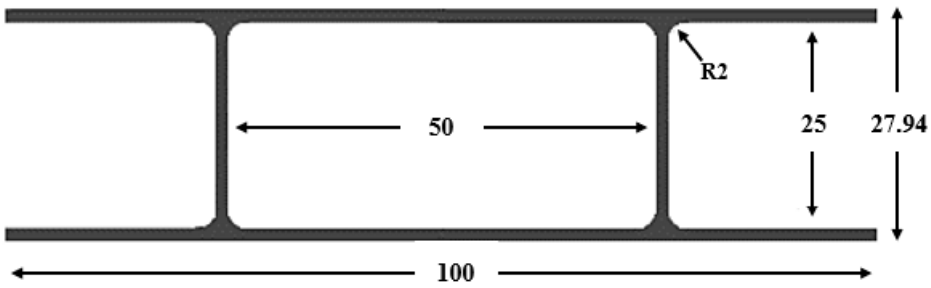

Figure 5.4. Cross-sectional view of corrugated structure (All dimensions are given in mm.).

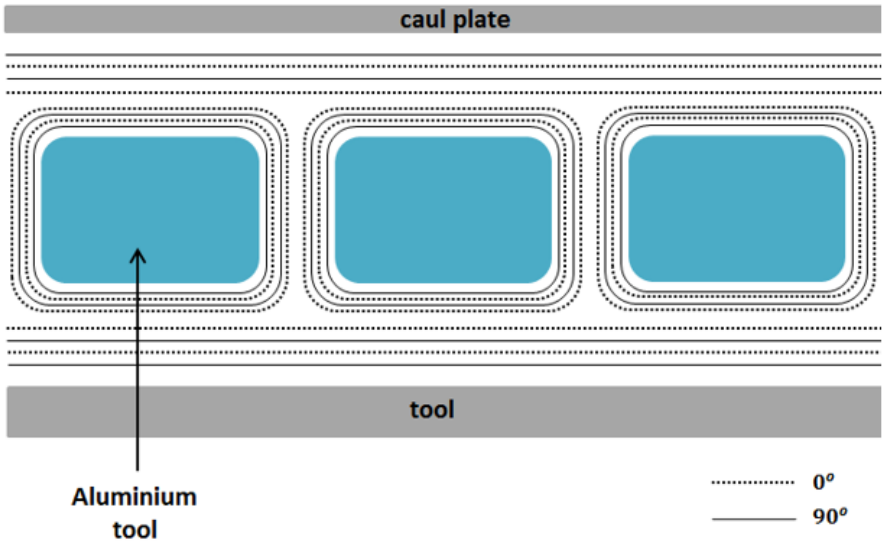

Figure 5.5. The lay-up method utilized in the manufacturing process of AS4/8552 corrugated structure.

The manufactured structures with 1.47 mm thickness are then cut by a water cooled diamond disk into parts with the dimensions specified in Figure 5.4 and the length of 60 mm. The close-up photo of one of the specimens is presented in Figure 5.6**.** The specimen is tested at a quasi-static speed of 1 mm/min.

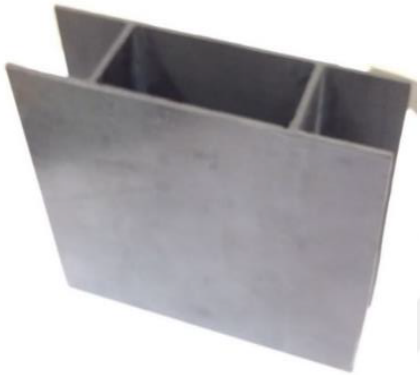

Figure 5.6. Test specimen.

The load-displacement curve and the crushed morphology obtained at the end of the testing phase are given in Figure 5.7. SEA value of the structure is calculated by division of the total amount of energy (area under the load-displacement curve) to the mass of crushed material. The energy absorption capability of the corrugated structure having 4 T-joints is compared with the performance of the flat plate (see Table 5.2).

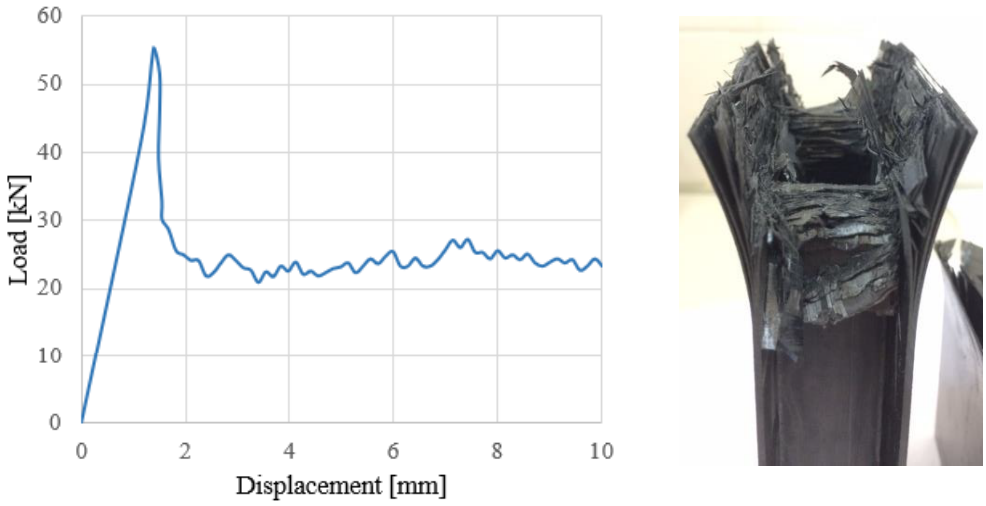

Figure 5.7. Experimental results of the corrugated structure: load-displacement curve (left), crushed morphology (right).

Table 5.2. SEA of corrugated structure and the difference from the flat plate.

Crushed Distance [mm]	Crushed Mass [g]	Absorbed Energy [J]	SEA [J/g]	Difference from the Flat Plate
10	4.89	216.1	44.19	37.5%

The results given in Table 5.2 show that by using this method, the SEA of the structure is increased by 37.5% when compared to the SEA of single flat plate. This increase can be explained by the fact that more fragmentation occurs in regions near T-shaped joints than in the flat plate alone. Since, T-joints leads the splayed layers intertwined, instead of long matrix cracks occurring between layers, more fiber breakages are seen which directly increases the level of absorbed energy. More importantly, unlike the nested structure, this corrugated structure provides a progressive failure and consequently a stable energy absorption until the specimen is totally crushed without the occurrence of catastrophic failure. Therefore, based on the results obtained up to this point, utilizing T-shaped joints to connect multiple sinusoidal structures will be preferred when designing the complex structures with high SEA performances.

5.3. Design of a Complex Composite Crash Box Structure

This section presents the design process and the numerical analysis of the crushing behavior of the three novel crash box geometries. As shown in Figure 5.8, the design idea of the crash box structure is to combine sinusoidal plates having 5 semi-circle curvatures by using the T-shaped joints.

Table 5.3 gives the cross-sectional views of three designed crash-box geometries. Each subsequent design attempt is made with the aim of improving its SEA characteristics over the previous one.

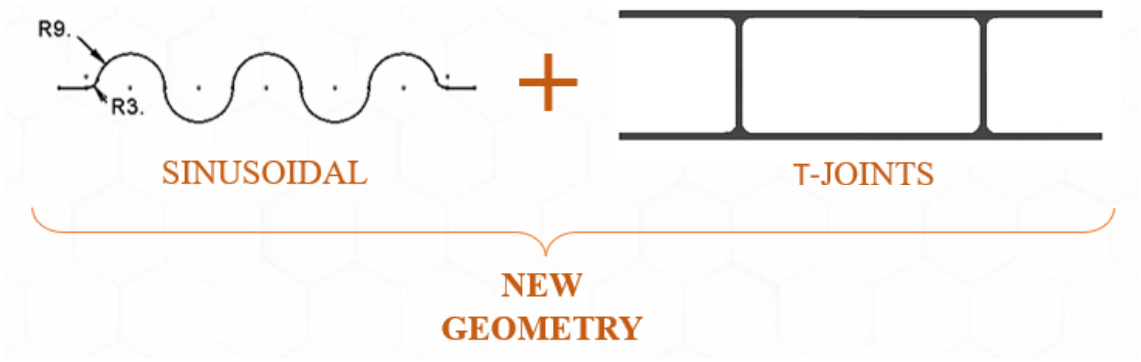

Figure 5.8. The design idea of the novel crash box geometry.

The first geometry which is named as “Parallel Sinusoidal Plates” is the combination of two sinusoidal structures with two vertical flat components in which 4 T-Joints are inserted. Since creating curvatures is known to increase the energy absorption capability in a considerable amount when compared to flat parts, next geometry is designed to have a circular core with 4 bisected sinusoidal arms connected with T-shaped connections to this core. Second geometry is named as “Sun-like Shape”.

In the final geometry, then, the influence of adding more bisected sinusoidal arms to the circle on the performance of structure was considered so that “Sun-like Shape” having 8 half arms is designed. It should be noted that all sinusoidal plates used in three different designs have the same dimensions and properties as the structure tested in the previous chapter and proven to have the highest SEA characteristics.

As the next step, FE models of the progressive failure behavior of these three geometries under quasi-static compression are created in ABAQUS/Explicit in which novel numerical approach is applied. The SEA results obtained from these models will be presented in the next section and is used to determine which geometry should be manufactured. At that point, manufacturability will also be another important evaluation criteria.

Table 5.3. Three crash box designs (All dimensions are given in mm).

Name	Code	Geometry
Parallel Sinusoidal Plates	**PSP**	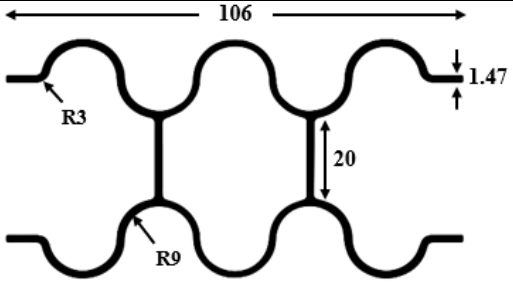
Sun-like Shape With 4 Half Sinusoidal Arms	**SL4**	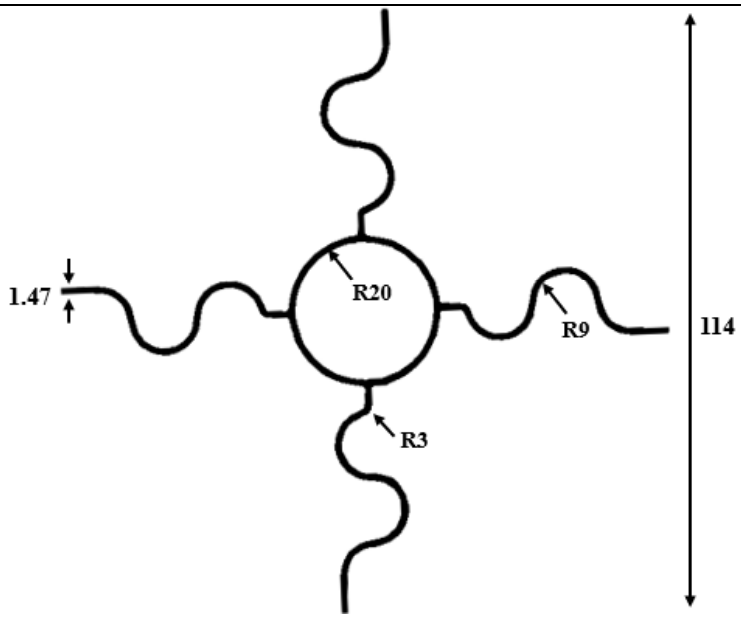
Sun-like Shape With 8 Half Sinusoidal Arms	**SL8**	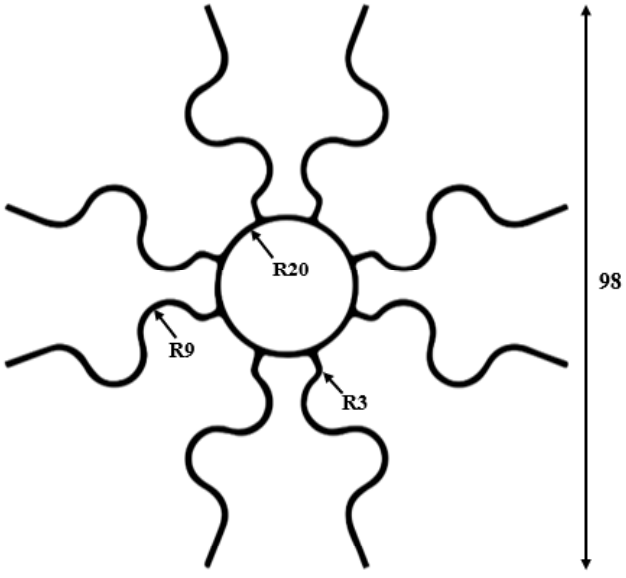

5.3.1. Numerical Analysis

The novel FE approach that leads reasonable run times has been developed and validated for both flat plates and sinusoidal structures sections 3.32 and 4.3.4. As a reminder, the modelling idea was to extrude four [0/90] sub-laminates with one element through the thickness representing eight individual plies stacked with $[0/90]_{2s}$ configuration. Besides, to obtain consistent results, the approach also consists of the regulation of the interlaminar and intralaminar parameters: halving the in-plane properties and doubling the fracture toughness while increasing the interfacial strength by %41. The rationale and the underlying theory of parametric adjustments can be reviewed in Chapter 3.

In the current section, same novel modelling approach is now applied to three crash box geometries made of AS4/8552 carbon/epoxy UD prepregs. The developed numerical analysis allows to obtain SEA results, and thus enables to make comparative analysis in a much less time than conventional models. Considering the complexity of geometries, using this approach will save a significant amount of time in the design process.

In numerical analysis, the design named “Parallel Sinusoidal Plates” is first analyzed by modelling one quarter of the geometry with the plug initiator proposed in the previous section. In this model, each of the four sub-laminates were meshed with 1 mm continuum shell elements (SC8R). The imposed velocity and boundary conditions are kept the same with the previous models applied for flat and sinusoidal specimens. Figure 5.9 demonstrates the Abaqus/CAE model with a close-up of the trigger mechanism and the plug initiator. Due to the complexity of the geometry, the 45° chamfer is not possible to apply at the edge but there is a still requirement of a trigger in order to exhibit realistic delamination behavior and prevent global buckling. That’s why, in the FE model, V-shaped trigger is applied at one edge of the structure where the plug initiator is supposed to hit. Figure 5.10 shows the close-up photo of V-shape trigger and the lay-up configuration throughout the thickness.

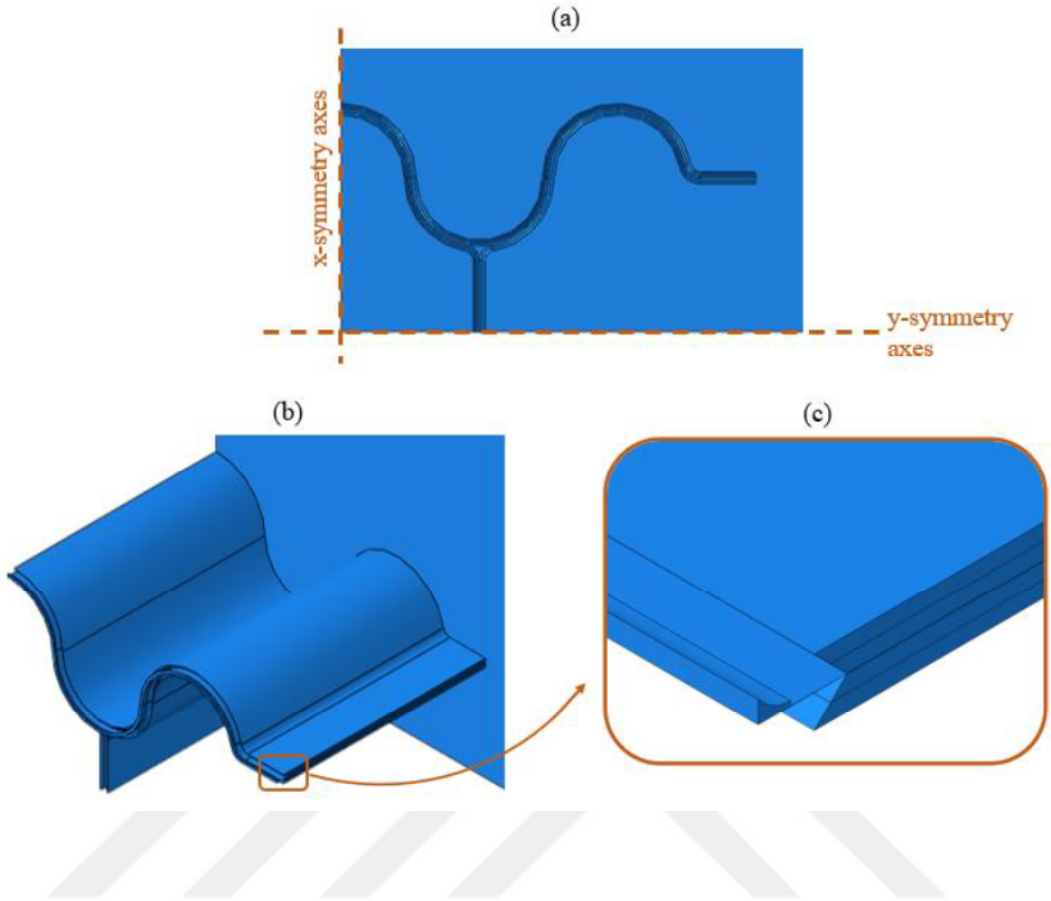

Figure 5.9. Abaqus/CAE model of PSP geometry: (a) front view with symmetry axes, (b) isometric view, (c) one edge with plug initiator.

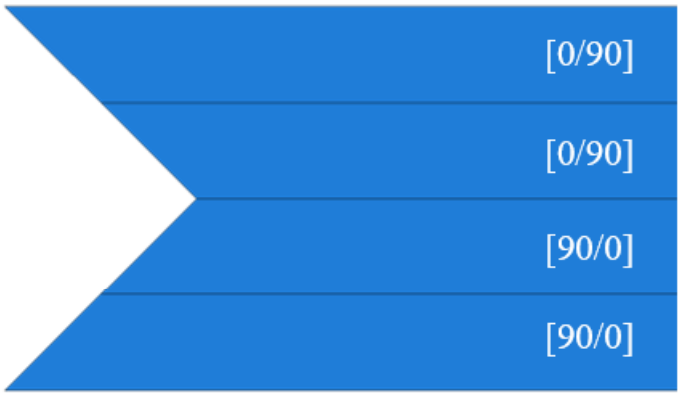

Figure 5.10. The schematic representing four layers and V-shaped trigger.

After the numerical analysis of PSP geometry, the FE models for SL4 and SL8 geometries are also implemented with the same approach, trigger mechanism and conditions (see Figure 5.11). The numerical analysis of SL8 geometry is implemented as again in a quarter model, while the crushing behavior of the SL4 geometry is analyzed by a full-geometry model since it has not a symmetrical structure. The results are presented and discussed in the following section.

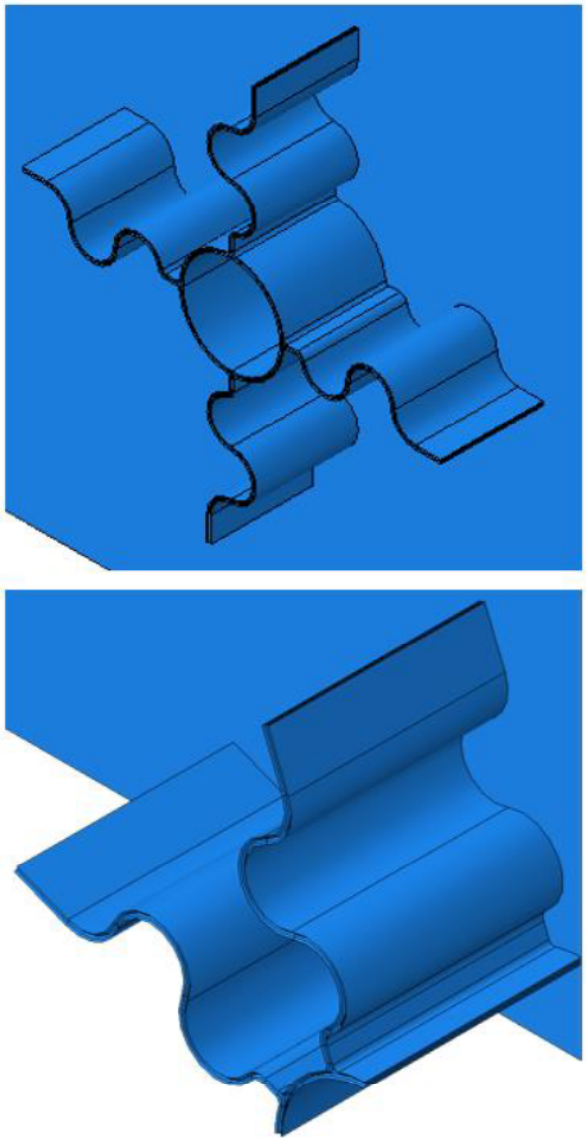

Figure 5.11. Abaqus/CAE models of SL4 (top) and SL8 (bottom) geometries.

5.3.2. Numerical Results

The simulation of the crushing modes of the PSP geometry are presented in Figure 5.12 in which fiber, matrix damage and delamination are demonstrated. As can be seen from the figure, there is an intense fiber damage observed in the regions close to the contact zone where delamination has already occurred. The sinusoidal parts at the top and the bottom also exhibit vertical ruptures due to the intense matrix failures. However, there is no matrix damage occurring on the sidewalls of the flat parts positioned at the center which is estimated to lower the SEA performance. The load-displacement curve obtained at the end of the simulation is presented in Figure 5.13.

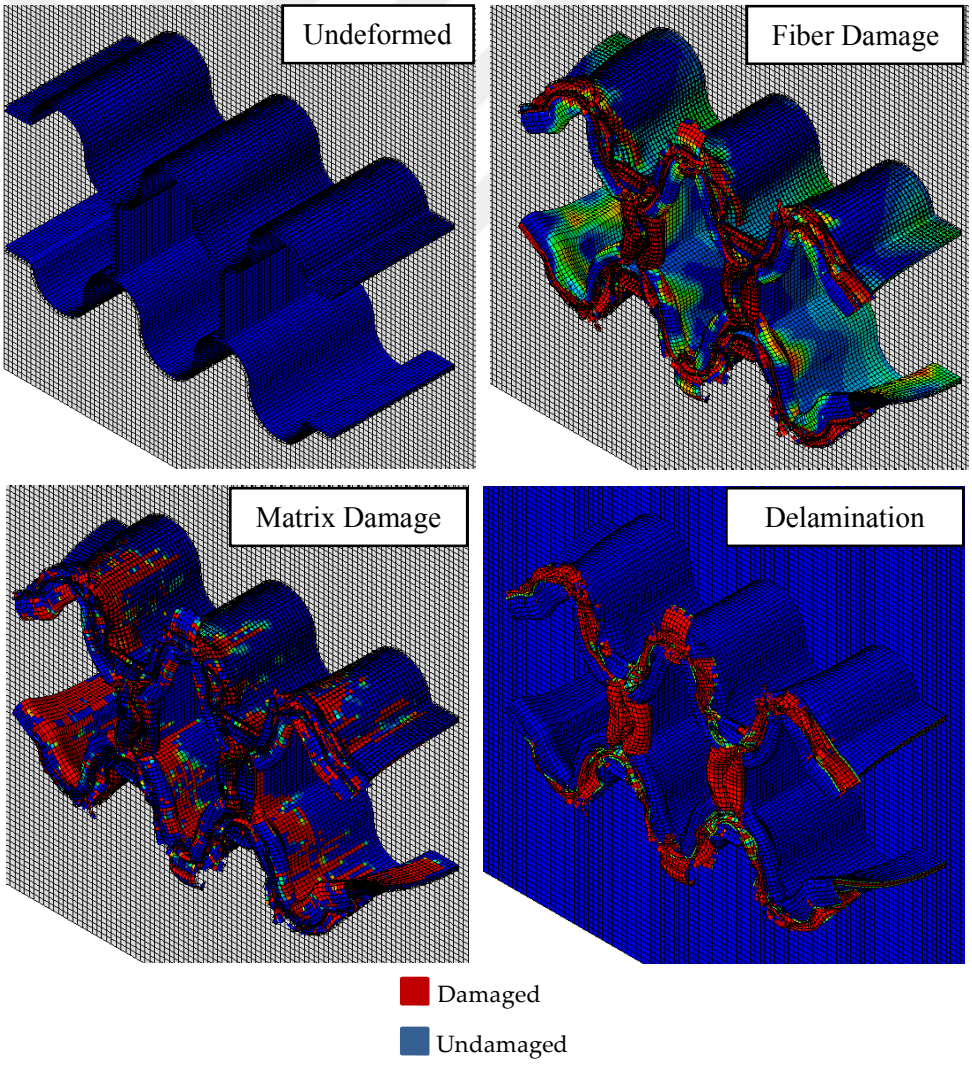

Figure 5.12. Simulation results of PSP geometry.

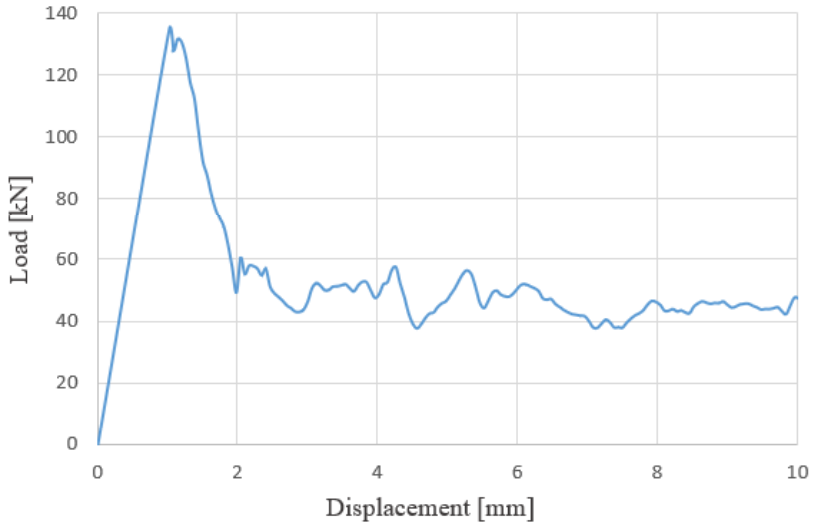

Figure 5.13. Load-displacement curve of PSP geometry.

The load-displacement curve obtained at the end of the simulation of SL4 geometry is depicted in Figure 5.14. The crushing modes obtained by the FE model developed for the SL4 geometry are presented in the Figure 5.15. In addition to fiber failure and the delamination in the regions close to the contact zone, matrix failure is also observed in the middle plies and on the sidewalls of the sinusoidal and circular parts. As mentioned before, rather than flat parts, a circular core placed at the center of the region was expected to increase the SEA performance. Simulation results confirm this prediction so that more vertical ruptures, and the corresponding micro-buckling and fiber damages are observed in the circular region.

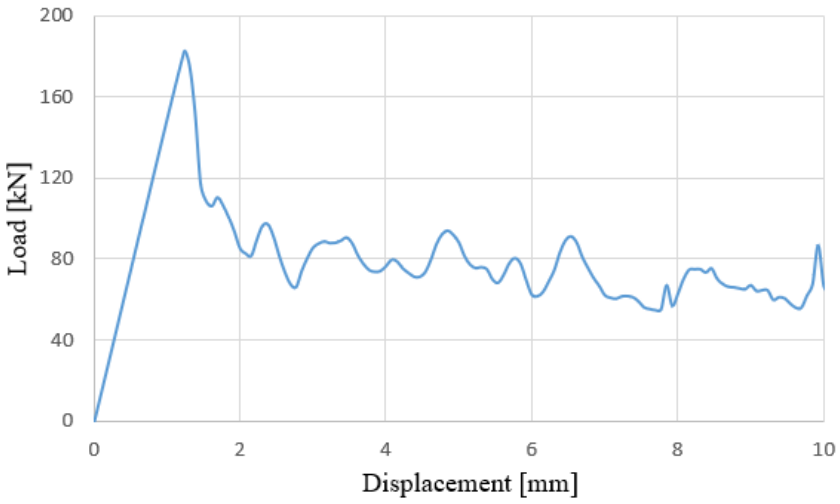

Figure 5.14. Load-displacement curve of SL4 geometry.

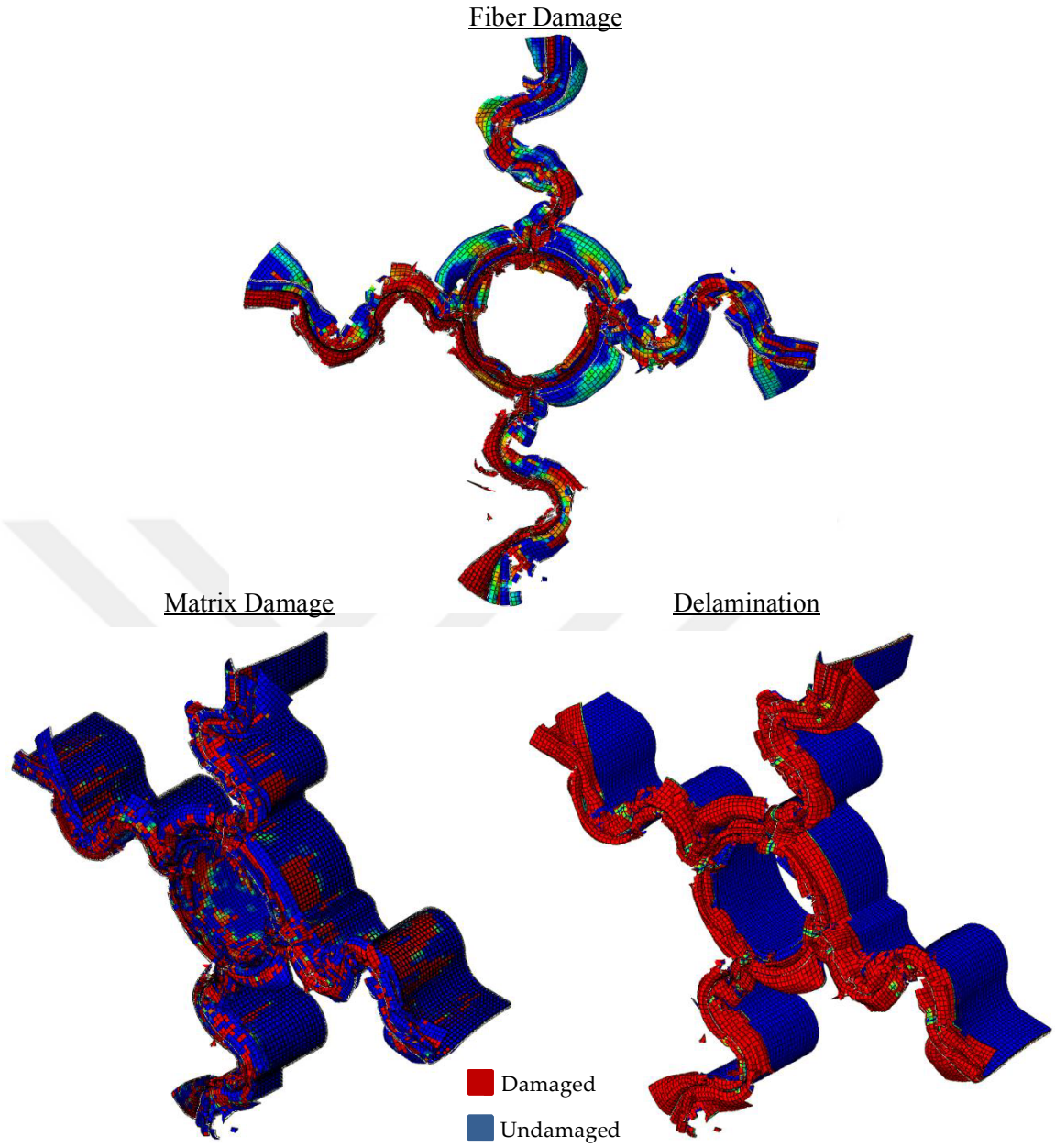

Figure 5.5. Simulation results of SL4 geometry.

The crushing modes in the simulation of the SL8 geometry are presented in the Figure 5.16. The failure mechanisms are quite similar to the previous geometry since both of the geometric designs consist of sinusoidal arms connected to the circular core.

Unlike the previous one, since the sinusoidal plates are positioned closer to each other in SL8 geometry, the damaged plies intertwine and increase the level of fiber fracture near the T-joints which has a direct effect to increase the SEA performance. On the other hand, the fibers near the T-joints are already broken in a considerable amount, the increase in SEA value will not be very large when compared to the energy absorption capability of SL4 geometry. The load-displacement curve obtained at the end of the simulation is depicted in Figure 5.17.

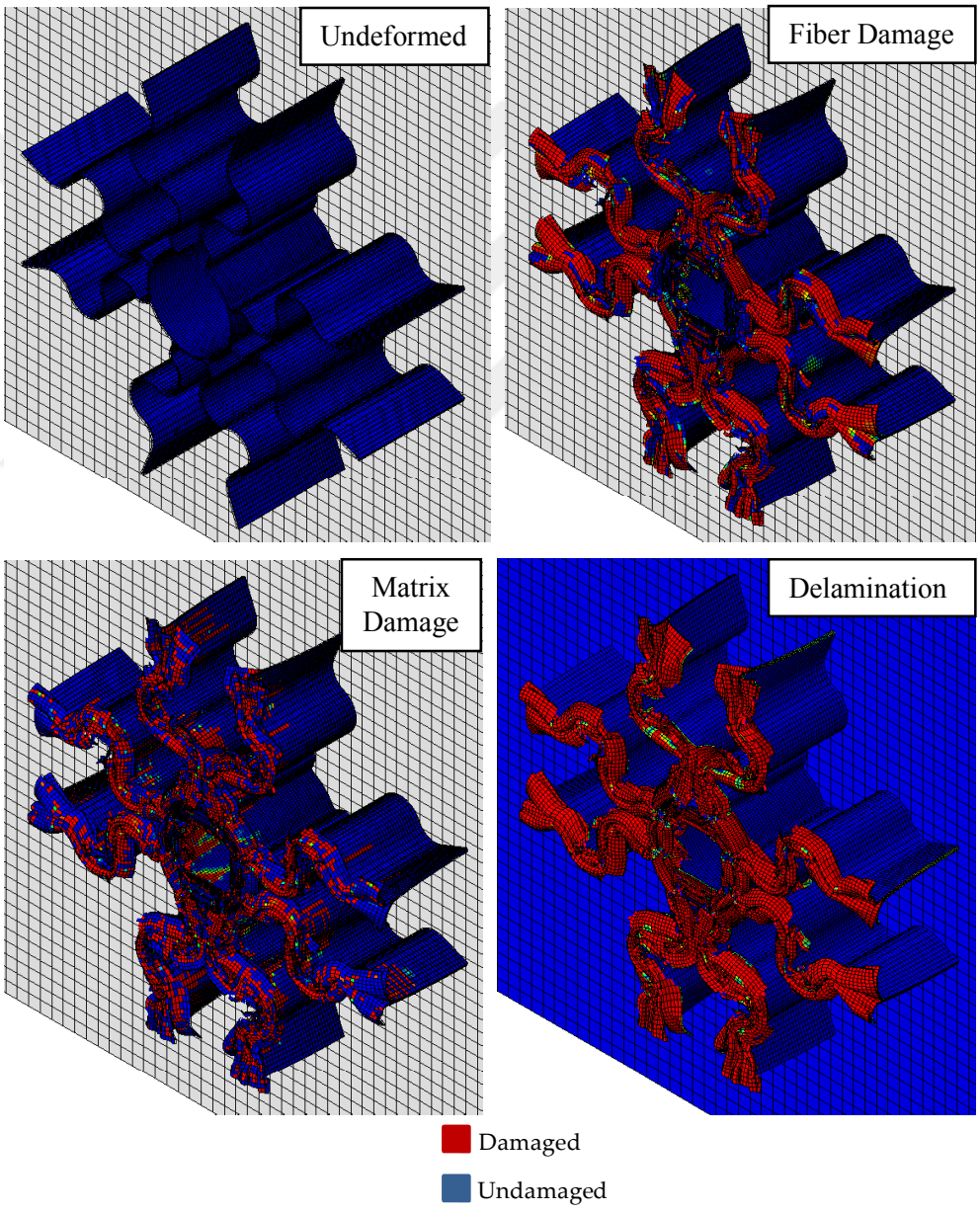

Figure 5.14. Simulation results of SL8 geometry.

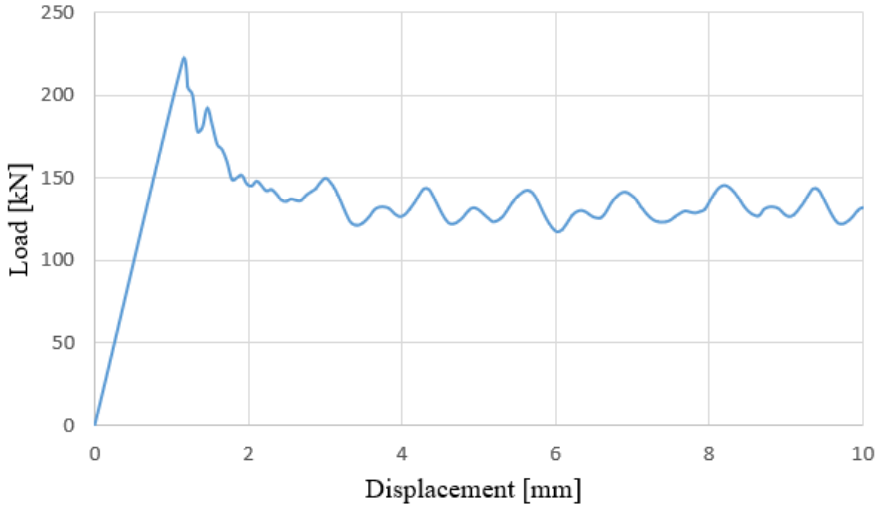

Figure 5.15. Load-displacement curve of SL8 geometry.

After the simulations are completed, SEA values for each geometry are calculated by dividing the area under the load-displacement curves to the mass of crushed specimen and the results are compared in order to decide which geometry to manufacture.

Table 5.4 shows the SEA results with the mass of the crushed specimen and the amount of absorbed energy at the end of the crushing process. Results show that the PSP geometry does not provide a substantial increase in the SEA performance. The reason behind this outcome is that although T-joints are performance enhancing elements, the flat parts reduce the SEA value. On the other hand, Sun-Like shapes with the circular core provide a significant advantage in terms of energy absorption capability over both the single sinusoidal plate and the recently designed PSP geometry. While SL4 geometry can absorb 16% more energy per unit mass than the single sinusoidal, the SEA of SL8 geometry is increased by 20% (see Figures 5.18 and 5.19).

Table 5.4. Comparison of the SEA performances of the three geometries.

Geometry	**Crushed Distance [mm]**	**Crushed Mass [g]**	**Absorbed Energy [J]**	**SEA [J/g]**
PSP	10	7.62	521.08	70.64
SL4	10	9.65	769.15	79.70
SL8	10	16.45	1358.02	82.55

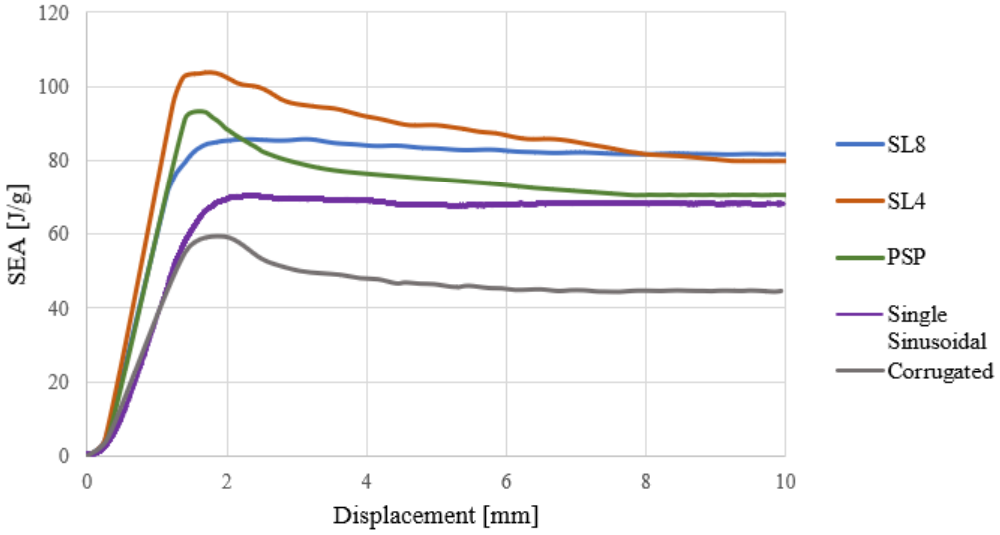

Figure 5.16. SEA vs Crush Distance plots for five different geometries.

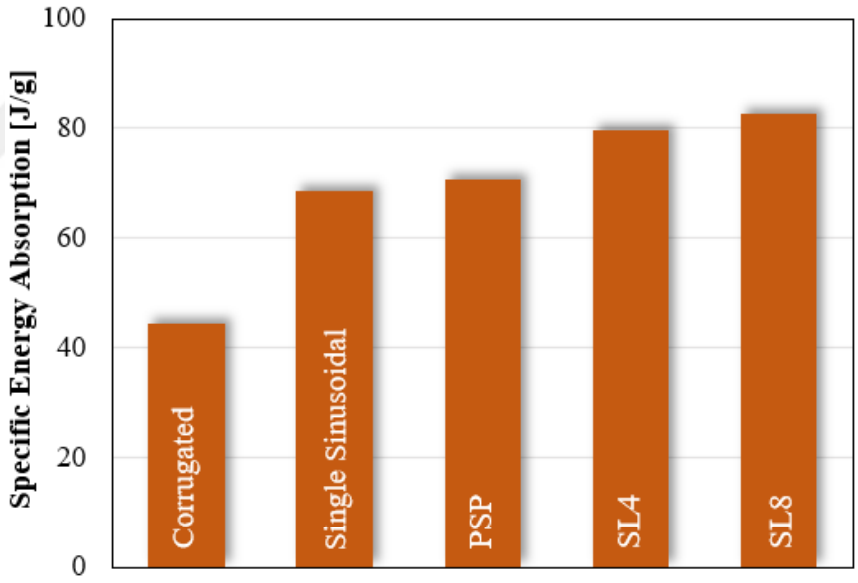

Figure 5.17. General SEA comparison.

It can be deduced from the results that Sun-like geometry is a good candidate as an energy absorber crash box structure. Between the two structures having 4 and 8 sinusoidal arms, there is no prominent difference in terms of energy absorption capability so that the manufacturability becomes an important criterion in deciding which structure should be selected. Considering the shape and number of the molds required for the manufacturing process and the suitable laying up conditions without space constraints that may reduce

quality, it can be said that the SL4 geometry is more preferable than SL8 structure for a defect-free production. In SL8 geometry, on the other hand, the small radius at the area close to the T-shaped joints would probably lead difficulties in laying up the prepregs properly, and thus would result in defected zones. All in all, as the next step of the thesis work, it is decided to manufacture and test Sun-like geometry having 4 half sinusoidal plate arms.

5.4. Manufacturing and Testing of Sun-like Geometry

The sun-like geometry is manufactured from Hexcel AS4/8552 carbon-epoxy UD prepregs by using the hand lay-up technique. In order to be able to manufacture such a complex composite structure, again custom designed steel molds are required. Therefore, four steel molds are designed and manufactured by using wire electro-discharge machining process after which the surfaces are mirror-polished.

During the manufacturing of the composite part, 8 plies of prepregs in total are stacked with $[0/90]_{2s}$ cross-ply configuration: 4 layers on the custom-made curved steel molds with [0/90/0/90] configuration and 4 layers on the cylindrical tube to be placed in the middle with [90/0/90/0] configuration. Then, the molds are closed and vacuum bagged, and the manufacturing process was completed in the autoclave. The snapshots representing the placement of molds with the prepregs laid on them can be seen in Figure 5.20.

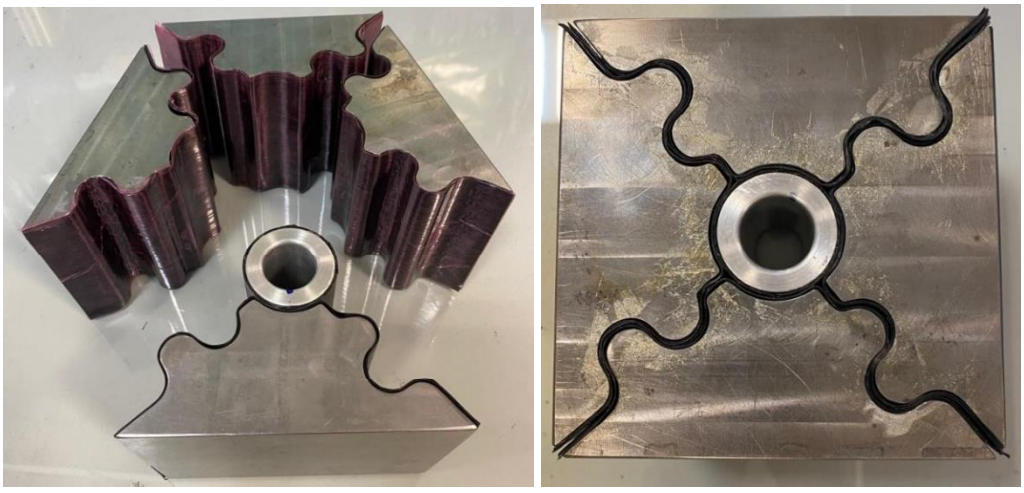

Figure 5.18. Snapshots taken during the manufacturing process.

Manufactured specimens are then cut to 50 mm in length and the chamfer is machined to one edge of them. Two specimens are then tested at a quasi-static speed of 1 mm/min by using the MTS hydraulic testing machine with a load capacity of 500 kN in the Construction Materials Laboratory at İstanbul Technical University. Figure 5.21 demonstrates the final product and the test setup.



Figure 5.19. Manufactured sun-like geometry (top) and the test setup (bottom).

The crushed morphology at the end of the experimental test and the load-displacement curve are presented in Figures 5.22 and 5.23. Moreover, the SEA values of the two specimens with the total amount of energy absorbed after 20 mm crush and the mass of crushed material are given in Table 5.5.



Figure 5.20. The deformed shape of sun-like geometry at the end of the test.

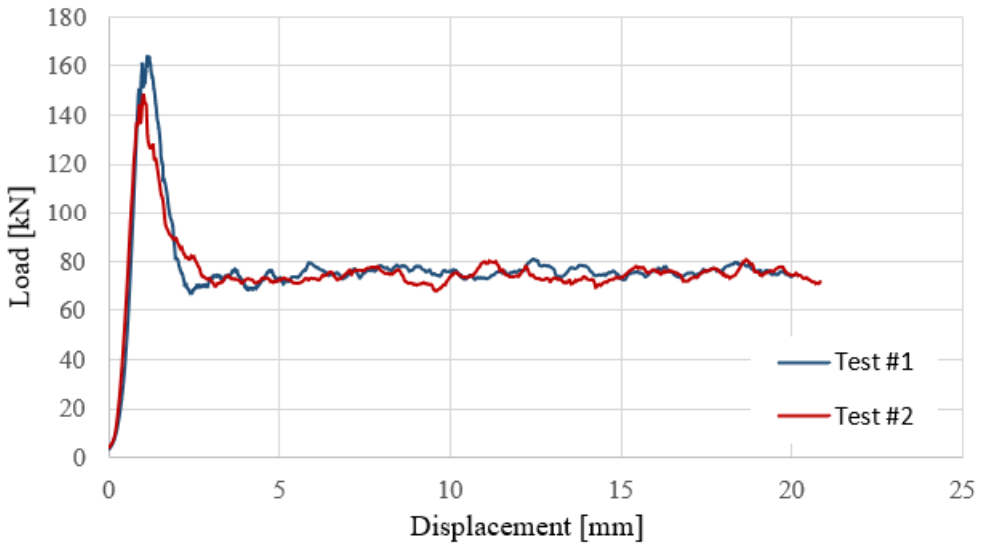

Figure 5.21. The load-displacement curves of SL4 geometry obtained from tests.

Table 5.5.The SEA values of SL4 structures.

Specimen No	SEA [J/g]	Average
#1	79.95	79.46
#2	78.97	

When the experimental results of SL4 geometry are compared with the data taken from the numerical analysis, there is a good agreement in both load-displacement and energy curves (see Figure 5.24). Thus, the consistency of the novel modeling approach developed in this thesis work is once again proven.

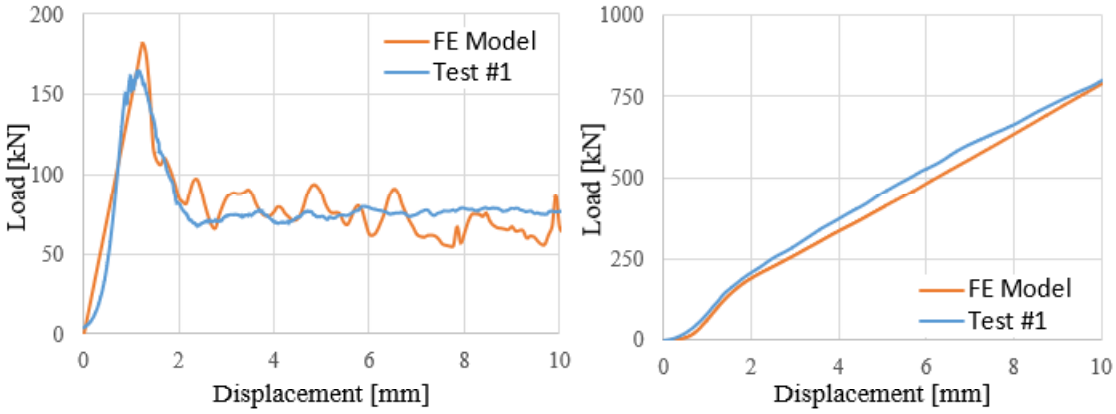

Figure 5.22. Comparison of the novel FE model of SL4 structure with experimental tests in terms of load-displacement (left) and energy curves (right).

5.5. A Solution to Decrease the Peak Load: TAPERING

In the previous section, both numerical and experimental investigations have been carried out for the crushing process of Sun-like structure and the results showed that the designed geometry exhibited a superior energy absorption capability. The high initial peak load, on the other hand, is still an issue since it may cause an excessive deceleration and thus a fatal damage on the passengers (see Figure 5.23). This section aims to develop a solution to decrease the level of peak load on the load-displacement curve. The idea is to taper sinusoidal arms of the Sun-like structure by linearly reducing the length (starting from the T-joints at the end of the circular core to outer radius of the total structure) and to achieve a partially conical geometry. By doing this, the rise-and-fall trend in the load-displacement curve for the first 3 mm displacement is expected to change and the load will gradually reach the mean level at the stable zone.

For this purpose, the sinusoidal arms of the manufactured sun-like specimen are tapered by first diamond disk cutter so that the edges are reduced by 5 mm. A better symmetry of the tapered arms is achieved by sanding the edges with emery paper. It is important to state at this point that it is not possible to achieve perfect symmetry in the structure since it was a hand-made process. However, the specimen preparation process in also not considered problematic since it does not have a serious impact on the overall objective. Figure 5.25 demonstrates the finalized tapered geometry.



Figure 5.23. The tapered geometry.

The tapered structure is tested in the MTS hydraulic testing machine and the experimental results are presented and compared with the non-tapered, original geometry in Figure 5.26. The results show that tapering eliminates the peak load just as predicted, and after a while, it still allows the load to fluctuate around to the same mean value as in the original geometry. Table 5.6 shows the comparison between the SEA values of the tapered non-tapered geometries. Even though the area under the curve decreased due to the change in load-displacement trend, the SEA value of the tapered geometry is still close to the previous one since the amount of material has also decreased for the first 5 mm.

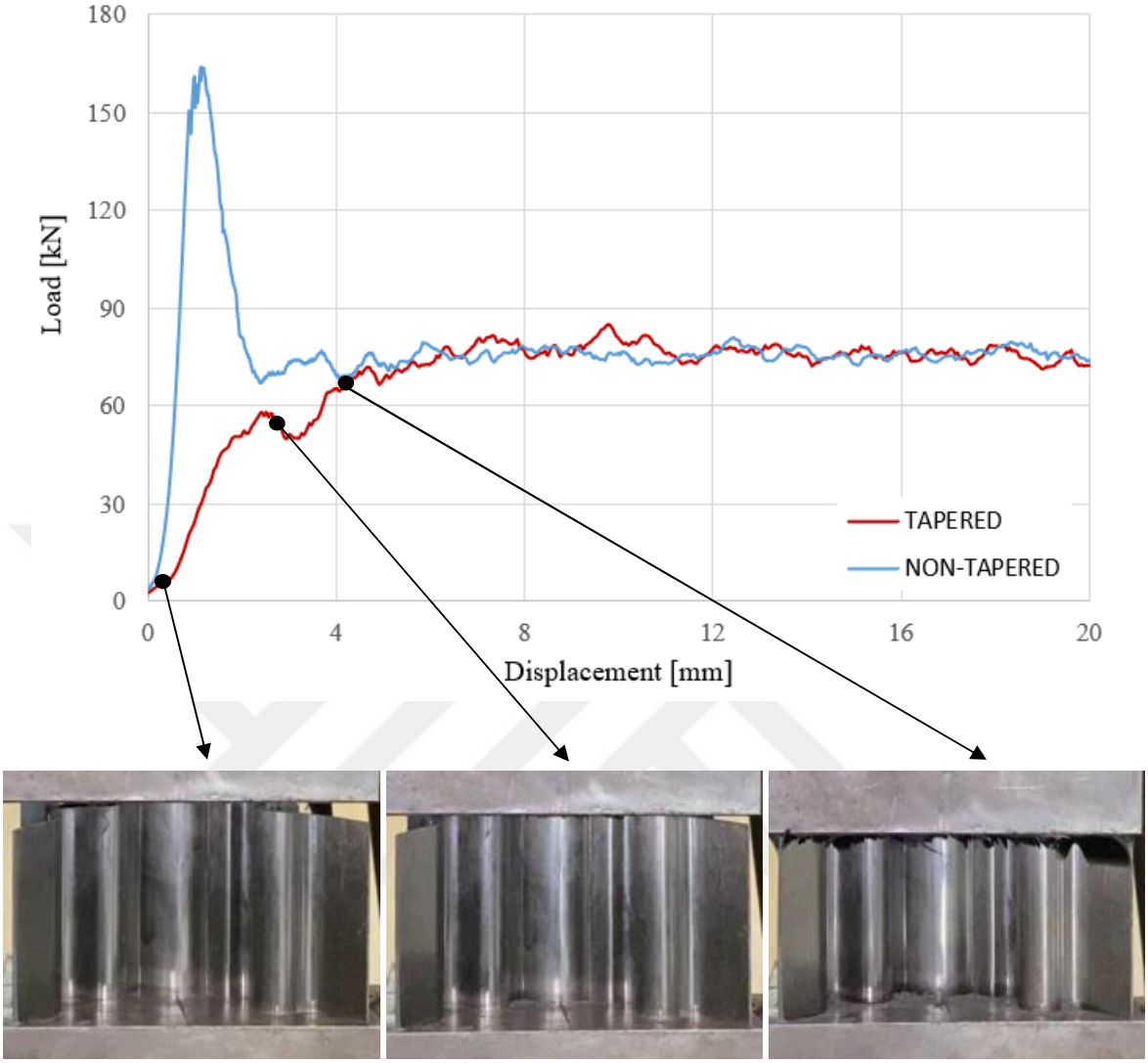

Figure 5.24. Experimental results of the tapered SL4 structure: load-displacement curve (top) and crushing morphology (bottom).

Table 5.6. Comparison between the SEA values of tapered and non-tapered structures.

Specimen	**SEA [J/g]**
tapered	78.28
non-tapered	79.46

6. CONCLUSION

This dissertation, in which the crushing of composite structures under axial loading is investigated both experimentally and numerically, consisted of four parts: i) crushing of flat plates, ii) the investigation of the influence of geometry on SEA through semi-circle and sinusoidal structures, iii) the development of novel computationally cost-effective FE Model, and iv) the design and manufacturing of a novel crash box geometry. This thesis study is believed to contain important findings and some major contributions to the field of crashworthiness of composite structures.

Predicting the crushing behavior of composite structures is a complex phenomenon since there are many distinct failure modes occurring simultaneously during the crush event, each providing a different energy absorption capability. Furthermore, the types and occurrence order of the crush-induced failure mechanisms depend on several factors and directly affects the SEA performance. Despite the extensive literature of experimental and numerical studies, it has been still unclear how failure modes are share and determine the level of absorbed energy. This dissertation presented both experimental and numerical investigations for the crushing process of AS4/8552 carbon/epoxy flat coupon plates with lay-ups of $[0/90]_{2s}$, $[0/90]_{3s}$, $[0/90]_{4s}$, and $[0/45/0/-45]_{s}$. A comprehensive understanding of the failure mechanisms taking place during the crush event is achieved. The overall understanding compiled from experimental study is that the length of the interlaminar crack indicates the failure mode, which can be either splaying or fragmentation. In a cross-ply specimen, while outer 0-degree plies have higher tendency to bend which creates splaying mode, fragmentation mode is observed mostly due to the matrix cracks in 90-degree plies. As a result of all these modes of damage, composite flat plates with 8 plies were found to have the SEA of 34.12 J/g. When the influence of plate thickness on SEA was investigated, the experimental results showed that the SEA remains the same (around 34 J/g) for the specimens with various thicknesses because there is no change in the type and occurrence order of the failure modes, only the amount of damage increases proportional to increasing mass. For $[0/45/0/-45]_{s}$ plate, more fiber breakages, thus fragmentation in 45-degree plies observed and this increases the energy absorption capability from 34,12 to 41,82 J/g.

One of the areas in the literature this study aims to make a major contribution was the modelling of the crushing behavior of the composite structures. Since the experimental methods are mostly time consuming and expensive, commercial Finite Element Analysis (FEA) programs are becoming popular and lead to simulate the failure of composite structures at lower costs. FE Models conducted for the crushing process of composite structures, on the other hand, cannot always provide accurate estimations due to the complex nature of the crushing process of composite structures including not only intralaminar failure mechanisms (in plane failure), but also interlaminar failure mechanisms (delamination). Moreover, for the modelling of complex composite structures, computational cost has been still an issue that needs to be dealt with. Although there are some attempts made in numerical studies to decrease run times, accurate modelling methods leading feasible computational (CPU) costs are still required. Within the scope of this thesis work, firstly, conventional FE model was developed for the crushing behavior of composite flat plates in ABAQUS/Explicit. According to the results, the model is shown to be capable of estimating both failure mechanisms and the SEA performance. Furthermore, as one of the significant contributions to the literature, a novel numerical approach was proposed by which energy absorption capabilities can be estimated in shorter run times. With the novel modelling idea of creating sub-laminates, thus reducing the number of interfaces, and modifying the relevant properties, the computational time was decreased by more than 50% for cross-ply flat plates when compared to the conventional FE model. Moreover, by applying the same approach to the $[0/45/0/-45]_s$ plates, validity of the model for different stacking sequences was also demonstrated. The adaptability of the model to complex geometries was further investigated, and it was proved that the model can be utilized in the design process of new crash box structures.

Geometry has a significant influence on Specific Energy Absorption (SEA) of composite structures; however, the variation of crush induced failure mechanisms for various geometric features and the way they affect energy absorption capability has not yet been fully clarified. Moving from simple flat specimens to complex structures, there has been a requirement to conduct a systematic study investigating the influence of geometry on SEA. For that purpose, this dissertation presented experimental and numerical investigations for the crushing process of AS4/8552 carbon fiber/epoxy semi-circle specimens, and sinusoidal structures with different diameter sizes and number of curvatures. The main goal

of this section was to understand the variation of the crush induced failure mechanisms through various geometries and their contributions to the energy absorption capability. The conclusion derived from the experimental study is that there is a combination of splaying mode and fragmentation mode due to the matrix cracks in most of the 90-degree plies and fiber breakages in 0-degree plies located in the center of the laminate. The levels and the occurrence order of these failure modes apparently determines the energy absorption capability. When the crushing morphology of semi-circle specimens were investigated, more fragmentation was observed in the center and vertical ruptures occurred at the outer plies which leads higher levels of specific energy absorption (48,9 J/g) as compared to flat specimens. The level of fragmentation increased even more for the sinusoidal structures since the number of vertical ruptures increased and the reflection points, connecting one of the repeating semi-circle segments to another, creating obstacles that leads more micro-buckling in 0-degree plies. Overall, sinusoidal structures were identified to have greater potential in terms of energy absorption.

The motivation behind conducting a study for sinusoidal structures with different geometric features was to understand the reason behind the change in energy absorption capabilities and to find out the structure having better performance. The idea was to keep the amount of material, thus weight constant while adding more semi-circle segments which leads to the decrease in radii. Therefore, sinusoidal structures with 3, 5 and 7 curvatures were tested under quasi-static compression conditions and their energy absorption capabilities with corresponding failure mechanisms were compared and discussed. Sinusoidal structure with 5 curvatures gave the highest SEA result of 68,73 J/g due to the higher number of vertical ruptures when compared to the sinusoidal structure with 3 curvatures. On the other hand, for the sinusoidal structure with 7 curvatures, SEA value did not further increase because of the instabilities occurring during the crushing process related to the low aspect ratio (the width to length ratio).

One of the objectives was to develop a conventional FE model which can not only estimate the amount of energy absorption, but also simulate the failure mechanisms occurring during the crushing process. Accurate FE Models were generated in ABAQUS/Explicit by including an artificial plug-initiator to get realistic simulation results. According to the presented results, numerical model showed good correlation with the

experimental data, can estimate energy absorption capability accurately and simulates the crushing behavior consistently. In the same section, the novel numerical approach porposed was also applied for AS4/8552 cross-ply sinusoidal structures with 3 curvatures. Results clearly showed that the model with 3-interfaces is proved to be applicable to complex geometries and can estimate SEA values of sinusoidal structure consistently in a shorter run time when compared to conventional 7-interface FE models. Computational time was reduced by 54%, from 241 minutes to 130 minutes on a 16-core computer.

In the final chapter of the dissertation, a design study was conducted to create a novel crash box geometry. The design idea of the crash box structure was to combine sinusoidal plates having 5 semi-circle curvatures by using the T-shaped joints. The reason behind the inclusion of T-joints in the design was that just like reflection points on sinusoidal geometry, T-joints were expected to create extra obstacles, increase the fragmentation level, and thus increase the amount of energy absorbed by unit mass. Several design attempts in ABAQUS/Explicit were made by modelling the crushing behavior with the novel numerical approach. After the simulations were completed, SEA values for each geometry were evaluated and the results were compared in order to decide which geometry to manufacture. According to the results, sun-like shapes with the circular core provided a significant advantage in terms of energy absorption capability over parallel sinusoidal plate design and single sinusoidal structure. Even though the sun-like structure having 8 half sinusoidal arms exhibited slightly better performance than the structure having 4 arms, the sun-like geometry with 4 half sinusoidal arms was preferred to be manufactured by considering the complexity of the manufacturing process and part quality. The experimental results of the quasi-static compression tests of sun-like geometry showed that the SEA of the geometry became 79,46 J/g which is 230% and 16% higher than the flat plates and the single sinusoidal structures, respectively. In the last part of the chapter, tapering was applied to the edges of crash box structure to create a conical structure and decrease the initial peak load which may cause an excessive deceleration and a fatal damage to the passengers. According to the quasi-static compression test results, the peak load was prevented as predicted, and a gradual increase was achieved in the load-displacement curve, without a significant change in the SEA value.

In conclusion, it can be stated that this dissertation provides several significant contributions to the literature by conducting a systematic study to understand the influence of geometry on SEA, developing a novel numerical approach in the field of progressive failure of composite structures, and designing a new crash box structure that does not exist in the literature or industry. Nevertheless, there are still several improvements that should be done as a future work. In the future, the design process can be taken to the next stage by considering more complex geometries, different materials and lay-up configurations. Since the design study in the dissertation was centered on the composite structures made of UD prepregs stacked with cross-ply configurations, there is a requirement to expand the study in the specified direction to investigate the behavior of structures made of woven fabrics and 3-D woven composites.

REFERENCES

1. Fang, J., G. Sun, N. Qiu, N. H. Kim and Q. Li, "On Design Optimization for Structural Crashworthiness and Its State of the Art", *Structural and Multidisciplinary Optimization*, Vol. 55, No. 3, pp. 1091–1119, 2016.

2. Chiaberge, M., *New Trends and Developments in Automotive Industry*, InTechOpen, London, 2011.

3. Eccomelt LLC, "Electric Vehicles to Transform Aluminum Demand by 2035", 2018, https://eccomelt.com/electric-vehicles-transform-aluminum-demand-2035/, accessed on March 29, 2023.

4. Czerwinski, F., "Current Trends in Automotive Lightweighting Strategies and Materials", *Materials*, Vol. 14, No. 21, p. 6631, 2021.

5. Ahmadvashaghbash, S., M. Engül, F. E. Öz, N. Ersoy, "A Comparative Numerical Study Aiming to Reduce Computation Cost for Mode-I Delamination Simulations", in *ECCM-18*, Athens, Greece, 2018.

6. Brechner, A., *A Safety Roadmap for Future Plastics and Composites Intensive Vehicles*, National Highway Traffic Safety Administration, Report No: DOT HS 810 863, Cambridge, 2007.

7. Tak, S. K. and M. A. Iqbal, "Axial compression Behavior of Thin-walled Metallic Tubes Under Quasi-static and Dynamic Loading", *Thin-Walled Structures*, Vol. 159, p. 107261, 2021.

8. Wade, B., *Capturing the Energy Absorbing Mechanisms of Composite Structures under Crash Loading*, PhD Thesis, University of Washington, 2014.

9. Hyer, M. W., *Stress Analysis of Fiber-Reinforced Composite Materials*, McGraw-Hill, Lancaster, 1997.

10. Agarwal, B. D., L. J. Broutman and K. Chandrashekhara, *Analysis and Performance of Fiber Composites*, Third Edition, John Wiley & Sons, New Jersey, 2006.

11. Rzeczkowski, J. and S. Samborski, “Experimental and Numerical Research of Delamination Process in CFRP Laminates with Bending-Twisting Elastic Couplings”, *Materials*, Vol. 15, p. 7745, 2022.

12. Andersen, M., *Crash Behavior of Composite Structures, A CAE Benchmarking Study*, M.S. Thesis, Chalmers University of Technology, 2014.

13. Farley, G., *Energy-absorption Capability of Composite Tubes and Beams*, NASA TM 101634, Hampton, 1989.

14. Farley, G. and R. Jones, "Crushing Characteristics of Continuous Fiber-reinforced Composite Tubes", *Journal of Composite Materials*, Vol. 26, No. 1, pp. 37-50, 1992.

15. Hull, D., "A Unified Approach to Progressive Crushing of Fiber-reinforced Composite Tubes", *Composite Science & Technology*, No. 40, pp. 377-421, 1991.

16. Carruthers, J., A. Kettle and A. Robinson, "Energy Absorption Capability and Crashworthiness of Composite Material Structures: A Review", *Applied Mechanics Reviews*, No. 51, pp. 635-649, 1998.

17. Bisagni, C, "Experimental Investigation of the Collapse Modes and Energy Absorption Characteristics of Composite Tubes", *International Journal of Crashworthiness*, Vol. 14, No. 4, pp. 365-378, 2009.

18. Chen, D., X. Sun, B. Li, Y. Liu, T. Zhu and S. Xiao, “On Crashworthiness and Energy Absorbing Mechanisms of Thick CFRP Structures for Railway Vehicles”, *Polymers,* Vol.14, pp. 4795, 2022.

19. Israr, H., S. Rivallant, C. Bouvet and J. Barrau, “Finite Element Simulation of 0◦/90◦ CFRP Laminated Plates Subjected to Crushing Using a Free-face-crushing Concept”, *Composites Part A*, Vol.62, pp. 16-25, 2014.

20. Thornton, P., "Energy Absorption in Composite Structures", *Journal of Composite Materials*, Vol.13, No.3, pp. 248-262, 1979.

21. Farley, G., "Energy Absorption of Composite Materials", *Journal of Composite Materials*, Vol. 17, No.3, pp. 267-279, 1983.

22. Schmueser, D. and L. Wickcliffe, "Impact Energy Absorption of Continuous Fiber Composite Tubes", *Journal of Engineering Material and Technology*, Vol. 109, No.1, pp. 72-77, 1987.

23. Ryzińska, G., M. David, G. Prusty, J. Tarasiuk and S. Wroński, "Effect of Fiber Architecture on the Specific Energy Absorption in Carbon Epoxy Composite Tubes Under Progressive Crushing", *Composite Structures*, Vol. 227, p. 111292, 2019.

24. Wang, Y., J. Feng, J. Wu and D. Hu, "Effects of Fiber Orientation and Wall Thickness on Energy Absorption Characteristics of Carbon-Reinforced Composite Tubes under Different Loading Conditions", *Composite Structures*, Vol. 153, pp. 356-368, 2016.

25. Mahdi, E., A. M. S. Hamouda and T. A. Sebaey, "The Effect of Fiber Orientation on the Energy Absorption Capability of Axially Crushed Composite Tubes", *Materials and Design*, Vol. 56, pp. 923-928, 2014.

26. Thuis, H. and V. H. Metz, "The Influence of Triggering Configurations and Laminate Lay-Up on The Failure Mode of Composite Crush Cylinders", *Composite Structures*, Vol. 28, No. 2, pp. 37-43, 1994.

27. Palanivelu, S., E. Van Paepegem, J. Degrieck, J. Vantomme, D. Kakogiannis, J. Van Ackeren, D. Van Hemelrijck and J. Wastiels, "Crushing and Energy Absorption Performance of Different Geometrical Shapes of Small-Scale Glass/Polyester Composite Tubes under Quasi-Static Loading Conditions", *Composite Structures*, Vol. 93, No. 2, pp. 992–1007, 2011.

28. Sivagurunathan, R., S.L.T. Way and M. Y. Yaakob, "The Effects of Triggering Mechanisms on the Energy Absorption Capability of Circular Jute/Epoxy Composite Tubes under Quasi-Static Axial Loading", *Applied Composite Materials*, Vol. 25, No. 2, pp. 1401-1417, 2018.

29. Sawamura, S., Y. Yamazaki, S. Yoneyama and Y. Koyanagi, "Multi-Scale Numerical Simulation of Impact Failure for Cylindrical CRFP", *Advanced Composite Materials*, Vol. 30, pp. 19–38, 2021.

30. Feraboli, P., "Development of a Modified Flat-plate Test Specimen and Fixture for Composite Materials Crush Energy Absorption", *Journal of Composite Materials*, Vol. 19, No. 43, pp. 1967-1989, 2009.

31. Bru, T., P. Walderström, R. Gutkin, R. Olsson and G. M. Vyas, "Development of a Test Method for Evaluating the Crushing Behaviour of Unidirectional Laminates", *Journal of Composite Materials*, Vol. 51, No. 29, pp. 4041-4051, 2017.

32. Vigna, L., A. Calzolari, G. Galizia, G. Belingardi and D. S. Paolino, "Effect of Friction on a Crashworthiness Test of Flat Composite Plates", *Forces in Mechanics*, Vol. 6, p.100070, 2022.

33. Lausch, J., M. Takla and H. G. Schweiger, "Crush Characteristics of Flat-plate Discontinuous Carbon Composites", *Composite Structures*, Vol. 147, p. 106431, 2021.

34. Lavoie, J. A. and J. Morton, "Design and Application of a Quasistatic Crush Test Fixture for Investigating Scale Effects in Energy Absorbing Composite Plates" *NASA Contractor Report*, 4526, 1993.

35. Babaei, I., R. Garg, L. Vigna, D. S. Paolino, G. Belingardi, L. Cascone, A. Calzolari and G. Galizia, "Newly Developed Anti-Buckling Fixture to Assess the In-Plane Crashworthiness of Flat Composite Specimens", *Applies Science and Technology,* Vol. 10, p. 7797, 2020.

36. Lausch, J., M. Takla and H. G. Schweiger, “Insight into Crush Performance Comparison of Composite Profiles and Flat Plates”, *Composites Part B: Engineering,* Vol. 233, p. 109643, 2022.

37. C. M. Kindervater, “Energy Absorption of Composites as an Aspect of Aircraft Structural Crash-Resistance”, *Developments in the Science and Technology of Composite Materials*, Springer Netherlands, pp. 643–651, 1990.

38. Mamalis, A., M. Robinson, D. Manolakos, G. Demosthenous, M. Ioannidis and J. Carruthers, "Review: Crashworthy Capability of Composite Material Structures", *Composite Structures*, Vol. 37, No. 2, pp. 109-134, 1997.

39. Farley, G., "Effect of Specimen Geometry on the Energy Absorption Capability of Composite Materials", *Journal of Composite Materials*, Vol. 20, No. 4, pp. 390-400, 1986.

40. Mamalis, A., D. Manolakos, G. Viegelahn, S. M. Yap and G. Demosthenous, "On the Axial Crumbling of Fiber-Reinforced Composite Thin-Walled Conical Shells", *International Journal of Vehicle Design*, Vol. 12, No. 4, pp. 450-467, 1991.

41. Farley, G. and R. Jones, "Crushing Characteristics of Composite Tubes with 'Near Elliptical' Cross Sections", *Journal of Composite Materials*, Vol. 26, No. 12, pp. 1741-1751, 1992.

42. Hanagud, S., I. Craig, P. Sriram and W. Zhou, “Energy Absorption Behavior of Graphite Epoxy Composite Sine Webs”, *Journal of Composite Materials*, Vol. 23, No. 5, pp. 448–459, 1989.

43. Wiggenraad, J. F., D. Santoro, F. Lepage, C. Kindervater, and H. C. Mañez, “Development of a Crashworthy Composite Fuselage Concept for a Commuter Aircraft”, paper presented at the *CEAS Forum on Crash Questions*, Italy, 2000.

44. Sokolinsky, V.S., K.C. Indermuehle and J.A. Hurtado, “Numerical Simulation of the Crushing Process of a Corrugated Composite Plate”, *Composites Part A: Applied Science and Manufacturing*, Vol. 42, No. 9, pp. 1119–1126, 2013.

45. Soni S., "A Comparative Study of Failure Envelopes in Composite Laminates", *Journal of Reinforced Plastic Composites*, Vol. 2, No. 1, pp. 34-42, 1983.

46. Tsai, S., "A Survey of Macroscopic Failure Criteria for Composite Materials", *Journal of Reinforced Plastic Composites*, Vol. 3, No. 1, pp. 40-62, 1984.

47. Nahas, M., "Survey of Failure and Post-Failure Theories of Laminated Fiber Reinforced Composites", *Journal of Composites Technology and Research*, Vol. 8, No. 4, pp. 138-153, 1986.

48. Orifici, A. C., I. Herszberg and R. Thomson, "Review of Methodologies for Composite Material Modelling Incorporating Failure", *Composite Structures,* Vol. 86, No. 1-3, pp. 194-210, 2008.

49. Hashin Z., "Failure Criteria for Unidirectional Fiber Composites", *Journal of Applied Mechanics*, Vol. 47, No. 2, pp. 329-334, 1980.

50. Chang, F. and K. Chang, "A Progressive Damage Model for Laminated Composites Containing Stress Concentrations", *Journal of Composite Materials*, Vol. 21, No. 9, pp. 834-855, 1987.

51. Puck, A. and H. Schurmann, "Failure Analysis of FRP Laminates by Means of Physically Based Phenomenological Models", *Composites Science and Technology*, Vol. 62, No: 12-13. pp. 1633-1662, 2002.

52. Davila, C. G., N. Jaunky and S. Goswami, “Failure Criteria for FRP Laminates in Plane Stress”, in *44th AIAA/ ASME/ ASCE/ AHS/ ASC Structures, Structural Dynamics, and Materials Conference*, Norfolk, 2003.

53. Pinho, S. T., L. Iannucci and P. Robinson, “Physically-Based Failure Models and Criteria for Laminated Fiber-Reinforced Composites with Emphasis on Fiber Kinking: Part I: Development”, *Composites Part A: Applied Science and Manufacturing,* Vol. 37, No. 1, pp. 63–73, 2006.

54. Hinton, M. J., A. S. Kaddour and P. D. Soden, "A Comparison of the Predictive Capabilities of Current Failure Theories for Composite Laminates, Judged Against Experimental Evidence", *Composites Science and Technology*, Vol. 62, No. 12-13 , pp. 1725-1797, 2002.

55. Jiang, H., Y. Ren, Z. Liu, S. Zhang and X. Wang, “Evaluations of Failure Initiation Criteria for Predicting Damages of Composite Structures Under Crushing Loading”, *Journal of Reinforced Plastics and Composites*, Vol.37, No. 21, pp. 1279 – 1303, 2018.

56. Kachanov, L.M., *Introduction to Continuum Damage Mechanics*, Martinus Nijhoff Publishers, Boston, 1986.

57. Lemaitre, J. and J.L. Chaboche, *Mechanics of Solid Materials*, Cambridge University Press, Cambridge, 1990.

58. Talreja, R. "Damage Development in Composites: Mechanisms and Modelling", *The Journal of Strain Analysis for Engineering Design*, Vol. 24, No. 4, pp. 215-222, 1989.

59. Donadon, M. V., L. Iannucci, B. G. Falzon, J. M. Hodgkinson and S. F. M. de Almeida, “A Progressive Failure Model for Composite Laminates Subjected to Low Velocity Impact Damage”, *Computers and Structures*, Vol. 86, No. 11-12, pp. 1232-1252, 2008.

60. Faggiani, A. and B. G. Falzon, “Predicting Low-Velocity Impact Damage on a Stiffened Composite Panel”, *Composites Part A: Applied Science and Manufacturing,* Vol. 41, No. 6, pp. 737-749, 2010.

61. Falzon, B. G. and P. Apruzzese, “Numerical Analysis of Intralaminar Failure Mechanisms in Composite Structures. Part I: FE Implementation”, *Composite Structures*, Vol. 93, No. 2, pp. 1039-1046, 2011.

62. Falzon, B. G. and P. Apruzzese, “Numerical Analysis of Intralaminar Failure Mechanisms in Composite Structures. Part II: Applications”, *Composite Structures*, Vol. 93, No. 2, pp.1047-1053, 2011.

63. Boyina, R. T. G., V. K. Rayavarapu and V. V. S. Rao, “Continuum Damage Mechanics-Based Failure Prediction and Damage Assessment in Laminated Composite Structures”, *Mechanics Based Design of Structures and Machines*, Vol. 1, pp. 1 - 29, 2023.

64. Johnson, A. F., A. K. Pickett and P. Rozycki, "Computational Methods for Predicting Impact Damage in Composite Structures", *Composites Science and Technology*, Vol. 61, No. 15, pp. 2183-2192, 2001.

65. Abir, M. R., T. E. Tay, M. Ridha and H. P. Lee, “Modelling Damage Growth in Composites Subjected to Impact and Compression After Impact”, *Composite Structures*, Vol. 168, pp. 13–25, 2017.

66. Rondina, F. and L. Donati, “Comparison and Validation of Computational Methods for the Prediction of the Compressive Crush Energy Absorption of CFRP Structures”, *Composite Structures*, Vol. 254, p. 112848, 2020.

67. Ladevéze, P. and G. Lubineau, “On a Damage Mesomodel for Laminates: Micro–Meso Relationships, Possibilities and Limits”, *Composite Science and Technology*, Vol. 61, No. 15, pp. 2149–2158, 2001.

68. Camanho, P. P., C. G. Dávila and M. F. de Moura, “Numerical Simulation of Mixed-Mode Progressive Delamination in Composite Materials”, *Journal of Composite Materials*, Vol. 37, No. 16, pp. 1415–1424, 2003.

69. Hu, P., Z. W. Shi, X. X. Wang, W. D. Li, S. G. Zhou and X. Han, “Strength Degradation of Adhesively Bonded Single-Lap Joints in a Cyclic-Temperature Environment Using a Cohesive Zone Model”, *The Journal of Adhesion*, Vol. 91, No. 8, pp. 587-603, 2015.

70. Barenblatt, G. I., “The Mathematical Theory of Equilibrium Cracks in Brittle Fracture”, *Advances in Applied Mechanics*, Vol. 7, pp. 55–129, 1962.

71. Dugdale, D. S., "Yielding of Steel Sheets Containing Slits", *Journal of the Mechanics and Physics of Solids*, Vol. 8, pp. 100–104, 1960.

72. Hillerborg, A., M. Modeer and P. E. Petersson, "Analysis of Crack Formation and Crack Growth in Concrete by Means of Fracture Mechanics and Finite Element", *Cement and Concrete Research*, Vol. 6, pp. 773–782, 1976.

73. Song, K., C. Davila and C. Rose, "Guidelines and Parameter Selection for The Simulation of Progressive Delamination", *in ABAQUS User's Conference*, Munich, 2008.

74. Xiao, X., "Simulation of Composite Tubes Axial Impact with a Damage Mechanics Based Composite Material Model", *in 10th International LS-DYNA Users Conference*, Detroit, 2008.

75. Mamalis, A. G., D. E. Manolakos, M. B. Ioannidis, P. K. Kostazos and D. P. Papapostolou, "Axial Collapse of Hybrid Square Sandwich Composite Tubular Components With Corrugated Core: Numerical Modelling", *Composite Structures*, Vol. 58, No. 4, pp. 571-582, 2002.

76. Hörmann, M. and M. Wacker, "Simulation of the Crash Performance of Crash boxes based on Advanced Thermoplastic Composite", *in 5th European LS-DYNA Users Conference*, Birmingham, 2005.

77. Kiani, M., H. Shiozaki, and K. Motoyama, "Using Experimental Data to Improve Crash Modeling for Composite Materials", *Composite Materials and Joining Technologies for Composites*, Vol. 7, pp. 215-226, 2013.

78. Liu, Q., F. Jie, Y. Ma, Y. Zhang and Q. Li, "Crushing Responses and Energy Absorption Behaviors of Multi-Cell", *Thin-Walled Structures*, Vol. 155, p. 106930, 2020.

79. Zhou, G., Q. Sun, J. Fenner, D. Li, D. Zeng and X. Su, "Crushing Behaviors of Unidirectional Carbon Fiber Reinforced Plastic Composites Under Dynamic Bending and Axial Crushing Loading", *International Journal of Impact Engineering*, Vol. 140, p. 103539, 2020.

80. Alkhatib, F., E. Mahdi and A. Dean, "Crushing Response of CFRP and KFRP Composite Corrugated Tubes to Quasi-Static Slipping Axial Loading: Experimental Investigation and Numerical Simulation", *Composite Structures*, Vol. 246, p. 11237, 2020.

81. Indermuehle, K., G. Barnes, S. Nixon and M. Schrank, "Simulating Composites Crush and Crash Events Using Abaqus", *in 50th AIAA/ASME/ASCE/AHS/ASC Structures, Structural Dynamics, and Materials Conference*, 2009.

82. Tan, W., B. G. Falzon and M. Price, "Predicting the Crushing Behavior Of Composite Material Using High-Fidelity Finite Element Modelling", *International Journal of Crashworthiness*, Vol. 20, No. 1, pp. 60–77, 2014.

83. Jahani, M., H. Beheshti and M. Heidari-Rarani, "Effects of Geometry, Triggering and Foam-Filling on Crashworthiness Behaviour of a Cylindrical Composite Crash Box," *International Journal of Automotive and Mechanical Engineering*, Vol. 16, No. 2., pp. 6568–6587, 2019.

84. Falzon, B. G., "Computational Modelling of the Crushing of Carbon Fiber-Reinforced Polymer Composites", *Philosophical Transactions of the Royal Society A*, Vol. 380, p. 336, 2022.

85. Kumbasar, B., "The Effects of Symmetry Boundary Condition, Mass Scale and Impactor Size for Edge Impact Simulations on ABAQUS", *in AIAA Scitech*, San Diego, 2022.

86. McGregor, C., R. Vaziri and X. Xiao, "Finite Element Modelling of the Progressive Crushing of Braided Composite Tubes Under Axial Impact", *International Journal of Impact Engineering*, Vol. 6, No. 37,pp. 662-672, 2010.

87. Turon, A., C. Davila, P. Camanho and J. Costa, "An Engineering Solution for Mesh Size Effects in The Simulation of Delamination Using Cohesive Zone Models", *Engineering Fracture Mechanics*, Vol. 74, No. 10 , pp. 1665–1682, 2007.

88. Dallia, D., L. F. Varandas, G. Catalanotti, S. Foster and B. G. Falzon, "Assessing the Current Modelling Approach for Predicting the Crashworthiness of Formula One Composite Structures", *Composites Part B: Engineering*, Vol. 201, No. 15, p. 108242, 2020.

89. Lescheticky, J., G. Barnes and M. Schrank, "System Level Design Simulation to Predict Passive Safety Performance for CFRP Automotive Structures", *in SAE World Congress & Exhibition*, Detroit, 2013.

90. Hexcel. HexPly ® 8552 – Product Data Sheet. *EU Version* 2016.

91. Ueda, M., S. Anzai and T. Kubo, "Progressive Crushing of a Unidirectional CFRP Plate with V-Shaped Trigger", *Advanced Composite Materials*, Vol. 24, pp. 85–95, 2015.

92. Öz, F. E., S. Ahmadvashaghbash and N. Ersoy, "Damage Mode Identification in Transverse Crack Tension Specimens Using Acoustic Emission and Correlation with Finiteelement Progressive Damage Model", *Composites Part B: Engineering,* Vol. 165, pp. 84-95, 2019.

93. Öz, F. E., E. Calik and N. Ersoy, "Finite Element Analysis and Acoustic Emission Monitoring of Progressive Failure of Corrugated Core Composite Structures", *Composite Structures*, Vol. 253, pp. 1-16, 2020.

94. Falk, M. L., A. Needleman and J. R. Rice, "A Critical Evaluation of Dynamic Fracture Simulations Using Cohesive Surfaces". *Journal de Physique*, Vol. 4, pp. 43–50, 2001.

95. ABAQUS/Standard User's Manual, Version 6.14.

96. Curtis, P. T. and S. M. Bishop, “An Assessment of The Potential of Woven Carbon Fibre-Reinforced Plastics for High Performance Applications”, *Composites*, Vol. 15, No. 4, pp. 259–265, 1984.

97. OM10 Resin System Prepregs Technical Data Sheet, KordSA, accessed on June 20, 2023.

98. Bayu, A., K. Koronka, P. Kadarno, and J. Purbolaksono, “Energy Absorption Analysis of Composite Crash Box by Finite Element Method”, *in Proceedings of the 1st International Conference on Contemporary Risk Studies*, Indonesia, 2022.

99. Abada, M. and A. Ibrahim, “Hybrid Multi-Cell Thin-Walled Tubes for Energy Absorption Applications: Blast Shielding and Crashworthiness”, *Composite Part B: Engineering,* Vol.183, p. 107720 , 2020.

APPENDIX A: COPYRIGHT PERMISSIONS FOR FIGURES

Permissions for the reused visual materials are presented in this appendix.

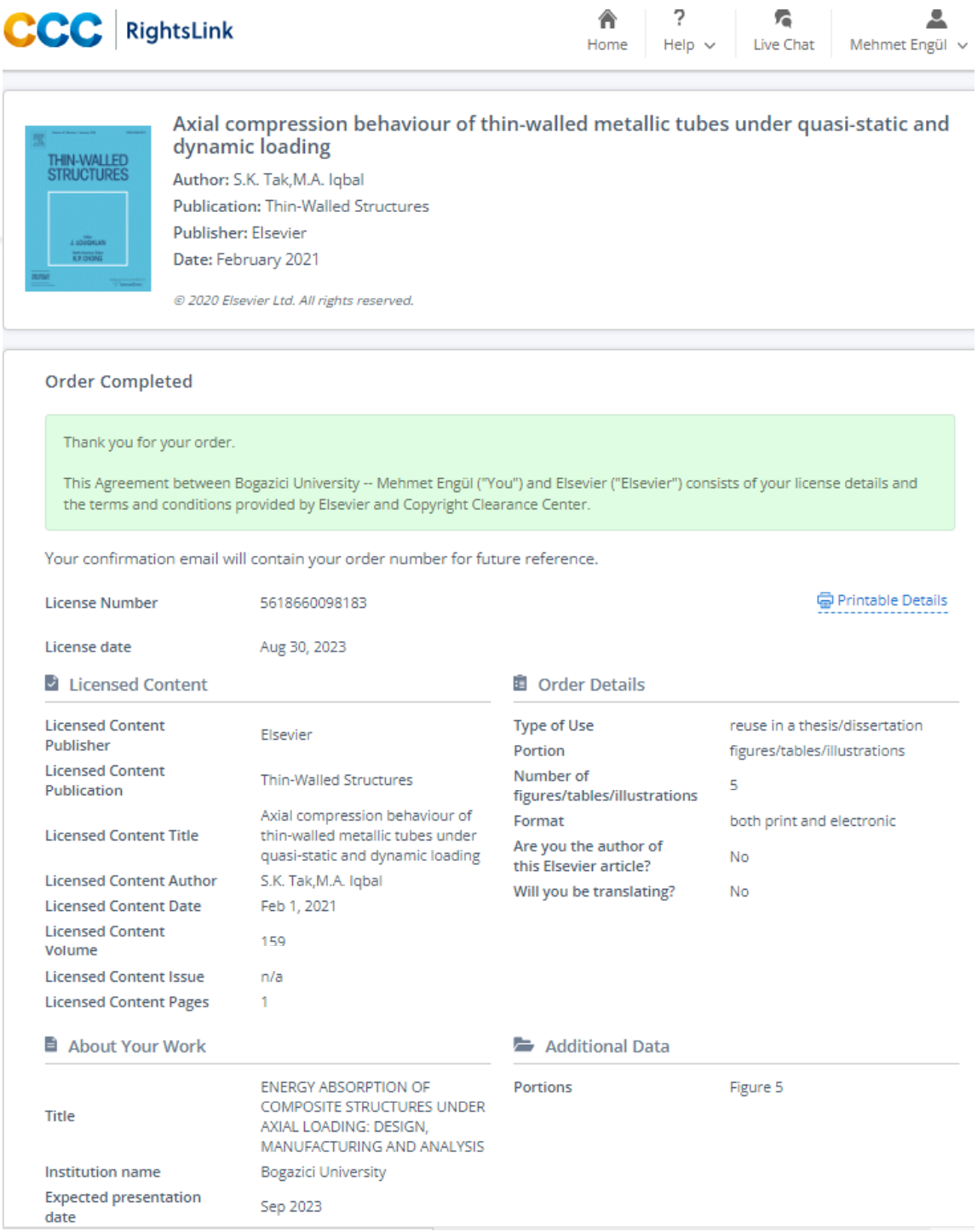

CCC RightsLink

Home | Help | Live Chat | Mehmet Engül

Axial compression behaviour of thin-walled metallic tubes under quasi-static and dynamic loading

Author: S.K. Tak,M.A. Iqbal
Publication: Thin-Walled Structures
Publisher: Elsevier
Date: February 2021

© 2020 Elsevier Ltd. All rights reserved.

Order Completed

Thank you for your order.

This Agreement between Bogazici University -- Mehmet Engül ("You") and Elsevier ("Elsevier") consists of your license details and the terms and conditions provided by Elsevier and Copyright Clearance Center.

Your confirmation email will contain your order number for future reference.

License Number	5618660098183
License date	Aug 30, 2023

Printable Details

Licensed Content

Licensed Content Publisher	Elsevier
Licensed Content Publication	Thin-Walled Structures
Licensed Content Title	Axial compression behaviour of thin-walled metallic tubes under quasi-static and dynamic loading
Licensed Content Author	S.K. Tak,M.A. Iqbal
Licensed Content Date	Feb 1, 2021
Licensed Content Volume	159
Licensed Content Issue	n/a
Licensed Content Pages	1

Order Details

Type of Use	reuse in a thesis/dissertation
Portion	figures/tables/illustrations
Number of figures/tables/illustrations	5
Format	both print and electronic
Are you the author of this Elsevier article?	No
Will you be translating?	No

About Your Work

Title	ENERGY ABSORPTION OF COMPOSITE STRUCTURES UNDER AXIAL LOADING: DESIGN, MANUFACTURING AND ANALYSIS
Institution name	Bogazici University
Expected presentation date	Sep 2023

Additional Data

Portions	Figure 5

Figure A.1. Permission for Figure 1.2.



CCC Marketplace

This is a License Agreement between Mehmet Engul ("User") and Copyright Clearance Center, Inc. ("CCC") on behalf of the Rightsholder identified in the order details below. The license consists of the order details, the Marketplace Permissions General Terms and Conditions below, and any Rightsholder Terms and Conditions which are included below.

Order Date	30-Aug-2023
Order License ID	1391684-1
ISBN-13	9780070167001
Type of Use	Republish in a thesis/dissertation
Publisher	MCGRAW-HILL HIGHER EDUCATION
Portion	Image/photo/illustration

LICENSED CONTENT

Publication Title	Stress analysis of fiber-reinforced composite materials
Author/Editor	HYER, MICHAEL W., WHITE, S. R.
Date	01/01/1997
Language	English
Country	United States of America
Rightsholder	McGraw Hill LLC
Publication Type	Book

NEW WORK DETAILS

Title	ENERGY ABSORPTION OF COMPOSITE STRUCTURES UNDER AXIAL LOADING: DESIGN, MANUFACTURING AND ANALYSIS
Instructor Name	Mehmet Engul
Institution Name	Boğaziçi University
Expected Presentation Date	2023-09-03

REQUESTED CONTENT DETAILS

Title, Description or Numeric Reference of the Portion(s)	Figure 9.1
Editor of Portion(s)	N/A
Volume / Edition	N/A
Page or Page Range of Portion	351
Title of the Article/Chapter the Portion Is From	Failure Theories for Fiber Reinforced Materials
Author of Portion(s)	HYER, MICHAEL W.; WHITE, S. R.
Issue, if Republishing an Article From a Serial	N/A
Publication Date of Portion	1997-01-01

Figure A.2. Permission for Figure 1.3.

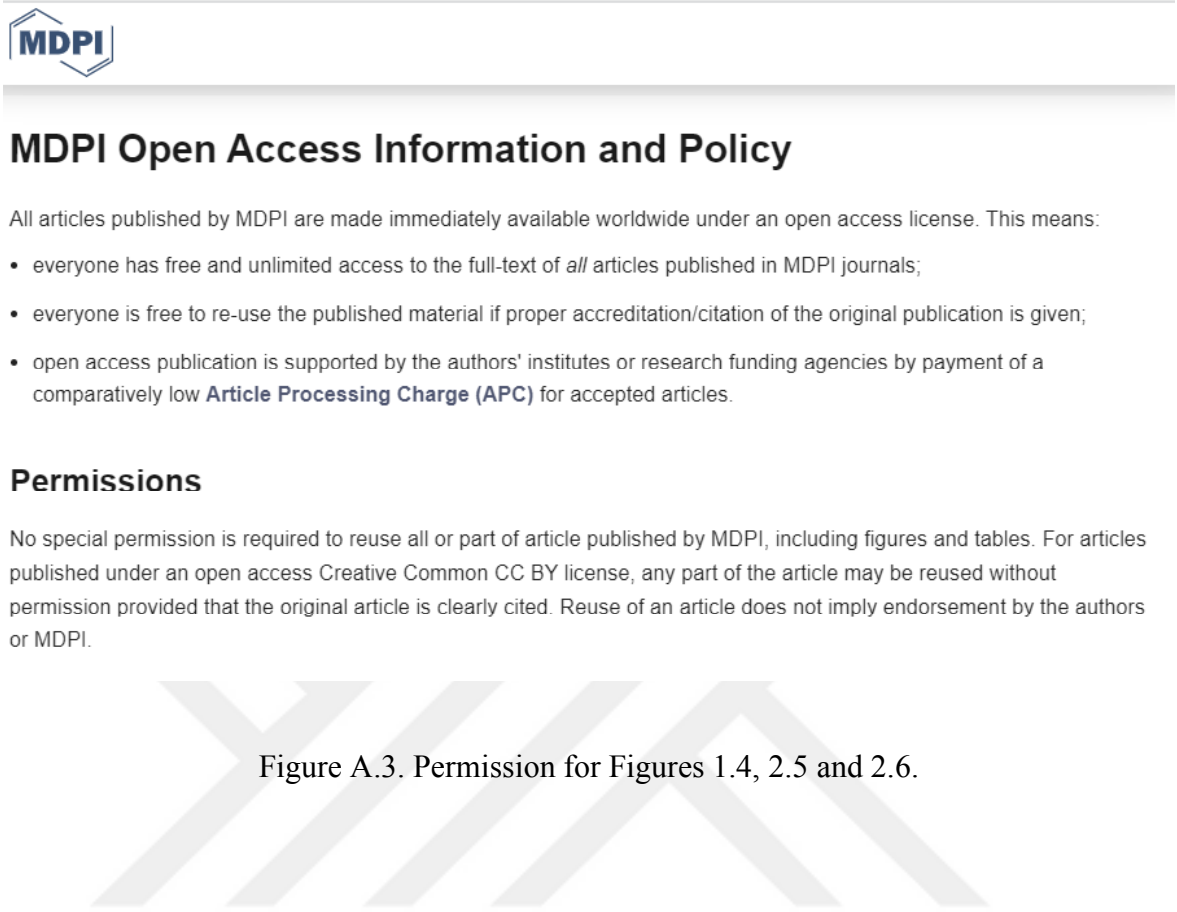

MDPI

MDPI Open Access Information and Policy

All articles published by MDPI are made immediately available worldwide under an open access license. This means:

- everyone has free and unlimited access to the full-text of *all* articles published in MDPI journals;
- everyone is free to re-use the published material if proper accreditation/citation of the original publication is given;
- open access publication is supported by the authors' institutes or research funding agencies by payment of a comparatively low **Article Processing Charge (APC)** for accepted articles.

Permissions

No special permission is required to reuse all or part of article published by MDPI, including figures and tables. For articles published under an open access Creative Common CC BY license, any part of the article may be reused without permission provided that the original article is clearly cited. Reuse of an article does not imply endorsement by the authors or MDPI.

Figure A.3. Permission for Figures 1.4, 2.5 and 2.6.



CCC Marketplace

This is a License Agreement between Mehmet Engul ("User") and Copyright Clearance Center, Inc. ("CCC") on behalf of the Rightsholder identified in the order details below. The license consists of the order details, the Marketplace Permissions General Terms and Conditions below, and any Rightsholder Terms and Conditions which are included below.

Order Date	30-Aug-2023
Order License ID	1391690-1
ISSN	0266-3538
Type of Use	Republish in a thesis/dissertation
Publisher	PERGAMON
Portion	Image/photo/illustration

LICENSED CONTENT

Publication Title	Composites science and technology
Article Title	A unified approach to progressive crushing of fibre-reinforced composite tubes
Date	01/01/1985
Language	English
Country	United Kingdom of Great Britain and Northern Ireland
Rightsholder	Elsevier Science & Technology Journals
Publication Type	Journal
Start Page	377
End Page	421
Issue	4
Volume	40

NEW WORK DETAILS

Title	ENERGY ABSORPTION OF COMPOSITE STRUCTURES UNDER AXIAL LOADING: DESIGN, MANUFACTURING AND ANALYSIS
Instructor Name	Mehmet Engul
Institution Name	Bogazici University
Expected Presentation Date	2023-09-03

REQUESTED CONTENT DETAILS

Title, Description or Numeric Reference of the Portion(s)	Figures 11 and 23
Editor of Portion(s)	Hull, D.
Volume / Edition	40
Page or Page Range of Portion	377-421
Title of the Article/Chapter the Portion Is From	A unified approach to progressive crushing of fibre-reinforced composite tubes
Author of Portion(s)	Hull, D.
Issue, if Republishing an Article From a Serial	4
Publication Date of Portion	1991-01-01

Figure A.4. Permission for Figures 2.1 and 2.4.

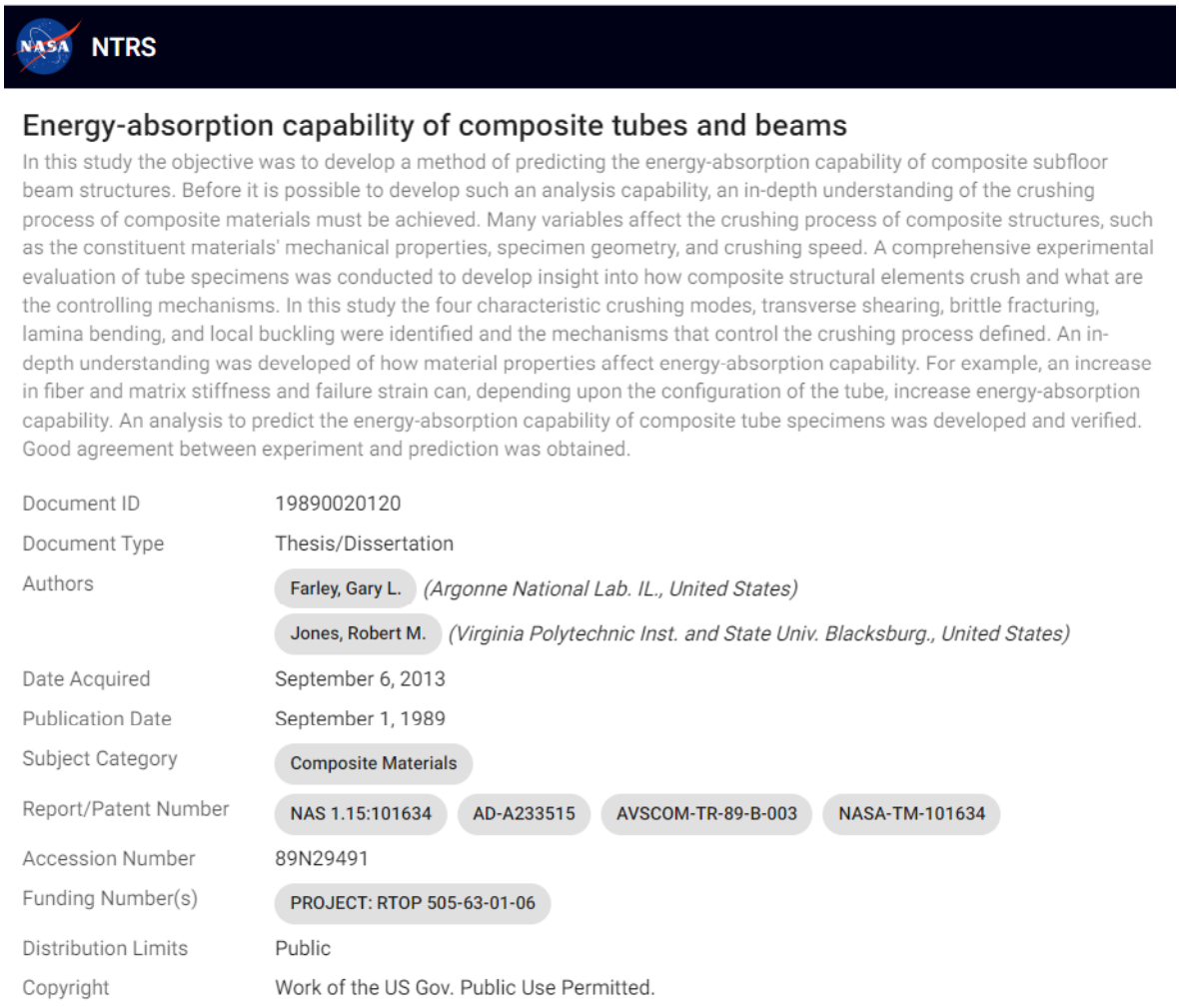

NTRS

Energy-absorption capability of composite tubes and beams

In this study the objective was to develop a method of predicting the energy-absorption capability of composite subfloor beam structures. Before it is possible to develop such an analysis capability, an in-depth understanding of the crushing process of composite materials must be achieved. Many variables affect the crushing process of composite structures, such as the constituent materials' mechanical properties, specimen geometry, and crushing speed. A comprehensive experimental evaluation of tube specimens was conducted to develop insight into how composite structural elements crush and what are the controlling mechanisms. In this study the four characteristic crushing modes, transverse shearing, brittle fracturing, lamina bending, and local buckling were identified and the mechanisms that control the crushing process defined. An in-depth understanding was developed of how material properties affect energy-absorption capability. For example, an increase in fiber and matrix stiffness and failure strain can, depending upon the configuration of the tube, increase energy-absorption capability. An analysis to predict the energy-absorption capability of composite tube specimens was developed and verified. Good agreement between experiment and prediction was obtained.

Document ID	19890020120
Document Type	Thesis/Dissertation
Authors	Farley, Gary L. *(Argonne National Lab. IL., United States)*
	Jones, Robert M. *(Virginia Polytechnic Inst. and State Univ. Blacksburg., United States)*
Date Acquired	September 6, 2013
Publication Date	September 1, 1989
Subject Category	Composite Materials
Report/Patent Number	NAS 1.15:101634 AD-A233515 AVSCOM-TR-89-B-003 NASA-TM-101634
Accession Number	89N29491
Funding Number(s)	PROJECT: RTOP 505-63-01-06
Distribution Limits	Public
Copyright	Work of the US Gov. Public Use Permitted.

Figure A.5. Permission for Figure 2.3.

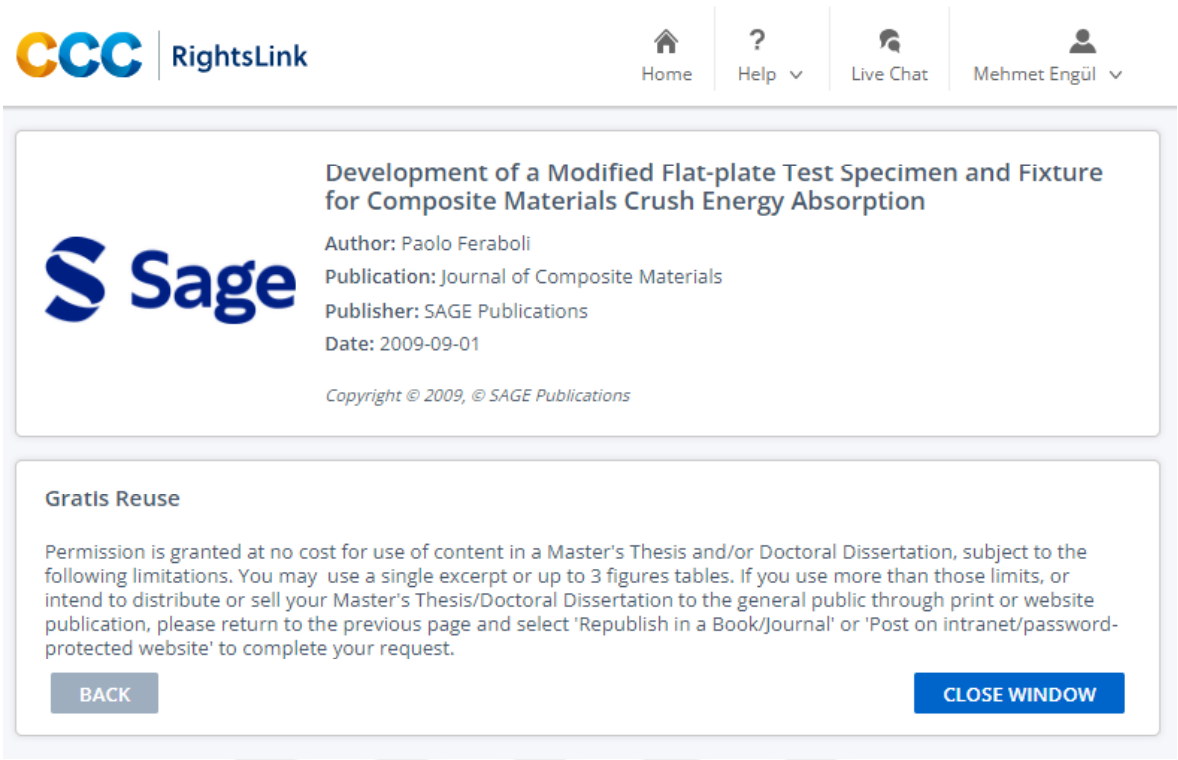

Figure A.6. Permission for Figure 2.7.

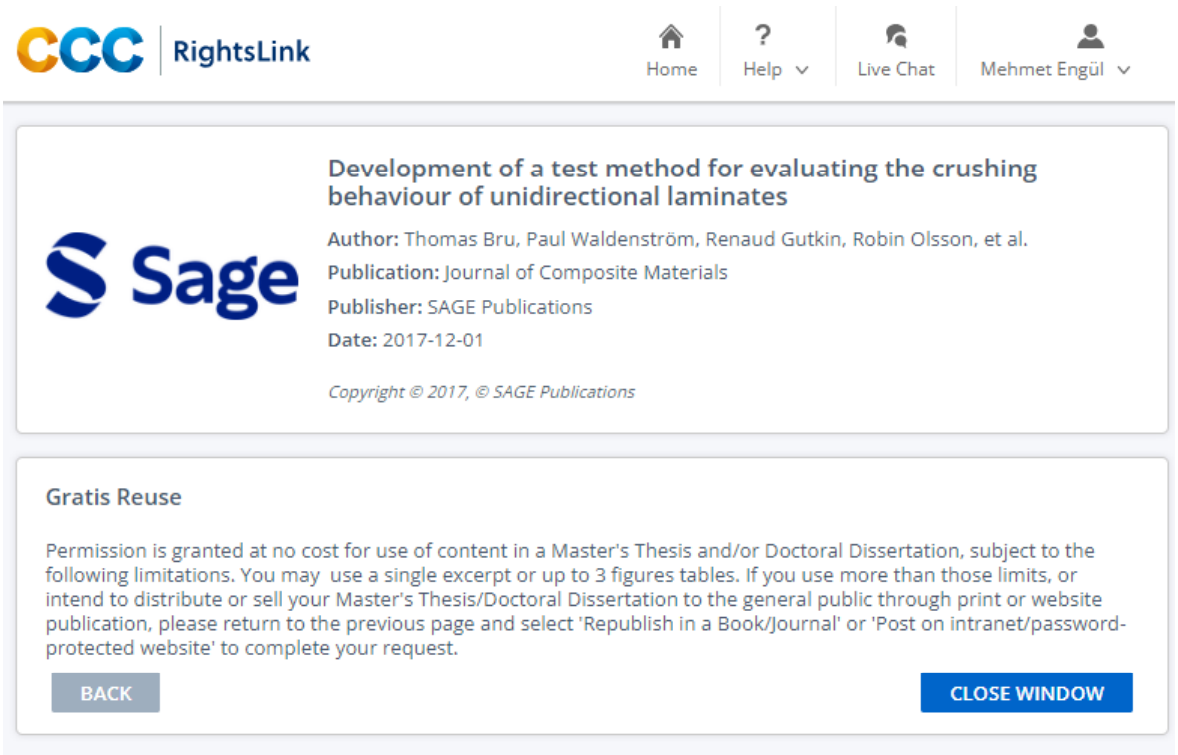

Figure A.7. Permission for Figure 2.9.



CCC Marketplace

This is a License Agreement between Mehmet Engul ("User") and Copyright Clearance Center, Inc. ("CCC") on behalf of the Rightsholder identified in the order details below. The license consists of the order details, the Marketplace Permissions General Terms and Conditions below, and any Rightsholder Terms and Conditions which are included below.

Order Date	30-Aug-2023
Order License ID	1391703-1
ISSN	1359-835X
Type of Use	Republish in a thesis/dissertation
Publisher	PERGAMON
Portion	Image/photo/illustration

LICENSED CONTENT

Publication Title	Composites. Part A, Applied science and manufacturing
Article Title	Crush characteristics of flat-plate discontinuous carbon composites
Date	01/01/1996
Language	English
Country	United Kingdom of Great Britain and Northern Ireland
Rightsholder	Elsevier Science & Technology Journals
Publication Type	Journal
Start Page	106431
Volume	147

NEW WORK DETAILS

Title	ENERGY ABSORPTION OF COMPOSITE STRUCTURES UNDER AXIAL LOADING: DESIGN, MANUFACTURING AND ANALYSIS
Instructor Name	Mehmet Engul
Institution Name	Bogazici University
Expected Presentation Date	2023-09-03

REQUESTED CONTENT DETAILS

Title, Description or Numeric Reference of the Portion(s)	Figure 1
Editor of Portion(s)	Lausch, J.; Takla, M.; Schweiger, H.-G.
Volume / Edition	147
Page or Page Range of Portion	106431
Title of the Article/Chapter the Portion Is From	Crush characteristics of flat-plate discontinuous carbon composites
Author of Portion(s)	Lausch, J.; Takla, M.; Schweiger, H.-G.
Issue, if Republishing an Article From a Serial	N/A
Publication Date of Portion	2021-08-01

Figure A.8. Permission for Figure 2.8.



Figure A.9. Permission for Figure 2.11.